Three-Dimensional Fluorescence Microscopy by Optical Scanning Holography

by

Bradley Wade Schilling

Dissertation submitted to the Graduate Faculty of
Virginia Polytechnic Institute and State University
in partial fulfillment of the requirements for the degree of

Doctor of Philosophy
in
Electrical Engineering

APPROVED:

_____
Dr. Ting-Chung Poon, Chairman

_____ _____
Dr. Ioannis M. Besieris Dr. Guy Indebetouw

_____ _____
Dr. Brian Storrie Dr. Ira Jacobs

December 5, 1997

Blacksburg, Virginia

Keywords: Optical Scanning Holography, 3D Imaging, 3D Fluorescence Microscopy

Three-Dimensional Fluorescence Microscopy by Optical Scanning Holography

by

Bradley W. Schilling
Ting-Chung Poon, Chairman

Electrical Engineering Department
(ABSTRACT)

As three-dimensional (3D) imaging and fluorescence techniques become standard in optical microscopy, novel approaches to 3D fluorescence microscopy are emerging. One such approach is based on the incoherent holography technique called optical scanning holography (OSH). The main advantage of OSH-based microscopy is that only a single two-dimensional (2D) scan is required to record 3D information, whereas most current 3D microscopes rely on sectioning techniques. To acquire a 3D representation of an object, current microscopes must physically scan the specimen in a series of 2D sections along the z-axis.

In order to record holograms by OSH, the fluorescent specimen is scanned with an optically heterodyned laser field consisting of a Fresnel zone pattern. A unique acousto-optic modulator configuration is employed to generate a suitable heterodyne frequency for excitation of the fluorescent object. The optical response of a solution containing a high concentration of 15 μm fluorescent latex beads to this type of excitation field has been recorded. In addition, holograms of the same beads have been recorded and reconstructed. To demonstrate the 3D imaging capability of the technique, the hologram includes beads with longitudinal separation of about 2 mm.

A detailed comparison of 3D fluorescence microscopy by OSH and the confocal approach was conducted. Areas for comparison were 3D image acquisition time, resolution limits and photobleaching. The analysis shows that an optimized OSH-based

fluorescence microscope can offer improved image acquisition time with equal lateral resolution, but with degraded longitudinal resolution when compared to confocal scanning optical microscopy (CSOM). For the photobleaching investigation, the parameter of concern is the fluence received by the specimen during excitation, which takes into account both the irradiance level and the time of illumination. Both peak and average fluence levels are addressed in the comparison. The analysis shows that during a 3D image acquisition, the OSH system will deliver lower peak fluence but higher average fluence levels to the specimen when compared to CSOM.

Acknowledgments

I would first like to express my gratitude to my advisor, Professor Ting-Chung Poon for his support and assistance. Professor Poon has carefully guided me through my entire graduate program at Virginia Tech. Along the way he has provided me with invaluable advice, unending assistance and a level of flexibility that I truly appreciate. Most importantly, Professor Poon's stimulating research ideas helped keep the work interesting and fun. I am also indebted to Professor Guy Indebetouw for his interest in the project and expert advise. Professor Indebetouw helped me to see the physics behind the engineering, providing me with a better overall understanding of the system. Thanks to Professor Brian Storrie, especially for taking the time to introduce me to the biological aspects of the project. Also thanks to Professor Ioannis Besieris and Professor Ira Jacobs for their guidance in my studies at Virginia Tech and for serving on my graduate committee.

I would also like to thank the people I work with at Night Vision, especially Dr. John Pollard, Wayne Grant, and John Nettleton for giving me the opportunity to pursue my degree and keep my job. I am particularly indebted to Brian Redman who always found the time to discuss my project and offer help. Brian's technical advice and guidance were a tremendous asset. Special thanks to Jonathan Lei and James Habersat, who offered their time and electronics expertise freely. Thanks to Dr. Nick Barr for his support and understanding. Thanks also to Bill Thodos for his advice and friendship.

Most importantly, I would like to thank my family. Thanks to my mom and dad who have always encouraged and supported me. I know they take as much pride in this accomplishment as I do. Thanks to my sisters, Sharon and Karen for their love and encouragement. Thanks to my brother, Gary, for his perspective and advice. Thanks also to Chris, Pat and Bobby. And special thanks to the kids, my nephews and nieces: Jorgen,

Kari, Tina, Kelsey, Zachary, Haleigh, Austin and Shannon. Even though we are getting spread around the country, I am happy that we are all still so close.

Thanks to my friends and predecessors from the Optical Image Processing Laboratory at Va. Tech, Brad Duncan who started it all, Mark McNeill, and Kyu Doh. Thanks to Derrek for the many conversations about school, computers and the market. And thanks to my best friends: Scott, Keith and Rich.

Finally, thanks to Amanda, who read every word of this dissertation and wrote many of them. In everything from in-depth discussions of the project, to long hours in the lab making holograms, Mandie has been there. But most importantly, thanks to Mandie for her support and caring which kept me going, even when things got tough.

Material support was provided in the form of equipment loan by Hamamatsu Corporation, NJ, and Hamamatsu Photonics K.K., Japan. Technical cooperation with Mr. Y. Shinoda, Dr. Y. Suzuki (Central Research Lab, Hamamatsu Photonics K.K., Japan) and Dr. M. H. Wu (Hamamatsu Corporation, NJ) is also greatly appreciated. This work has been supported by NSF grants under the Directorate of Biological Sciences (BIR-9419342) and the Directorate of Engineering (ECS-9319211).

Table of Contents

1.0 Introduction..... 1

2.0 Optical Scanning Holography..... 3
2.1 Background and Previous Work..... 4
2.2 Theory of Holographic Recording by OSH..... 6
2.3 EBSLM-Based Image Reconstruction.....9

3.0 Computer Simulations..... 12

3.1 General Considerations..... 13
3.2 Convolution and the 2-D Fast Fourier Transform..... 15
3.3 The Sampling Theorem and Aliasing..... 16
3.4 Computer Generated Holograms.....18
3.5 Numerical Reconstruction.....25

4.0 Selected Topics in Fluorescence.....30
4.1 The Physics of Fluorescence..... 30
4.1.1 Absorption and Emission Spectra..... 31
4.1.2 Fluorescence Lifetime and Quantum Efficiency.....35
4.1.3 Photobleaching.....37
4.2 Fluorescence Microscopy.....38
4.2.1 Fundamentals of Fluorescence Microscopy.....39
4.2.2 Fluorescence Microscopy in Three Dimensions.....41
4.2.3 Two-Photon Laser-Scanning Microscopy..... 44

5.0 Experimental Setup.....47
5.1 Important components..... 47
5.1.1 Argon Ion Laser System.....48
5.1.2 Acousto-optic Modulator Configuration.....49
5.1.3 AOM Drive and Demodulation Electronics.....52
5.1.4 Scanning and Data Acquisition..... 54
5.2 3-D Holographic Fluorescence Microscopy.....57

6.0 Experimental Results..... 62
6.1 Preliminary Fluorescence Results..... 62
6.2 Fluorescence Holograms by OSH.....65

7.0 Analysis.....70
7.1 Preliminary Calculations.....71
7.1.1 Rayleigh Range, Gaussian Beam Waist and Numerical Aperture.... 71
7.1.2 Relationship Between Number of Zones in FZP and z..... 74
7.1.3 Fringe Spacing and Sampling.....83
7.1.4 Scanning Limits.....84
7.1.5 FWHM, $1/e$ and $1/e^2$ Widths of a Gaussian Beam.....88
7.2 Resolution Limit..... 92
7.2.1 Resolution Limits for Optical Microscopy.....93
7.2.2 Resolution Limits for CSOM.....94
7.2.3 Resolution Limits for OSH..... 96
7.2.3.1 Resolution of the Current OSH Microscopy Setup..... 100
7.2.3.2 Theoretical and Practical Resolution Limit for Microscopy by OSH..... 102
7.3 Photobleaching Analysis.....104
7.3.1 Scanning Times..... 105
7.3.2 Minimum Irradiance Requirement for PMT Detection..... 107
7.3.3 Excitation Irradiance Requirement.....109
7.3.4 Total Power of Scanning Beam..... 115
7.3.5 Peak Irradiance and Peak Fluence.....119
7.3.6 Energy and Average Fluence..... 120
7.3.7 Calculations.....121
7.3.8 Summary of Photobleaching Analysis..... 127

8.0 Conclusions and Future Research..... 129

References.....133

Vita..... 139

List of Figures

Figure 1: Setup used for holographic recording by OSH..... 7

Figure 2: Reconstruction using an EBSLM..... 11

Figure 3: Dot object..... 19

Figure 4: Slit object..... 19

Figure 5: Particle field object..... 19

Figure 6: Computer generated FZP for $x = 0.00192$, $y = 0.00192$, $z = 0.035$ and $n = 10$.....22

Figure 7: Simulated hologram of the dot object shown in Figure 3..... 24

Figure 8: Simulated hologram of the slit object shown in Figure 4.....24

Figure 9: Simulated hologram of the "particle field" object shown in Figure 5..... 24

Figure 10: Numerical image reconstruction of the dot object, shown in Figure 3..... 28

Figure 11: Numerical image reconstruction of the slit object, shown in Figure 4.....28

Figure 12: Numerical image reconstruction of the particle field object shown in Figure 5..... 28

Figure 13: Computer generated FZP for $x = 0.00192$, $y = 0.00192$, $z = 0.01$ and $n = 10$.....29

Figure 14: Simulated hologram of the "particle field" object shown in Figure 5 using the FZP shown in Figure 13 as the scanning pattern..... 29

Figure 15: Numerical reconstruction of the hologram shown in Figure 14..... 29

Figure 16: Electronic state diagram showing fluorescence.....33

Figure 17: Optical fluorescence microscope block diagram..... 40

Figure 18: a) Block diagram of the components which make up a confocal scanning laser microscope. b) Enlarged view of the focusing action in the specimen.....43

Figure 19: Acousto-optic modulator configuration for the generation of two light beams separated by a temporal frequency difference of $2\Omega_2$..... 51

Figure 20: Block diagram of the electronic setup used to generate the AOM drive signals and demodulate the PMT signal in holographic fluorescence microscopy..... 53
Figure 21: Block diagram of the optical experimental setup used to record the hologram of a fluorescent specimen by optical scanning holography..... 58
Figure 22: Oscilloscope trace showing the measured heterodyned laser field used to excite the fluorescent specimen. The scope is DC coupled with 0 volt DC level at the '4-' in the lower left hand corner. The voltage scale is 20 mV/div and the time scale is 50 ns/div..... 64
Figure 23: Oscilloscope trace showing the measured fluorescent response to the heterodyned laser excitation after filtering and amplification. The scope is AC coupled with 0 volt level at the center. The voltage scale is 10 mV/div and the time scale is 50 ns/div..... 64
Figure 24: Experimental configuration of fluorescent solution on the ends of two wires..... 66
Figure 25: Hologram of fluorescent specimen recorded using OSH. The object consists of two drops of solution containing a high concentration of fluorescent latex beads separated in depth by about 2 mm. The image is a 256 level gray scale image consisting of 256 $\times$ 256 pixels. The area scanned is about 2.0mm $\times$ 2.0 mm.....68
Figure 26: Reconstruction of the hologram shown in Figure 2 at a depth of $z_0 = 34.5\,mm$. Arrow shows individual fluorescent beads which are in focus at this depth.....68
Figure 27: Reconstruction of the hologram shown in Figure 2 at a depth of $z_1 = 36.8\,mm$. The arrow shows four individual fluorescent beads which are in focus at this depth..... 68
Figure 28: Focusing of a Gaussian beam with beam waist and numerical aperture shown.....73
Figure 29: Dependence of ω_{fzp} on z..... 76
Figure 30: Plot of N_z vs. z for $NA = 0.5,\ 0.75$ and 0.95. ($\lambda = 515\,nm$)..... 79
Figure 31: Plot showing maximum w_p vs. z, for small w_p and $N_z = 5,\ 10,$ and 20. ($\lambda = 515\,nm$)..... 81

Figure 32: Plot showing w_p vs. maximum z for large w_p and for $N_z = 5,\ 10,$ and $20.$ ($\lambda = 515\,nm$)..... 82
Figure 33: Maximum sampling step size versus z for $N_z = 5,\ 10$ and $20.$ 85
Figure 34: Diagram showing the scanning limits in the lateral dimension for a) beam scanning and b) object scanning..... 87
Figure 35: Plot of Gaussian and Airy pattern at the focus of a lens with $NA = 0.95$ ($\lambda = 515\,nm$).....90
Figure 36: Plot showing resolution limit for OSH at minimum z for $NA = 0.95$, $\lambda = 515\,nm$, and minimum number of zones $n = 10$..... 103
Figure 37: Diagram used in calculation of η_c(OSH), the light collection efficiency for the wide area detection scheme of OSH.....111
Figure 38: Plot showing $I_{fzp}(\rho,\ z)/L_{ex}$(OSH) versus ρ in μm.....117
Figure 39: Proposed setup to record scanning pattern during holographic recording..... 132

List of Tables

Table 1: Power output by wavelength.....48
Table 2: Conversion factors for comparing resolution criteria.....92
Table 3: Summary of relevant PMT specifications.....122
Table 4: Summary of values used for photobleaching analysis.....123
Table 5: Calculated values for equations (89) and (91).....125
Table 6: Major results of the photobleaching analysis.....128

1.0 Introduction

Optical scanning holography (OSH) is a technique used to record three-dimensional (3D) information of an object or scene by scanning it with a heterodyned Fresnel zone pattern (FZP) laser field and collecting the scattered light. As one of the primary research interests of the Optical Image Processing Laboratory at Virginia Tech, OSH has been investigated in detail by a number of researchers over the past decade. The work presented in this thesis introduces a new and exciting application of OSH: fluorescence microscopy. This work does not represent the first attempt to improve on standard microscopy using holographic techniques. Since its conception, holography has been applied to microscopy with limited success. In fact, research in 3D imaging of microscopic specimens led to the invention of holography by Dennis Gabor in 1949.[1] However, holographic techniques have apparently never been applied to fluorescence microscopy. Perhaps this is because of the common misconception that a coherent illumination/detection scheme is a prerequisite of holographic recording. OSH, on the other hand, successfully applies holographic techniques to microscopic fluorescent objects for the first time. In addition, OSH offers several improvements to current 3D fluorescence microscopes.

Since the days of "wavefront reconstruction" by Gabor, a number of sophisticated 3D imaging techniques have been employed to view and record 3D information of microscopic samples. Perhaps the most successful optical technique developed in recent years is that of confocal scanning optical microscopy (CSOM). Current techniques in 3D microscopy, including CSOM, involve sectioning and reconstitution. The approach is to take a series of sections through the sample at different depths, image and then merge the information into a single, 3D image. The required depth, or z-scanning, is the major drawback of these methods as it is time consuming and requires very precise mechanical

positioning. The potential of eliminating the depth scan required by current techniques gave us the impetus to investigate holographic microscopy. An attractive quality of holography is its inherent ability to store 3D information in a 2D array without a depth scan. 3D microscopy based on optical scanning holography makes use of this inherent advantage and only a single 2D scan of a thick specimen is required to record 3D information. This results in a significant time savings in data acquisition and a reduction in photobleaching.

Although applying holographic techniques to microscopy is not in itself original, many aspects of this project are "first-time" innovations in the field, particularly in the area of fluorescence. A recent major innovation in light microscopy is the use of fluorescent dyes as selective stains or markers in living cells. These dyes were originally utilized by biologists to improve contrast and resolution. The dyes are now being used in conjunction with laser scanning and confocal microscopy techniques to obtain 3D images. Since the recording technique used in OSH is incoherent, holographic recording of fluorescent objects is possible. Therefore, the system can take advantage of the same characteristics which make fluorescence attractive in standard light microscopy. To our knowledge, holograms of fluorescent objects have never been recorded. The new technique combines the 3D imaging capability of optical scanning holography with the advantages of fluorescence microscopy techniques. This research, which brings these ideas together for the first time, will lead to the first 3D holographic fluorescence microscope.

It is appropriate to address some background material that is directly applicable to the project. In this vein, Chapter 2 addresses the history of OSH before reviewing the basic theoretical constructs of the process. Image reconstruction can be achieved optically, but in recent years PC-based numerical methods have been the prominent reconstruction technique. Chapter 3 includes a discussion of the important numerical methods behind numerical image reconstruction and presents a complete computer simulation of the system. It makes sense to consider pertinent areas of fluorescence and

fluorescence microscopy, including confocal techniques which are covered in Chapter 4. Although several areas are touched on theoretically in the first four chapters, the project has really been experiment driven. The primary goal being the demonstration of 3D fluorescence imaging of microscopic objects by OSH. The hardware and experimental configuration are described in Chapter 5. Experimental results are presented in Chapter 6. The application of OSH to fluorescence microscopy is a new and novel approach to a complicated and demanding problem. Although experimental verification of the technique is an important milestone, there are many additional steps toward the final goal of a practical system. Along these lines, a detailed analysis of the system, including a complete comparison with existing techniques, is equally as important. Current industry standards for 3D fluorescence microscopy are the confocal scanning optical or laser microscope. Chapter 7 presents a detailed comparison between OSH and CSOM in the practical areas of 3D image acquisition time, resolution, and photobleaching. Finally, Chapter 8 contains concluding remarks, including ideas for future research in 3D fluorescence microscopy by OSH.

2.0 Optical Scanning Holography

The backbone of this project is the incoherent holographic recording technique called optical scanning holography. This chapter addresses previous work done in the area and reviews the fundamentals of this technique.

2.1 Background and Previous Work

The origin of optical scanning holography is usually attributed to Poon and Korpel who suggested the use of an active optical heterodyne scanning technique for the recording of holograms in 1979.[2] The technique was subsequently analyzed in detail and further developed by Poon in 1985.[3,4] The fundamentals of this holographic recording technique, however, lie in incoherent methods which were first investigated more than a decade earlier. Since the first holograms were generated using coherent illumination, incoherently illuminated and self-luminous objects were initially considered unacceptable for holographic recording. Fortunately, this is not the case. Coherent illumination is not ultimately essential for holography as long as each object point somehow creates a Fresnel-zone pattern (FZP) on the recording medium. Several ingenious methods of producing this condition have been developed, including optical scanning holography. The significance of these developments is paramount since without incoherent holography, holography of fluorescent objects would be impossible. Remember, like self-luminous objects, an excited fluorescent molecule radiates incoherent light.

The first incoherent holographic recording technique was suggested by Mertz and Young[5] in 1962 and was applied to x-ray astronomy. In their technique, the lens of a camera was replaced by a FZP mask and used to record images of the stars. Instead of focusing the starlight, the mask caused each star to produced a FZP shadow on the film. In the reconstruction process, each FZP acts as a lens to produce an image. Lohmann[6] was the first to suggest a method of incoherent holography which divides the object light into two paths using an interferometer, although at about the same time the method was independently discovered by Cochran.[7] The separated light can be recombined in such a manner that each object point produces an intensity made up of the sum of a uniform bias and a spatially varying pattern, usually a FZP. Similar systems were investigated by many scientists in the following years.[8-12] Bias buildup is the major problem with these

techniques, as was first pointed out by Cochran[7] and later addressed by Kozma and Massey.[13] The buildup occurs if the object contains a large number of points, since an equally large number of zone plates must overlap on the film. The more points in the object, the higher the ratio of uniform bias to the spatially varying portion of the intensity pattern. According to Kozma and Massey, the brightness of the reconstruction for a given film is inversely proportional to the square of the density of resolvable points in the object.[13] The next section shows explicitly that OSH is another way to record a FZP for each object point. As will become evident, a major advantage of OSH is that it does not suffer from the bias buildup problem. Another method for incoherent holography has been proposed by Sirat and Psaltis which makes use of the properties of optical propagation through birefringent crystals.[14]

In recent years, the investigation and advancement of OSH has been a major research concern of the Optical Image Processing Laboratory at Virginia Tech. Not only does OSH offer advantages over other incoherent holography techniques, such as a lack of bias buildup, but it has advantages over standard holographic techniques as well. Since the holographic information manifests itself as an electric current, no photographic processing is necessary and real-time holography is possible. In fact, the first OSH experiments demonstrated real-time holography using an electron-beam-addressed spatial light modulator (EBSLM)-based reconstruction scheme.[15-18] As is often the case, these first experiments were conducted on 1D line objects. The system was subsequently improved to enable recording and reconstruction of 2D transmissive objects in real time, again making use of the EBSLM.[19,20] Continued research in OSH led to several new methods of incoherent image processing.[21] A detailed analysis of the twin image noise associated with this technique has also been conducted.[22,23] Elimination of this noise represents a major system improvement. A novel approach to preprocessing holographic information has been investigated.[24] Computer simulation has shown one example in which proper design of the scanning pattern records a hologram which displays edge

enhancement upon image reconstruction. Rigorous attention has also been given to the application of OSH to 3D microscopy.[25] This project has taken OSH in a new direction in its application to 3D fluorescence microscopy.[26]

2.2 Theory of Holographic Recording by OSH

On one level, 3D holographic fluorescence microscopy is simply an application of OSH. This section presents a detailed discussion of the theoretical basis of this holographic recording technique. In general terms, OSH is based on scanning the object with a temporally modulated Fresnel-zone pattern (FZP). The FZP is generated by superimposing a plane wave and a spherical wave which originate from the same laser. As with the other incoherent holography methods, the 3D location of the scatterer is encoded in the position and size of the FZP.[5] Unique to OSH, however, is the fact that the FZP is temporally modulated allowing for heterodyned detection. Heterodyned detection is an important difference since it offers increased sensitivity and allows for the elimination of the bias which plagues the other techniques. Temporal modulation of the scanning pattern is accomplished by shifting the frequency of the plane wave using an acousto-optic modulator prior to superimposing the fields. As the FZP is scanned over the object, the scattered light is collected and integrated by a photodetector or a photomultiplier tube (PMT), resulting in a current which contains 3D information in the form of a hologram.

In OSH the plane wave and spherical wave originate from a single laser operating at wavelength $\lambda_0 = 2\pi c/\omega_0$, where c is the speed of light and ω_0 is the operating frequency of the laser in $radians/second$. The situation is shown in Figure 1. The laser beam is split into two paths at the beamsplitter (BS). The frequency of one path is shifted

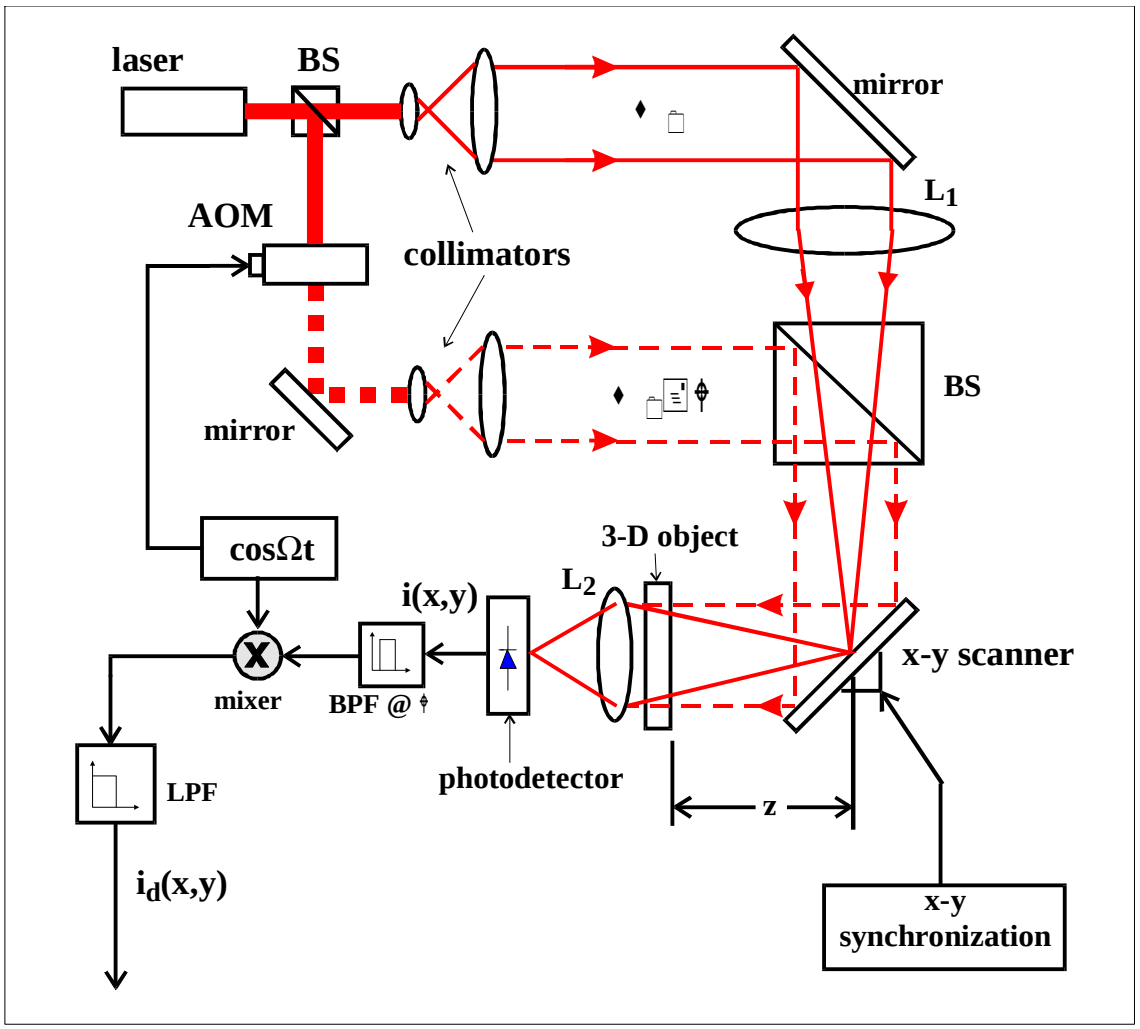

Figure 1 - Setup used for holographic recording by OSH
(BS: beamsplitter; LPF: lowpass filter; BPF: bandpass filter)

by directing the beam through an acousto-optic modulator (AOM) operating in the Bragg regime with drive signal $cos\Omega t$. The first order diffracted light at frequency $\omega_0 + \Omega$ is collimated and expanded into a plane wave, while other diffracted orders are blocked. The resulting first order light is expanded, collimated and directed by the second beamsplitter to the surface of a set of 2D scanning mirrors. The second beam from the laser is simply left at frequency ω_0 and is directed by a mirror to pass through a lens. The lens focuses the light which is then recombined collinearly with the first beam. The resulting interference pattern is the FZP laser field which has been derived previously.[20] The FZP is mathematically represented by

$$I_s(x,\, y,\, z;t) \,=\, A^2 + B^2 + 2AB sin\big(\tfrac{k_0}{2z}(x^2 + y^2) - \Omega t\big). \tag{1}$$

In equation (1), A^2 and B^2 are proportional to the initial intensities of the light beams, $k_0 = \omega_0/c$ is the wavenumber of the laser light, and z, as denoted in Figure 1, is the axial distance measured from the focus of the spherical wave. This interference pattern is scanned over the object with intensity transmittance or reflectance $|\Gamma(x,y,z)|^2$. The transmitted or reflected light is collected by a photodetector or a PMT. The configuration shown in Figure 1 is the configuration used for a transmissive object. The scanning action results in the spatial convolution of the scanning field intensity and the object, thus encoding each object scatterer by a FZP.

Some insight into the OSH process may be gained by taking a simple example. Let the object transmittance be a single scatterer $|\Gamma(x,y,z)|^2 = \delta(x - x_0, y - y_0,\, z - z_0)$. The resulting heterodyned output current from the PMT at frequency Ω is proportional to[24]

$$i_\Omega(x,y;z,t) \propto sin\big(\tfrac{k_0}{2z_0}\left[(x - x_0)^2 + (y - y_0)^2\right] + \Omega t\big). \tag{2}$$

This current contains the holographic information pertaining to the off-axis point object. In order to extract this information, the signal is electronically multiplied by $cos(\Omega t)$ and lowpass filtered. The resulting demodulated signal i_d is given as

$$i_d(x, y) \propto sin\left(\frac{k_0}{2z_0}\left[(x - x_0)^2 + (y - y_0)^2\right]\right), \tag{3}$$

which contains the location (x_0, y_0) as well as the depth (z_0) information of the point object. To preserve and record the phase of i_d, a DC bias signal is added. The resulting signal is a hologram of the off-axis point source object :

$$t(x, y) = i_d(x, y) + bias. \tag{4}$$

This hologram can be displayed on a television monitor or sent to a video digitizer to be converted to a digital image for storage and/or processing.

2.3 EBSLM-Based Image Reconstruction

The two primary means of image reconstruction that have been investigated are real-time image reconstruction using an electron-beam-addresses spatial light modulator (EBSLM) and numerical reconstruction. Due to the incredible progress made in computers in recent years, numerical methods for image reconstruction have improved and become the standard technique in these experiments. For real-time applications though, EBSLM-based reconstruction are very important and are addressed briefly here. Numerical reconstruction is addressed in detail in Chapter 3.

Image reconstruction using an EBSLM is possible because of an electro-optic effect. The electro-optic effect employed by the EBSLM is a linear change in the refractive index of a $LiNbO_3$ crystal resulting from charge deposition on the crystal face. The linear electro-optic effect is called the Pockels effect.[27] Specifically, with no charges on the crystal face, linearly polarized light passing through the crystal results in linearly

polarized light out of the crystal. However, if charges are present on the crystal face, linearly polarized light passing through the crystal will result in elliptically polarized light out of the crystal.[28] The EBSLM contains an electron gun which deposits the charges on the face of a 55 degree cut $LiNbO_3$ crystal. One face of the crystal is coated with MgO to increase secondary electron emission, while the other face is coated with a highly transparent conductive film electrode for controlling crystal voltage.

In the reconstruction stage of the optical scanning holographic system, the primary function of the EBSLM is to modulate coherent light in accordance with a serial input video signal. The coherent light modulation system is shown in Figure 2. The EBSLM Controller accepts a video signal as its input and directs this signal to an electron gun and deflection coils located in the EBSLM head. The intensity of electron emission from the electron gun is modulated by the input video signal. The deflection coils create a magnetic field to steer the electron beam so that it sweeps the crystal back and forth and up and down in a raster fashion. This process is analogous to the functioning of a cathode ray tube. The electron gun and deflection coils deposit the 2D spatially modulated charges onto the $LiNbO_3$ crystal, resulting in the accumulation of charges in the pattern of the hologram. The Pockels effect changes the refractive index of the crystal on a point-by-point basis (see Figure 2), and thus modulates the incident coherent linearly polarized light according to the hologram pattern. Using an analyzer, the linearly polarized light is passed and allowed to illuminate a screen at a distance z away, while the elliptically polarized light is blocked. The resulting modulated light projected onto the screen is the hologram pattern.

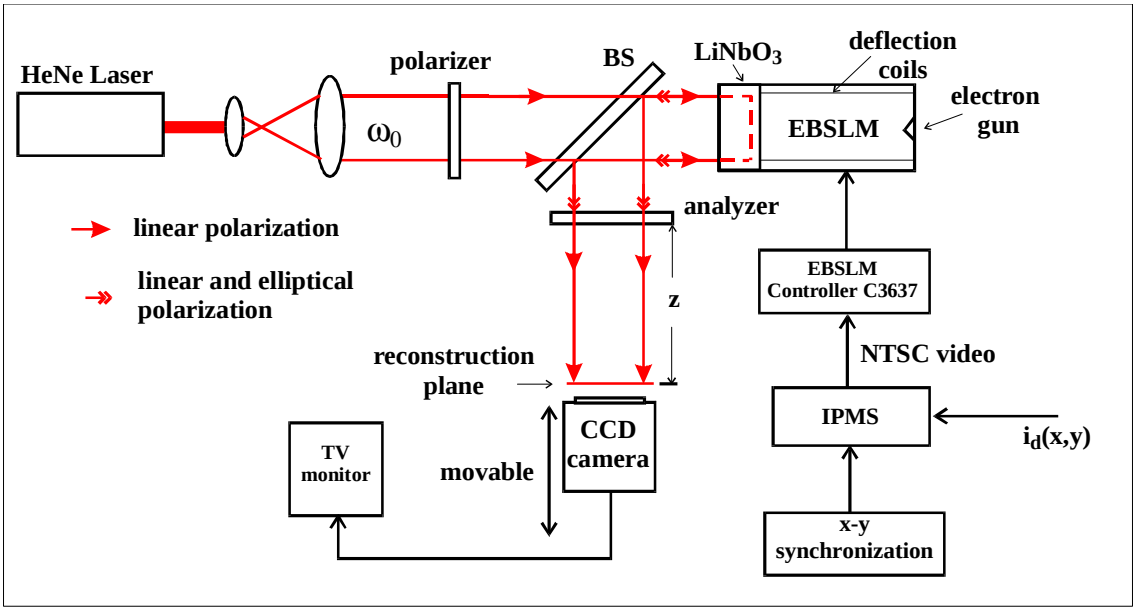

Figure 2 - Reconstruction using an EBSLM

3.0 Computer Simulations

Computer modeling and simulation have become increasingly important aspects of modern research, and the OSH project is no exception. The main reason for computer-based modeling and analysis is verification of experimental data by reconciliation with theory. The equations developed in Section 2.2, coupled with digital image processing and Fourier analysis techniques, are used to create computer generated holograms and image reconstructions for comparison with experimental findings. As with the experimental portion of the OSH project, the computer simulations and associated programs have undergone many iterations of development. The earliest simulations were one-dimensional (1D), which is equivalent to taking a 1D slice through the hologram or image reconstruction. From these relatively simple algorithms (based on discrete, 1D convolution) stemmed valuable insight, particularly concerning alternate scanning patterns.[29] As progress continued, and powerful PC's became more affordable, this simple code evolved into a complex set of software applications which model every aspect of the OSH system in two dimensions. One of the first successful results of the computer model was the extension of the 1D study of alternate scanning patterns to two dimensions. We showed that by careful design of the scanning field, real-time processing of holographic information of an object could be achieved during recording. As an example, we created a computer generated hologram that exhibited enhanced edges upon normal image reconstruction.[24]

Although the verification aspects of the computer model are extremely useful, the simulations have taken on an even more important role in the reconstruction process of OSH. The algorithms have proven to be so robust that numerical methods have become the standard means for image reconstruction of both optically and computer generated holograms. So in some regard, the simulations have become an integral part of the OSH experiment, as opposed to a validating tool. This section includes a discussion of the

programming involved in the modeling of the system. Modeling the OSH recording stage begins with a digital representation of an object, typically consisting of simple shapes (points and/or lines) stored as a simple binary image file. A computer generated hologram is generated based on the mathematical constructs of the OSH system. Finally, another algorithm numerically reconstructs the real image of the original object from the hologram.

3.1 General considerations

As stated previously, the algorithms developed to model and analyze the OSH system consist of a complex group of programs which simulate the physical processes, along with several support functions. The programs are written in the C/C++ programming language using a WATCOM (1995) compiler. Since it is compilable, C/C++ code gives better performance than commercial mathematics packages such as MatLab or MathCad, although the algorithms may be easier to develop using these packages. The experimental "data" are objects, holograms and image reconstructions. The simulated versions of the data consist of 2D arrays of floating point numbers. Any 2D array of numbers can be viewed as an image file after undergoing normalization and conversion processes.

For standard gray scale images, normalization consists of converting the array of floating point numbers into pixels represented by single byte integers between 0 and 255, inclusive. The pixel corresponding to the largest number in the data is set to 255 (white), while the pixel corresponding to the smallest number in the array is set to 0 (black). Intermediate numbers are assigned a pixel value, P_n, according to the following linear normalization equation:

$$P_n = \frac{x - xmin}{|xmax - xmin|} \times 255, \tag{5}$$

where $xmin$ is the smallest real data value, and $xmax$ is the largest. The size of a typical data array is 256×256. Even though they are more computationally demanding, larger data arrays, such as 512×512, can also be handled by the algorithms. The choice to use the relatively small array size is based on acquisition time for optically recorded holograms. Details are included in the experimental section.

The second, and more demanding process involved in viewing numerical data, is the conversion from a normalized array of integers to a standard image file format. There are many commercial software applications for the conversion from one standard image file format to another. However, since a simple 2D array of integers is not a standard image file format, the commercially available software cannot be used. The image data in all standard image files is preceded by several descriptive lines of data, called "headers". Headers contain information telling the software how to read the data, such as array size, color information, resolution, compression, and many other parameters. A custom support application was developed to take the raw image data and insert the appropriate header information so the file can be recognized and read by commercial software. Only one standard file type is necessary, since once the data is in a standard file format, it can be converted to any other format using the commercial software. The TIFF (Tag Image File Format) file format, one of the most popular and versatile standards, was selected.[30] There is also occasion to remove the header information from a standard TIFF file, thus leaving the straight data available for processing. A second support application was developed to delete the header from a TIFF file.

3.2 Convolution and the 2-D Fast Fourier Transform

The mathematics that describe the physical processes involved in holographic recording by OSH, as discussed in Chapter 2, involve 2D spatial convolution. Optically, a hologram is generated by scanning a FZP intensity pattern over an object and collecting the scattered light. The process is represented mathematically by the two dimensional convolution of the FZP intensity pattern with the object's intensity transmittance or reflectance. The 2D spatial convolution of two functions, $g(x, y)$ and $h(x, y)$, is defined by the following integration:[31]

$$g(x, y) * h(x, y) = \int_{-\infty}^{\infty}\int g(x', y')h(x - x', y - y')dx'dy'. \tag{6}$$

The mathematical rigors of the preceding integration can be replaced by the simpler process of multiplication by invoking the "convolution theorem," which relates convolution in the spatial domain to multiplication in the spatial frequency domain. Explicitly, the convolution theorem states that the following are Fourier transform pairs:[32]

$$g(x, y) * h(x, y) \Leftrightarrow G(f_x, f_y)H(f_x, f_y), \tag{7}$$

where $G(f_x, f_y)$ is the Fourier transform of $g(x, y)$. The Fourier transform is defined as

$$G(f_x, f_y) = \int_{-\infty}^{-\infty}\int_{-\infty}^{-\infty} g(x, y)exp[j2\pi(f_x x + f_y y)]dxdy. \tag{8}$$

The convolution of equation (6) can therefore be calculated by multiplying the Fourier transforms of each function, and taking the inverse Fourier transform, as

$$g(x,y) * h(x,y) = \mathcal{F}^{-1}\{G(f_x,\, f_y)H(f_x,\, f_y)\}, \tag{9}$$

where $\mathcal{F}^{-1}\{\,\cdot\,\}$ denotes the inverse Fourier transform. Often, it is easier to compute the right hand side (RHS) of equation (9) than the RHS of equation (6). For numerical work, an even greater advantage of the convolution theorem exists because of a very computationally efficient algorithm called the Fast Fourier transform (FFT). A FFT is a digital approximation of a Fourier transform. To investigate the computational efficiency of this approximation, consider the following. To compute a discrete Fourier transform, on the order of N^2 complex multiplications, are necessary where N is the number of elements in the array. Using the FFT algorithm, the discrete Fourier transform can be computed in on the order of ($N \times log_2 N$) operations.[33] The difference between N^2 and ($N \times log_2 N$) is immense. A 256 x 256 complex data array contains 65,536 complex numbers. A computer that takes $10\,ns$ to perform a complex multiplication (one clock tick for a 166 MHz Pentium) can compute the discrete 2D Fourier transform of this array in about 42 seconds. The same computer, can compute the 2D FFT of this array in approximately 6.3 milliseconds. The FFT has been thoroughly studied and public domain code for computing the FFT algorithm can easily be procured. The routine used in this project comes from the outstanding reference: *Numerical Recipes in C.*[33]

3.3 The Sampling Theorem and Aliasing

Even with readily available algorithms, calculating the 2D convolution using FFTs can be tricky. One problem that deserves particular attention is involved with the sampling of continuous data at discrete intervals. It comes as no surprise that the consequences of the sampling theorem must be considered for computer simulations and numerical image reconstruction algorithms. What may not be obvious is that sampling effects are present in optically generated holograms as well. As mentioned previously, the

data in the OSH experiment exists in the form of images. Holograms, whether generated optically or by computer, are digitized, or sampled at evenly spaced intervals. Anytime a function or data is digitized, sampling and aliasing must be considered.

If we consider the sampling interval in the lateral direction to be Δx_s (which is always equal Δy_s for this experiment), then the reciprocal of Δx_s is the sampling frequency. There exists a critical value of sampling frequency, called the Nyquist frequency, defined as $f_n = \frac{1}{2\Delta x_s}$. The "sampling theorem" says that a function is completely determined by its samples if the continuous function is bandwidth limited to frequencies smaller than the Nyquist frequency.[33] Said another way, the sampling frequency, $f_s = \frac{1}{\Delta x_s}$, must be twice the highest spatial frequency in the continuous function or information is lost. Undersampling results in lost information and aliasing is said to occur. Aliasing considerations are critical and must be addressed for the OSH experiment.

First consider how sampling effects and aliasing come into play during the computer simulation phase and numerical reconstruction of OSH. Aliasing effects are particularly important when simulating the scanning pattern and the free space impulse response, so aliasing plays a major role in both simulations and numerical reconstructions. As seen in equation (1), the effective frequency of the FZP increases with increasing lateral distance from the origin. In order to eliminate the undesirable effects of aliasing, the simulated FZP functions must be artificially bandwidth limited. This is achieved by multiplying the scanning field with a Gaussian windowing function. The same situation exists during numerical image reconstruction with the simulated version of the free space impulse response. This topic is addressed further in the next two sections.

It is easy to see how the sampling theorem will effect the sampling step size when holograms are recorded optically as well. The sampling theorem criteria is met if two pixels are recorded (in each direction) for the smallest resolvable object. That is, the

sampling step size must be at least half the width of the smallest resolvable object. However, this is not the end of the story for OSH. A fact that is perhaps more subtle is that the sampling theorem pertains not only to the object being scanned, but to the scanning field as well. Only fringes that are twice the width of the sampling step size will contribute fringes to the final hologram. The situation is further complicated by the fact that the effective size of the FZP, and therefore the fringe spacing, changes with distance z. There are some complicated relationships between the size of the FZP, fringe spacing, necessary sampling step size and distance which are derived in Chapter 7.

3.4 Computer Generated Holograms

The theoretical treatment of holographic recording by OSH presented above shows that the process is mathematically equivalent to convolution of the object with the scanning field. Modern computer techniques suggest that the most efficient means of convolving data sets is with the FFT algorithm. In this section, the theory and computer techniques are coupled to create computer generated holograms consistent with the OSH recording technique.

The first step to a computer generated hologram is creating a simulated object. The object's intensity profile is designated $|\Gamma(x,y)|^2$. Again, experimentally real objects are used, such as slits, pinholes and transparencies of letters. Simulated objects are typically binary image files consisting of simple patterns. For instance a dot represents a point object, a line represents a slit object, or text is used for more complicated objects. Figures 3, 4, and 5 show example image files which represent simulated objects. The

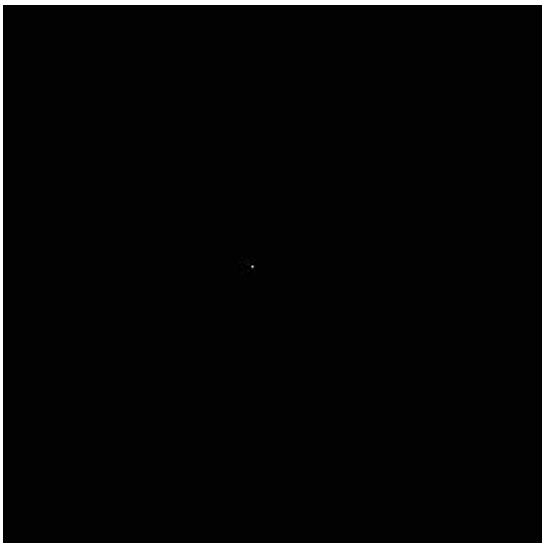

Figure 3 - Dot object

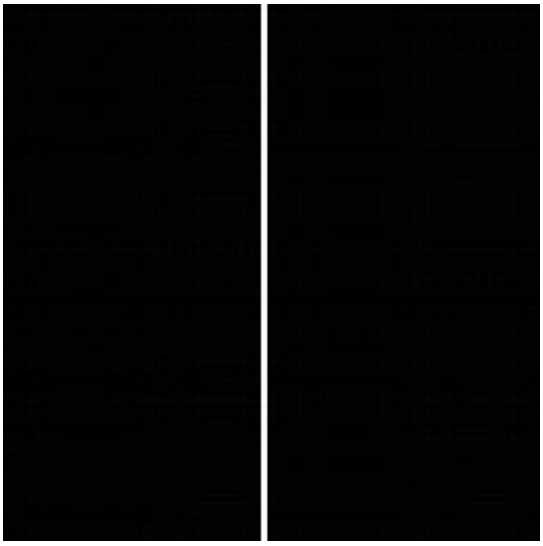

Figure 4 - Slit object

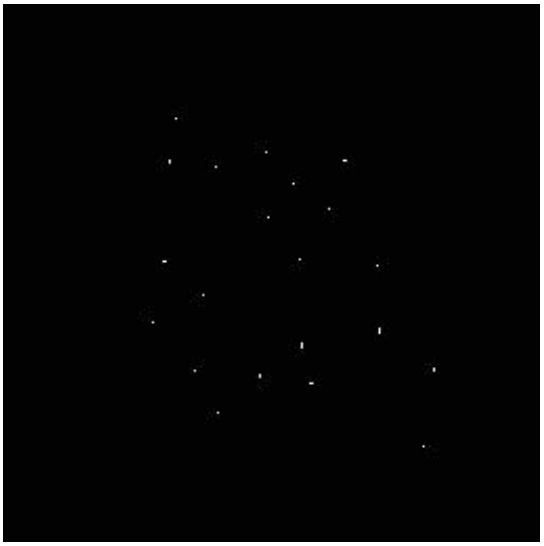

Figure 5 - Particle field object

images are 256×256 binary arrays. The array size is a power of two to allow for efficient use of the FFT algorithm. Object image files are easy to generate using C/C++ by simply storing an array which has a value of 255 for a white pixel and 0 for black. The TIFF conversion utility is used if the file must be viewed or printed. Alternatively, an object image file is generated using a standard graphics package, such as Microsoft Paintbrush or Corel Draw. Obviously, viewing the image is not a problem, as most commercial graphics programs have the ability to export files in the TIFF format. In this case the TIFF conversion utility is invoked to strip the header information, leaving only the data array available for processing. By making use of a combination of commercial graphics packages and the custom conversion utility, a file which represents an object may be generated. A digital representation of the scanning field is the second image file required to create the hologram.

The FZP scanning field can be modeled simply by using equation (1). Depending on the values of the variables in equation (1), the high frequency portions of the pattern at large radial distance can lead to aliasing and spurious results. As described in the previous section, FZP information having frequencies more than half the sampling frequency is useless. In practice aliasing effects are alleviated by multiplying equation (1) by a Gaussian windowing function. The Gaussian multiplier also makes sense physically because the actual optical scanning pattern exists in the profile of a laser beam. The laser beam intensity falls off approximately as a Gaussian. The equation used in the simulation is

$$I_s(x, y, z) = exp\Big[- \tfrac{2(x^2+y^2)}{w_{fzp}^2} \Big] sin\big[\tfrac{\pi}{\lambda z}(x^2 + y^2) \big], \tag{10}$$

where the subscript s refers to the simulated FZP intensity pattern, w_{fzp} is the Gaussian beam width at the object, and λ is the wavelength of the laser. Since the extent of the

scanning field is determined by the Gaussian multiplier, w_{fzp} is considered the width of the FZP as well. Beyond the waist, the Gaussian will diffract according to $w_{fzp} \propto \frac{\lambda z}{\pi w_0}$, where w_0 is the beam waist.

The support application which generates the numerical FZP accepts user input for the depth variable, z, for the lateral extent, x_{ext}, and for a Gaussian roll-off factor. A square image is always assumed, so $x_{ext} = y_{ext}$. One way to choose a reasonable roll-off factor for the Gaussian is to base it on the number of fringes, or zones, that will occur in the pattern within the $1/e$, (or $1/e^2$) point. Note that a zone (or fringe) consists of both a light and dark ring. The intensity, $I_s(x, y, z)$, will have a value $1/e^2$ times its maximum when the argument of the exponential is equal to two, or when $(x^2 + y^2) = w_{fzp}^2$. Beyond the Rayleigh range, $sin\left[\frac{\pi}{\lambda z}(x^2 + y^2)\right]$ has a cycle whenever $\left[\frac{\pi}{\lambda z}(x^2 + y^2)\right] = n2\pi$. Setting the lateral distance where the Gaussian is at the $1/e^2$ point to the lateral distance where the sine term has gone through N_z cycles, the following relationship is derived:

$$w_{fzp}^2 = N_z 2\lambda z. \tag{11}$$

The approximate number of fringes inside the $1/e^2$ point can therefore be determined by choosing a Gaussian beam width such that $w_{fzp}^2 = N_z 2\lambda z$. For $N_z = 10$ zones within the $1/e^2$ point, $w_{fzp}^2 = 20\lambda z$. For this case the FZP intensity pattern, shown in Figure 6, will be at $1/e^2$ of its maximum after 10 fringes. Perhaps twice that many fringes are actually visible. Note that the number of zone$s$ in the FZP was chosen rather arbitrarily here, but as is evident in the simulated holograms and image reconstructions that follow, 10 zones gives acceptable results. The concept of system design and evaluation based on the number of zones in the scanning pattern is intuitive. The topic has been touched on in the

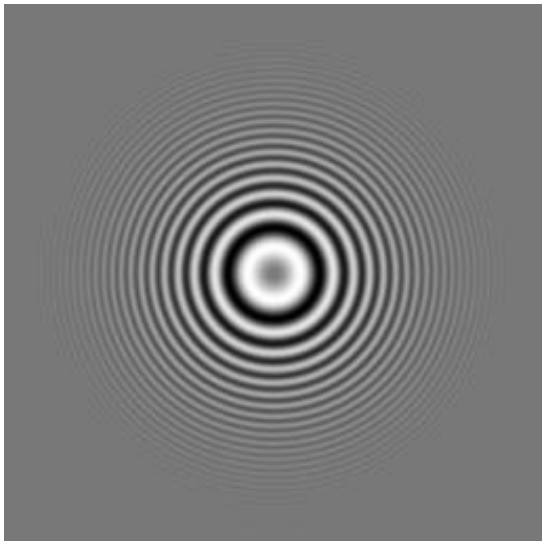

Figure 6 - Computer generated FZP for $x_{ext} = 1.92mm$, $y_{ext} = 1.92mm$, $z = 35mm$, $\lambda = 515\,nm$ and $N_z = 10$.

literature,[23] and will be investigated in some detail in later analysis. The number of zones in the scanning pattern has an effect on the resolution limit and depth of focus of the system.

Figure 6 shows the FZP for $z = .035\,m$, $x_{ext} = y_{ext} = .00192\,m$ and $N_z = 10$. The values for x_{ext}, y_{ext} and z are chosen to be close to the distances which were used experimentally. Holograms of area around $1.92\,mm \times 1.92mm$ are routinely recorded when dealing with microscopic objects (see Chapter 5). Similarly, the object typically will be about 3 or 4 cm from the focal point of the spherical wave. Obviously, since the pattern shown in Figure 6 is created by a computer, it is a sampled version of equation (10). Since the array size is 256×256 and the figure spans 0.00192 meters in the x and y directions, the sampling interval in the spatial domain, denoted $\Delta x_s = \Delta y_s = 1.92$ $mm/256 = 7.5\,\mu m$. The dimensions of the simulated objects are arbitrary, so it is reasonable to assign the same parameters for x_{ext}, y_{ext}, Δx_s and Δy_s to the object.

Once the object and scanning pattern have been generated and stored in the computer, the mathematical theory developed in Section 3.2 can be used to generate a simulated hologram. Specifically, the scanning pattern, $I_s(x,\, y,\, z)$, is convolved with the object intensity pattern, $\left|\Gamma(x,y)\right|^2$, to produce the hologram $t(x,y)$ as:

$$t(x,y) = \left|\Gamma(x,y)\right|^2 * I_s(x,\, y,\, z). \tag{12}$$

The convolution can be efficiently calculated by making use of the convolution theorem and the FFT algorithm as follows:

$$t(x,y,\, z) = FFT^{-1}\left[FFT\left\{\left|\Gamma(x,y)\right|^2\right\} \times FFT\{\, I_s(x,\, y,\, z)\}\right]. \tag{13}$$

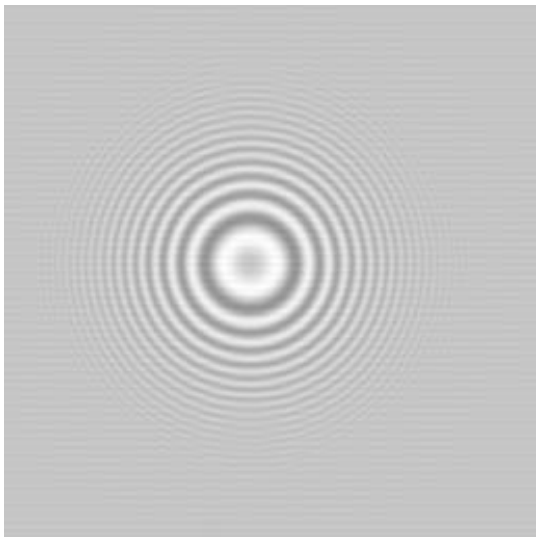

Figure 7 - Simulated hologram of the dot object shown in Figure 3

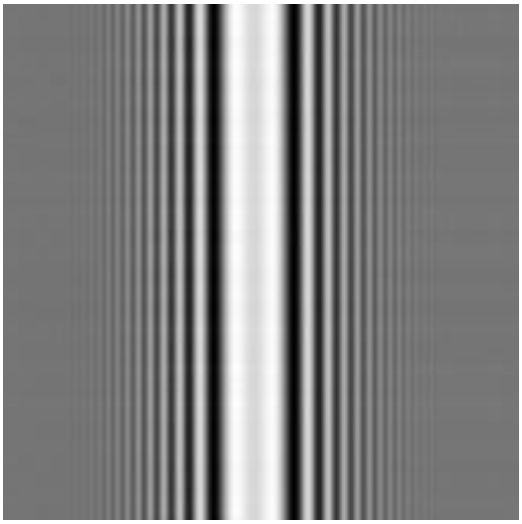

Figure 8 - Simulated hologram of the slit object shown in Figure 4

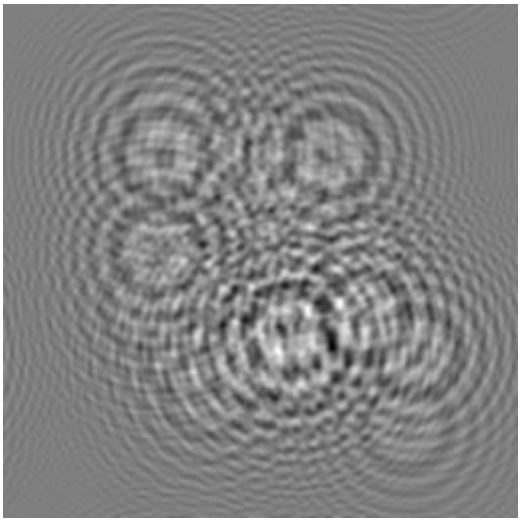

Figure 9 - Simulated hologram of the "particle field" object shown in Figure 5

Simulated holograms of each of the objects shown in Figures 3, 4, and 5 are shown in Figures 7, 8, and 9 respectively. Note that the hologram of the point object and slit object contain approximately as many fringes as the scanning pattern has zones. Although it is less obvious in the hologram of the simulated particle field, due to the more complicated fringe interference, each point in the object is represented by the same number of fringes as in Figures 8 and 9.

3.5 Numerical reconstruction

The numerical approach to image reconstruction has many advantages over optical reconstruction and has become standard practice for the OSH experiment. In practice, the real image reconstruction is achieved by passing a plane wave through the hologram and allowing it to propagate some distance z where the real image is in focus. We model this process numerically by convolving the hologram with the free space impulse response. Specifically, the intensity of the reconstructed image is given by

$$r(x,y;z) = |\, t(x,y;z) * h(x,y;z)|^2, \tag{14}$$

where $h(x,\, y; z)$ is the free space impulse response given by[34]

$$h(x,y;z) = \tfrac{1}{\mathrm{j}\lambda z} exp\big[- \tfrac{j\pi}{\lambda z}(x^2 + y^2)\big]. \tag{15}$$

Not surprisingly, the convolution of equation (14) is most efficiently computed by invoking the convolution theorem in conjunction with the FFT algorithm. Specifically,

$$r(x,y;z) = |\, FFT^{-1}\{FFT\,[t(x,y;z)] \times FFT\,[h(x,y;z)]\}|^2 \tag{16}$$

As with the FZP scanning field, the free space impulse response is by necessity sampled in a 256×256 array and a decaying exponential multiplier must be used to reduce the effect of aliasing. Note that since an equation for the Fourier transform of $h(x, y; z)$ is known, an equivalent approach is to use it directly in equation (16). The Fourier transform of the free space impulse response, called the spatial transfer function of wave propagation in free space, is defined as[34]

$$H(f_x, f_y; z) = \mathcal{F}\{h(x, y; z)\}$$

$$= \begin{cases} exp\left[j2\pi \frac{z}{\lambda}\sqrt{1-(\lambda f_x)^2-(\lambda f_y)^2}\right] & \text{for } \sqrt{(f_x)^2+(f_y)^2} < \frac{1}{\lambda} \\ 0 & \text{otherwise} \end{cases} \tag{17}$$

where f_x and f_y are the spatial frequency domain variables in the x and y directions, respectively. For a discretely sampled function, the relationship between the x and f_x is $f_x = 1/N\Delta x$ where N is the number of elements in the array. It can be especially advantageous to use equation (17) instead of equation (15) if the choices for x_{ext}, y_{ext}, and z lead to significant aliasing in equation (15). In this case equation (16) becomes

$$r(x, y; z) = \left| FFT^{-1}\{FFT\left[t(x, y; z)\right] \times H(f_x, f_y; z)\}\right|^2. \tag{18}$$

Reconstructions of the holograms presented in Figures 7, 8, and 9 have been created by implementing equation (18) and are shown in Figures 10, 11, and 12, respectively.

It is important to investigate the relationship between the size of the FZP and the object itself. For instance, using different parameters, a different scanning field is generated. Let the value for z used as the scan distance in the previous simulation be divided by about three. As expected, the FZP scanning field is smaller. Using a $z = 10$ mm and leaving the rest of the parameters unchanged results in a FZP as shown in Figure

13. A computer generated hologram made by convolving this scanning pattern with the particle field is shown in Figure 14. Notice that the fringes tend to interfere less in this hologram. The resulting image reconstruction of the particle field is given in Figure 15. It is easy to see that as the object gets more complicated, the fringes will distort the image reconstruction. This illustrates why twin image elimination can be very important for the OSH system. In addition to the reduction in distortion, however, the particle field points are more finely resolved using the "smaller" FZP. The resolution of the system is dependent on z. The relationships between z, resolution and FZP size are investigated in Chapter 7.

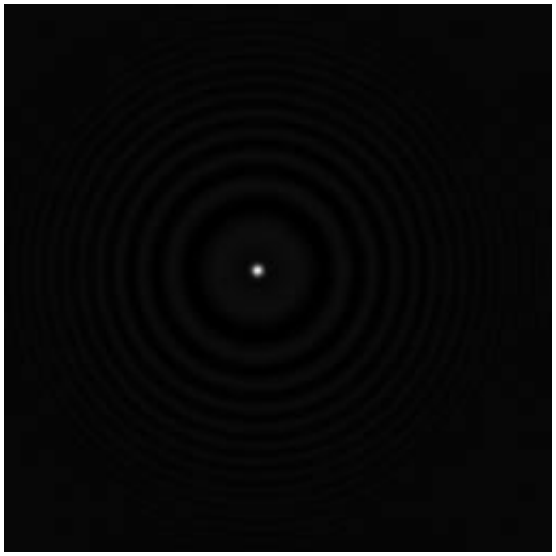

Figure 10 - Numerical image reconstruction of the dot object shown in Figure 3

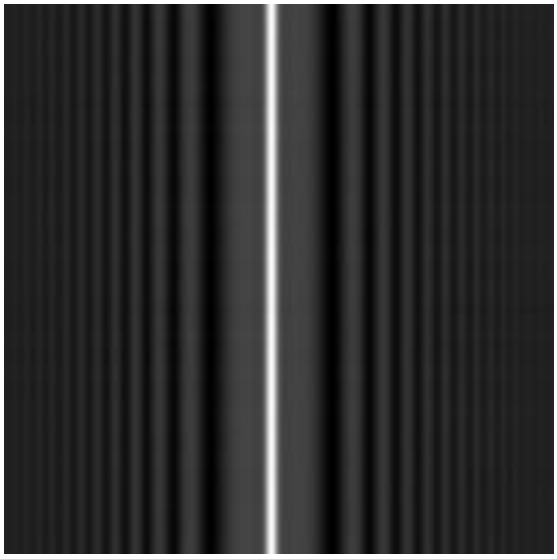

Figure 11 - Numerical image reconstruction of the slit object shown in Figure 4

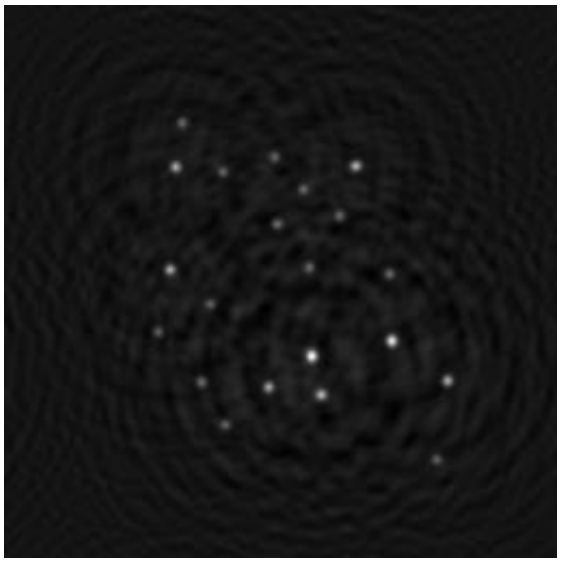

Figure 12 - Numerical image reconstruction of the particle field object shown in Figure 5

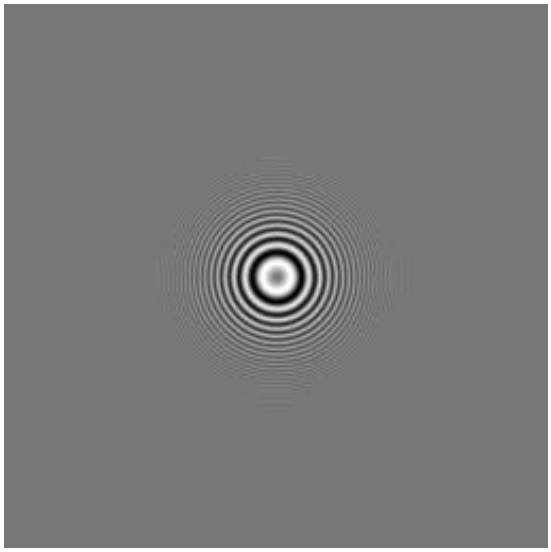

Figure 13 - Computer generated FZP for $x_{ext} = 1.92mm$, $y_{ext} = 1.92, z = 10mm$, $\lambda = 515\,nm$ and $n = 10$

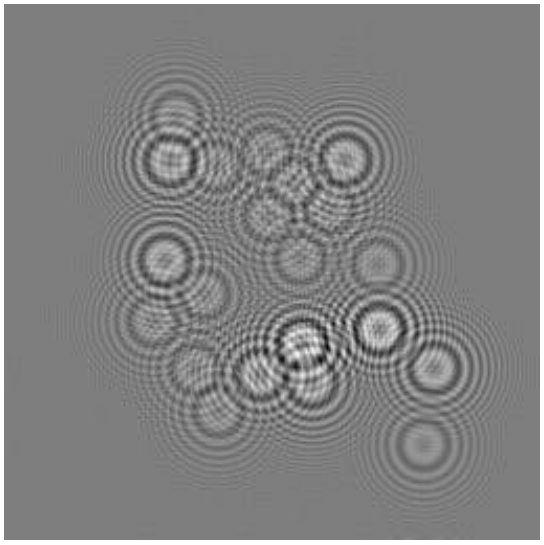

Figure 14 - Simulated hologram of the "particle field" object shown in Figure 5 using the FZP shown in Figure 13 as the scanning pattern

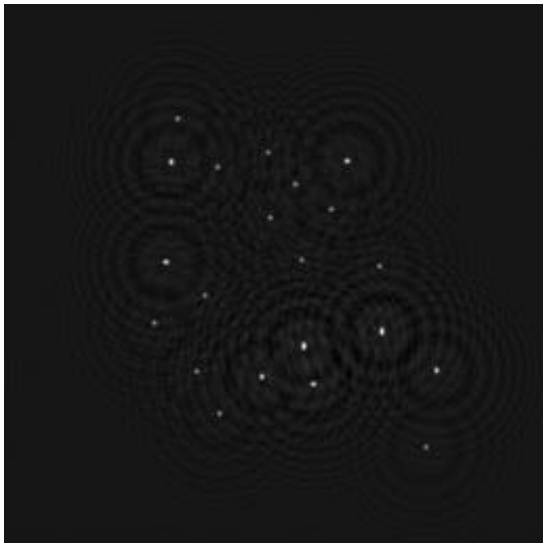

Figure 15 - Numerical reconstruction of the hologram shown in Figure 14

4.0 Selected Topics in Fluorescence

The discipline of cell biology was launched by the invention of the light microscope nearly 300 years ago. Despite its importance, however, this invention has been in jeopardy of being overshadowed by newer approaches to microscopy, such as the electron microscope. Recently, several new techniques have brought the light microscope back to the cutting edge of biological research. One of these innovations is the development of multicolor fluorescent dye molecules. Fluorescent dyes used as selective stains or markers have once again made light microscopy an indispensable technology for the observation of living cells. Fluorescent dyes can be linked to a variety of biological structures, allowing specific cell structures to stand out from their background.[35] A fluorescent molecule is one that absorbs a photon and quickly re-emits a photon of lower energy, and thus longer wavelength. For instance, the dye fluorescein absorbs light at a wavelength of 490 nm and in response emits light at 525 nm. This section considers the physical process of fluorescence in some detail and investigates how this mechanism is exploited by today's microscopist. Fluorescence microscopy has now matured to the point where it is commonplace to employ it in conjunction with laser scanning and confocal microscopy techniques, which enhance resolution and enable a three-dimensional imaging capability.[36-39]

4.1 The Physics of Fluorescence

The phenomenon called fluorescence is actually a specific type of a much broader class of phenomena called luminescence. There are a number of common types of luminescence including radioluminescence, electroluminescence, chemiluminescence, bioluminescence, thermoluminescence, and photoluminescence. Fluorescence is one of the

two types of photoluminescence, phosphorescence being the other. By definition, luminescence is the spontaneous emission of optical radiation (infrared, visible or ultraviolet) by matter. Under the proper conditions, luminescence manifests itself in a variety of types of matter including atoms; organic, inorganic, and organometallic molecules; polymers; organic and inorganic crystals; and amorphous substances.[40] One of the most straightforward ways fluorescence can occur is by the application of nonionizing radiation, such as visible or ultraviolet light, to matter. Under these conditions a stimulus photon is absorbed by the molecule, which accepts the energy by entering into an excited state. Some of the energy is then converted into rotational and/or translational energy, and the remainder is emitted as light of a lower energy than that of the stimulating photon. This process is investigated in some detail in the remainder of this section.

4.1.1 Absorption and Emission Spectra

Under normal conditions and at room temperature, the electronic state of a molecule will be its lowest possible energy state, known as the ground state. Outside stimuli such as visible or ultraviolet light can put the molecule in an excited state, where one or more electrons occupy higher energy orbitals than in the ground state. The multiplicity of an electronic state is defined in terms of the spin quantum number (S) of the molecule. The spin quantum number is the absolute value of the sum of the electronic spins in the molecule. The multiplicity of the molecule is then defined as the quantity $(2S + 1)$, and may be either singlet or triplet. In a singlet state there are an equal number of electrons with negative and positive spins in the molecule, or said another way, all the electrons spins exist in pairs. For the singlet state, $S = 0$ and the multiplicity is therefore 1. Conversely, a triplet state is one in which there is one unpaired set of electron spins, $S = 1$ and multiplicity is 3. Figure 16 has an orbital diagram associated with each electronic-state position in which the direction of the arrow symbolizes the electron's spin

value. The various energy levels of singlet states are referred to as S_0 (ground state), S_1, S_2 etc., and the triplet states are referred to as T_1, T_2, etc. Additional levels in the diagram are depicted by narrower lines which represent the molecule's vibrational energy levels. These vibrational levels are related to the vibration of the atomic nuclei.[41]

The arrows which go between various energy levels in Figure 16 represent electron movement from one state to the next. The dashed lines on the left represent a transition to an excited state brought about by the absorption of an incident photon of sufficient energy. The incident photon must possess energy equal to the energy difference between the excited state and the lower state (for this discussion, the lower state is the ground state) in order for the transition to take place. The initially excited state can be any one of a number of high energy or vibrational states. For this reason, a range of incident photon energies can produce an absorption transition. This range of possible photon energies results in a molecular absorption or excitation spectrum consisting of broad bands rather than lines. The excitation spectrum in a molecule is a measure of the probability of photons at a given wavelength being absorbed by a molecule. This probability depends on the availability of an appropriate transition between the ground state and some vibrational level of an excited state, with energy equal to the incident photon energy.

A molecule in an excited state will eventually return to the ground state. This process can occur through a number of possible paths. A return to the ground state can be nonradiative (depicted by dotted lines in Figure 16). An example of a radiationless transition, called internal conversion, is the generation of heat. An excited molecule may make a transition to an excited triplet state. This is called an intersystem crossing and is

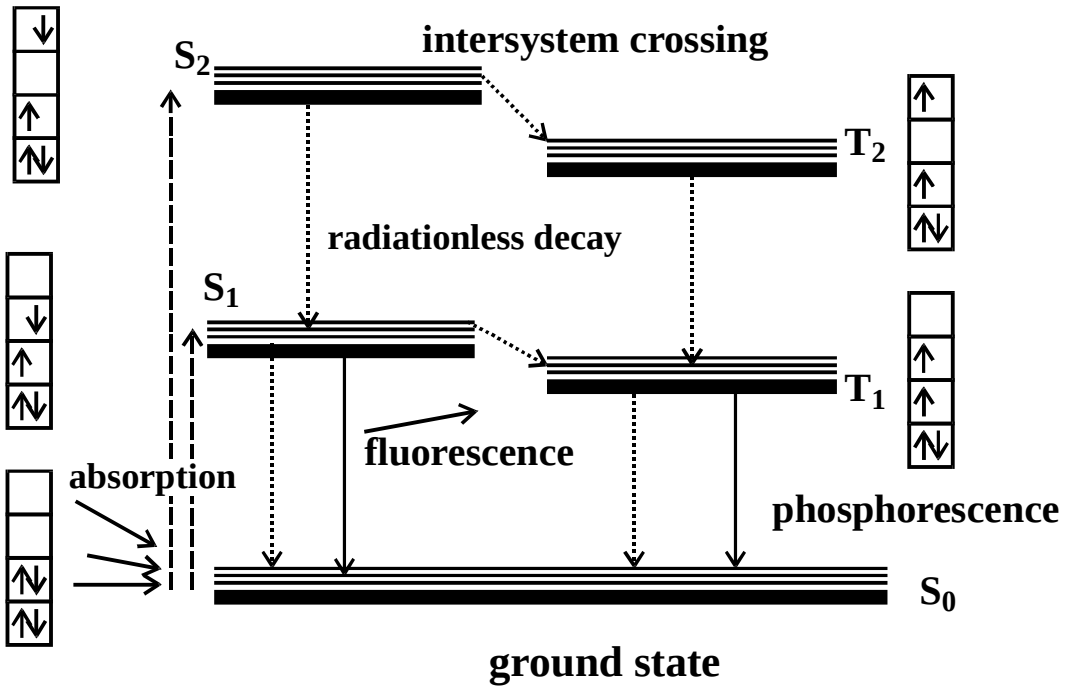

Figure 16 - Electronic state diagram showing fluorescence

also symbolized by dotted lines in Figure 16. From an excited triplet state, an internal conversion can also occur, from which no light is emitted. However, an excited singlet or triplet state may return to the ground state via radiative decay, shown as solid lines between states in the Figure 16. When an electron decays radiatively to a lower state, a photon is emitted. A radiative transition between a singlet state and the ground state which results in the emission of a photon is called fluorescence. Fluorescence is nearly always a result of a transition between the lowest energy level of the first excited singlet state and some vibrational level of the ground state. For a radiative transition from a triplet state to the ground state, which results in the spontaneous emission of a photon, the process is called phosphorescence. Phosphorescence has a longer lifetime than fluorescence. If the delay between absorption and emission is on the order of 10^{-8} seconds or less, the emission is called fluorescence. For a delay $\sim 10^{-6}$ the term delayed fluorescence is used, and a delay greater than $\sim 10^{-6}$ results in phosphorescence.[42]

Because the emitted photon has less energy than the excitation photon, the wavelength of the emission is almost always longer than that of the excitation. This is known as Stokes' law, and this type of fluorescence is sometimes called Stokes' fluorescence. Though less likely, photon emission at shorter wavelengths, called anti-Stokes fluorescence, is possible. This situation usually involves thermally excited molecules having highly populated vibrational energy levels. It is also possible to obtain re-emission of photons at the incident photon energy, a process called resonance fluorescence. This phenomena is observed only in solids and gases and is the basis of atomic fluorescence.[43]

Just as with the absorption spectrum, the emission spectrum for a typical fluorescent dye involves a band of wavelengths. A typical emission spectrum curve has a peak corresponding to the energy from the lowest S_1 vibrational level to a favored vibrational level in the ground state. Since fluorescence nearly always takes place between S_1 and S_0, the curve will fall off very steeply on the high energy side (shorter wavelength)

of the peak. The low energy side falls off less rapidly due to the more probable occurrence of transitions from the lowest S_1 vibrational level to an upper vibrational level in the ground state.

It is the finite difference between the peaks in the excitation and emission spectra, known as the Stokes shift, that makes fluorescent dyes useful in microscopy. Wavelength selective filters are utilized in the illumination and viewing stages of the microscope to separate and to collect the desired fluorescent emission from the undesired excitation light. A dye which exhibits a large Stokes shift allows for a greater ability to block unwanted radiation and to collect fluorescent emission. This results in improved performance.[44] As can be expected, fluorescent dyes are identified and quantified by their absorption and emission spectra. As an example, the peak excitation for rhodamine is approximately 570 nm, and the peak fluorescence wavelength is around 610 nm.[44] With the proper selection of narrow band optical filters, more than one dye can be used simultaneously in a single cell to distinguish different cell characteristics.

4.1.2 Fluorescence Lifetime and Quantum Efficiency

Along with excitation and emission spectra, two fundamental parameters which characterize a fluorophore are quantum efficiency and fluorescent lifetime. The quantum efficiency is the ratio of energy emitted to energy absorbed by a fluorescent molecule.[45] A high quantum efficiency is nearly always desirable in fluorescence experiments, as is the case with the OSH system. The fluorescence lifetime is defined as the average amount of time the molecule remains in the excited state prior to its return to the ground state.[46] Fluorescence lifetime differences may be used as a form of selectivity in a technique called fluorescence lifetime-resolved imaging microscopy.[47-48] The approach is to make use of some sort of gating based on the lifetime of different fluorophores. From an imaging viewpoint, the time-dependent selectivity is equivalent to a selectivity based on emission

wavelength or other spectroscopic properties.[49] Our interest in fluorescence lifetime, however, is rooted in the use of a heterodyned light field for excitation. The concept is important enough to the OSH experiment to warrant a brief discussion of fluorescence lifetime.

Two methods for measuring the fluorescence lifetime have gained wide acceptance, the pulse method and the phase-modulation method.[50] In the pulse method, the sample is excited with a short pulse of light and the time-dependent decay of the fluorescence intensity is measured. Ideally, an infinitely short pulse of light is desired for this excitation. Pulsed lasers can be ideal sources for this technique. In addition, subnanosecond UV light sources have been developed for this purpose.[51] In the phase-modulation method, the sample is excited with sinusoidally intensity modulated light. The phase shift and demodulation of the emission, relative to the incident light, is used to calculate the lifetime.[46] To see the direct bearing this method has on the OSH experiment, reconsider the generation of the FZP scanning laser field.

The FZP laser field is generated by superimposing a plane wave with a spherical wave from the same laser, but with a slightly different temporal frequency, resulting in an FZP which is temporally modulated. To apply OSH to fluorescent specimens, the FZP is generated at a wavelength near the peak absorption of the specimen and used as the heterodyned excitation field. If the fluorescence lifetime of the specimen is short enough, the fluorescence response is also temporally modulated, allowing its heterodyne detection. The frequency difference produced by a standard acousto-optic modulator (AOM) is $\Delta\Omega/2\pi = 40\,\text{MHz}$ or higher. Clearly, if the fluorescence lifetime of the sample is longer than the period of the excitation (25 ns for $\Omega/2\pi = 40$ MHz), the fluorescent specimen will be unable to respond. Note that the time required for absorption is negligible (~10^{-15} seconds) compared to the typical lifetime of fluorescence (~10 nanoseconds).[42] Although many fluorescent dyes have lifetimes less then 10 nanoseconds,[52] when a fluorescent sample is excited by a sinusoidal light field, the modulated emission is delayed in phase and

has a modulation index that is smaller than that of the excitation. The relationship for first order, single exponential decay is governed by the following equation from Lakowicz:[46]

$$m = [1 + \omega^2\tau^2]^{-\frac{1}{2}} \tag{19}$$

where m is the demodulation factor, ω is the frequency of modulation and τ is the fluorescence lifetime. With fluorescent signal at a premium, we have elected to use a unique AOM configuration to allow for the use of a beat frequency close to 10 MHz. The AOM configuration is described in Chapter 5.0.

4.1.3 Photobleaching

Some fluorescent molecules can be destroyed or damaged by the excitation process in the presence of molecular oxygen. This phenomenon is called photobleaching. Photobleaching is defined as the permanent destruction of fluorescence by light-induced conversion of the fluorophore to a chemically nonfluorescent compound.[42] It is important to note that photobleaching requires light and oxygen for most commonly used fluorophores. Since removing oxygen is not a viable option when studying living cells, the effects of photobleaching are usually reduced by regulating the light dose, or fluence, of the excitation. The fluence is defined as the intensity, or irradiance, of the excitation multiplied by the time of illumination. Traditionally, photobleaching has been controlled by reducing the fluence on the fluorophore by one of these alternatives: 1) short duration, high intensity illumination, or 2) longer duration and low intensity illumination. The first option is usually achieved using shutters, illuminating the fluorescent specimen in very short pulses. The second option requires very sensitive photodetection devices, such as PMTs. An interesting solution to the photobleaching problem called two-photon laser-scanning microscopy (TPLSM) has recently been developed.[53] Since the advantages of

the two-photon technique are particularly relevant to 3D microscopy, the topic is addressed more completely in a later section.

As stated previously, the rate of fading is dependent on excitation energy and period of exposure. Many factors effect the required excitation energy including the light source, the position of collector lens, the diffusion of light over the specimen, the magnification and numerical aperture, and the type of excitation filter used.[54] Through optimization of these factors, illumination can be reduced, though irradiation damage can rarely be avoided entirely by this means. Excitation irradiance levels below 50 μW/cm^2 are low enough to avoid irradiation damage.[55] This is equivalent to 1.3×10^{14} photons/second/cm^2. Since 3D fluorescence microscopy by OSH eliminates the multiple 2D scans required of current 3D microscopes, it is natural to assume that it will also have a great advantage over current methods in reducing excitation photo-damage. This aspect of the system is considered in some detail in Chapter 7.0.

4.2 Fluorescence Microscopy

There is more to microscopy of biological specimens than simply forming highly magnified, clear images. At magnification levels sufficient to image single cells clearly, most biological structures are colorless and transparent. In the absence of some mechanism to improve the contrast in such a specimen, important features may remain invisible. Traditionally, selective staining has been used to darken or color certain aspects of a specimen. However, as with the electron microscope, this type of specimen preparation kills living cells. Fluorescence microscopy has been successful at marking features of living cells and thus improving resolution and specificity.[35]

4.2.1 Fundamentals of Fluorescence Microscopy

The principles of operation for the fluorescence microscope are the same as for basic optical microscopy. The main difference is the incorporation of the appropriate optical filters at the excitation and emission wavelengths. The advantage of fluorescence microscopy is that an emission filter (sometimes called a blocking filter) can be inserted in the viewing stage of the microscope to block out the illumination light. In this way only light emitted by the specimen (or specific dyed feature of the specimen) is collected at the eyepiece or detector. The image of the object which fluoresces is bright on a dark background. A block diagram showing the basic components of the fluorescence microscope is given in Figure 17. The block diagram is identical to that of a standard optical microscope with the addition of a special source for illumination, and the filters required to exploit the excitation and emission characteristics described in the previous section. The most common form of illumination for the fluorescence microscope is an arc lamp. When coupled with a narrow-bandpass (or notch) filter, wavelengths of light near the absorption peak of the fluorescent dye are incident on the specimen. As described in the previous section, the specimen then fluoresces at a longer wavelength. In some systems, the excitation comes from a scanning laser. In this case, the source itself may be monochromatic and an excitation filter is not always necessary. Typically, if the specimen contains only a single absorbance wavelength, a longpass filter is used as an emission filter to maximize the light collection efficiency. In this manner, all light emitted above the cutoff wavelength of the excitation filter is collected. However, if multicolor dyes are being used simultaneously in a specimen, notch filters must be used for both excitation and emission.

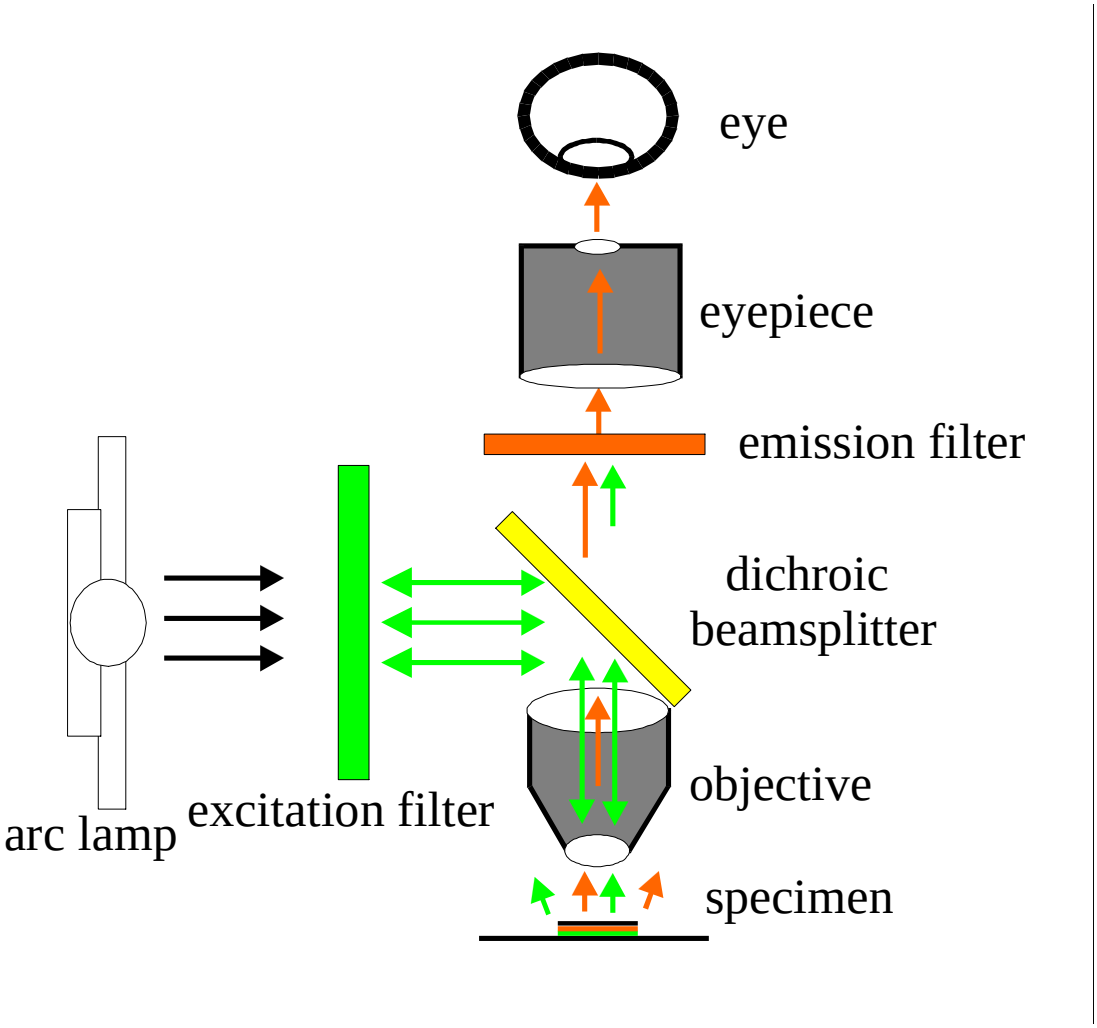

Figure 17 - Optical fluorescence microscope block diagram

4.2.2 Fluorescence Microscopy in Three Dimensions

The image obtained from a typical microscope is reminiscent of a 2D projection of a 3D object. Several methods have been developed to obtain a more accurate 3D portrayal of the original object from the 2D images produced by a standard optical or fluorescence microscope. These methods usually involve digital processing, computer storage, and sophisticated programs to reconstruct the data into a realistic image. The most obvious approach to microscopy in three dimensions is to generate a set of 2D projections at specified intervals of focus along the focus axis.[37] Confocal scanning microscopy accomplishes just that, proving to be one of the most exciting advances in optical microscopy in this century.[56] Researchers are currently combining the idea of fluorescence with confocal scanning microscopy to develop confocal scanning fluorescence microscopes.[36] Since confocal microscopy is such an important topic, a brief discussion of confocal techniques in fluorescence microscopy follows.

Consider the situation in which it is desired to image a single small area within a specimen, perhaps a single feature such as the nucleus of a cell. In conventional fluorescence microscopy the object is uniformly illuminated. As planes below the surface of a thick specimen are brought into focus, the image becomes more obscured with depth, quickly becoming incomprehensible. The image is obscured by fluorescent emission and scattering from particles in front of and behind the plane of interest, as well as the random scattering of light from all around the nucleus. The confocal scanning microscope achieves superior contrast and resolution, especially in the longitudinal direction, in the following manner. Refer to Figure 18, a simplified block diagram of a fluorescence confocal scanning laser microscope (CSLM). The CSLM is a variation of the confocal scanning optical microscope (CSOM) which uses an arc lamp or similar broad band source for illumination. In either case, the excitation radiation passes through a notch filter, a pinhole and an objective lens which focuses it to a point at a chosen depth in the object.

The benefit of this focusing action is readily apparent. Since the light is focused to a single diffraction limited point within the specimen, a much smaller amount of light passes through the object relative to conventional fluorescence microscopy with uniform illumination. Unwanted fluorescent emissions will only occur in an hourglass-shaped region of the thick object, reducing stray emissions and reflections which obscure the image. The region in which stray emissions and unwanted reflections occur is shown shaded in Figure 18 a). In this manner, stray light emissions from points to either side of the point of interest are eliminated. However, there are still fluorescent emissions from in front of and behind the plane of interest to consider. This image obscurant is controlled with a second pinhole aperture in the detection stage of the confocal microscope. The light emitted from the spot of interest is focused to a point at the second pinhole aperture, where it passes through in its entirety. The opaque material around the second aperture serves to block most of the remaining light which would otherwise obscure the image. Figure 18 b) shows in detail how the pinhole effectively blocks unwanted light from reaching the photodetector. In the figure, the detection stage of the confocal scanning microscope has been unfolded and the beam splitter removed for clarification. The solid lines represent the light fluorescing from the desired depth, which passes through the pinhole unhindered. However, unwanted light from in front of and behind the desired depth, is not focused to a point at the aperture and is thus blocked from reaching the photodetector. These stray emissions are represented by dashed lines in Figure 18 b). Of course, the blocking filter is inserted in front of the detector as in standard fluorescence microscopy to stop the illumination wavelengths from being collected. In this manner, a clear image of one single fluorescing point in the thick specimen is collected and recorded. The entire specimen is scanned in three dimensions to acquire a complete recording of the object.

The confocal configuration reduces both the area of illumination and the area

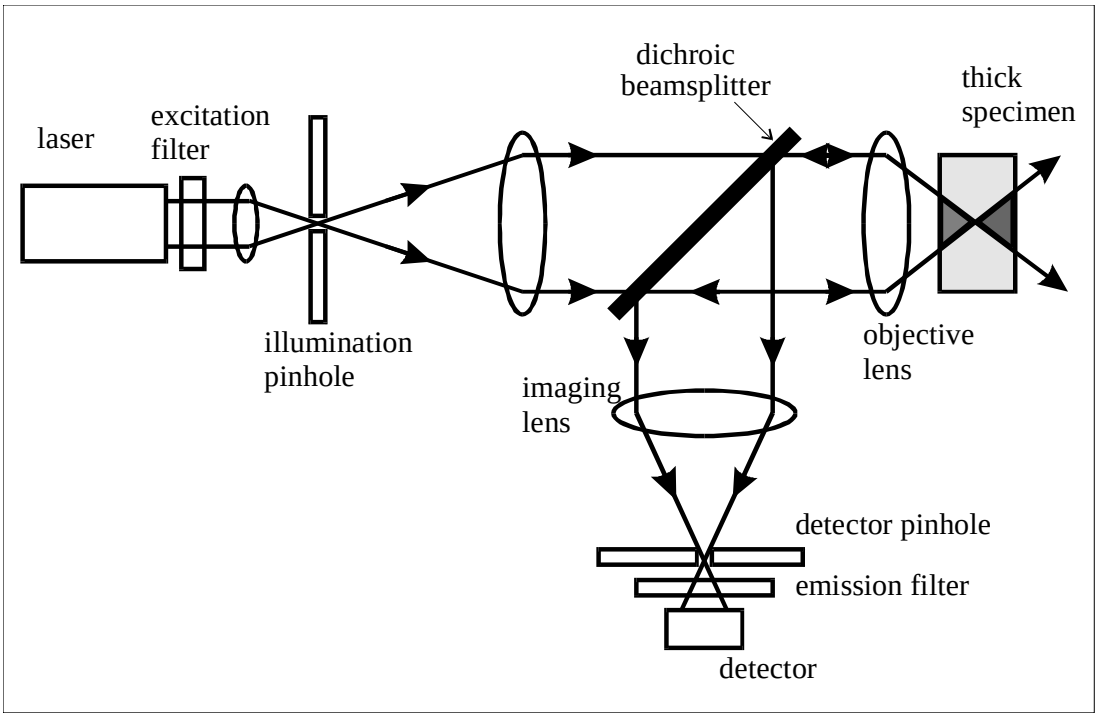

Figure 18 a) - Block diagram of the components which make up a confocal scanning laser microscope

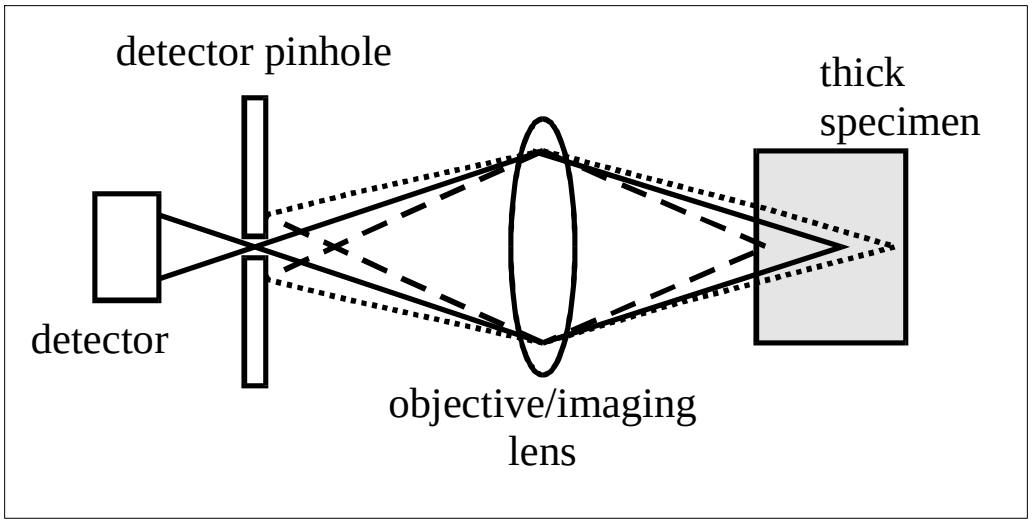

Figure 18 b) - Enlarged view of the focusing action in the specimen

from which the measurement is taken to near diffraction limited points. According to Rost, confocal techniques result in a resolution 1.4 times better than that of a conventional microscope.[41] In fluorescence microscopy the improvement in resolution is even greater. This comes about from the fact that the resolution of the confocal system is dependent on the excitation wavelength, rather than on the emission wavelength as in a conventional fluorescence microscope with uniform illumination. A confocal fluorescence microscope also has a unique depth discriminating property because out-of-focus planes are imaged with less intensity than the in-focus plane.[39] However, confocal techniques tend to exacerbate the photobleaching problem, since 10 to 64 images are routinely taken of a single sample. Solutions to photobleaching for confocal microscopy often involve the use of antioxidants[57] or limiting the number of sections recorded. The obvious drawbacks of these "solutions" have held the door open for further research in this area. Very promising solutions to the photobleaching problem for 3D imaging microscopy are two and three-photon microscopy techniques which very recently have been developed.

4.2.3 Two-Photon Laser-Scanning Microscopy

The two-photon (2-p) approach to laser scanning fluorescence microscopy is similar to the confocal technique, but causes much less photo-damage. The two-photon laser scanning microscope (TPLSM) was first demonstrated by Watt Webb and his co-workers in 1990.[58] The idea was originally proposed by Sheppard *et al.* as early as 1977.[59,60] As with the confocal technique, a laser beam is focused at the plane of interest within a labeled specimen and raster scanned across the focal plane. The fluorescence response is detected by a PMT to form the image. The advantage of TPLSM lies in the fact that the fluorescent label is excited only at the focus of the beam. This is accomplished by illuminating the specimen with a high power laser which emits at twice the wavelength of the absorption peak of the fluorophore. For example, a fluorophore

with peak absorption in the UV range of 350-400 nm can be excited in the 2-p mode with a high power laser emitting in the IR range of about 700-800 nm. The trick is to get two infrared photons to collide with a fluorophore simultaneously. The combined energy of two infrared photons excites the fluorophore in an identical way as a single photon of half the wavelength. After excitation, the fluorophore relaxes and fluorescent emission takes place as usual (see Section 4.1).

The statistics involved in having two low energy photons excite a fluorescent molecule at precisely the same time have been calculated. The power of the laser is adjusted so it is only probable that this occurs at the focus of the laser, where there is the highest density of photons. The process can result in a diffraction-limited spot being excited. The advantages of this technique are multifold.[53] Since there is no out-of-focus fluorescence, the dye is not bleached in the cone-shaped region shown in Figure 18, but only precisely at the diffraction-limited spot corresponding to the focus. This dramatically reduces photobleaching and phototoxicity. Since only a single spot is excited, the need for an aperture at the detector is eliminated. In CSLM, the aperture is a source of reduced SNR since some of the light is necessarily blocked by the aperture. TPLSM can therefore have a SNR advantage over CSLM as well, since all the fluorescent emission can be collected.

Imaging to greater depths is also possible with the 2-p technique. The reason is that IR wavelengths penetrate deeper into most specimens than UV or visible light. In fact Potter *et al.* have reported the capability to image two to three times deeper in certain tissue with TPLSM than with CSLM.[61] A final advantage of the 2-p technique is easy separation of excitation and emission. Excitation wavelengths will typically be anywhere from 700 nm to 1000 nm with the 2-p method. This leaves hundreds of nanometers of separation between the IR laser wavelength and the fluorescent emission, which will lie in the UV or visible spectrum. The technique has recently been elevated to three photon excitation. Serotonin distribution has been measured in live cells with this technique.[62]

There are a few disadvantages to the 2-p and 3-p techniques, most deal with the large and expensive laser necessary to achieve the high power, short pulse IR radiation. The most versatile pulsed IR laser for TPLSM is a mode-locked, titanium-doped sapphire (Ti:Sapphire) laser which requires an 8-10 W argon-ion pump laser. The system is tunable from 700-1000 nm, allowing 2-p excitation of fluorophores usually excited in the UV, blue or green region of the spectrum. These lasers are quite a deterrent to the widespread acceptance of TPLSM since they consume a significant amount of power (10-20 kW) and currently have a high price ($\sim$ \$135,000).[53] Also, the theoretical resolution of a TPLSM system is worse than that of CSLM by a factor of about two, since the excitation wavelength is about twice as long.[63] Be that as it may, researchers have reported sharper images using TPLSM versus CSLM on the same specimen.[53] This is because theoretical resolution is seldom achieved in CSLM when living specimens are imaged. The laser power must be attenuated to reduce photo-damage and a larger-than-optimal confocal aperture must be used to obtain a reasonable signal-to-noise ratio.

Fluorescence microscopy has become a requisite tool for biologists, particularly for the study of living cells. The ability to link fluorescent dyes to separate biological structures has enabled researchers to study specific cell structures in living cells. Fluorescence microscopy takes advantage of the ability of some molecules to fluoresce, or emit light of a characteristic wavelength when excited by another wavelength. Image contrast is improved by using filters to facilitate the fluorescence process and block interfering illumination radiation prior to viewing. Recent developments involving scanning confocal techniques linked with fluorescence have also led to improved resolution and depth discrimination. Two and three-photon techniques in conjunction with confocal methods show great promise in reducing photo-damage in living specimens. The fundamental processes involved in fluorescence have been reviewed and a brief description of how this phenomenon is used in microscopy has been presented.

5.0 Experimental Setup

The experimental setup for optical scanning holography described in Section 2.2 was designed in the late 1980's to demonstrate the principle of OSH. Although holographic fluorescence microscopy is theoretically the same as the original version of OSH, the experimental setup is different in many ways. The modified experimental setup is discussed in the following sections, with emphasis on the specific changes which have been made to accommodate fluorescent specimens. Since the system is theoretically identical to standard OSH, it is not necessary to repeat any theoretical constructs. In addition to the use of optical filters in the illumination and light collection stages of the experiment (as with fluorescence microscopy), alterations to the setup have impacted the laser source, AOM configuration, x-y scanning and light collection apparatus. A discussion of the specific component changes made to the setup and considerations about each is included in Section 5.1. The complete system is described in Section 5.2 before experimental results are presented in Chapter 6.

5.1 Important components

Several changes to the standard OSH setup described in Section 2.2 are required in order to make the system suitable for holography of fluorescent specimens. These alterations are addressed on a component level before reviewing the experimental setup in its entirety.

5.1.1 Argon-Ion Laser

A good place to begin the component-level overview of the experimental hardware is with the argon-ion laser source. Since the conception of OSH, a HeNe laser has always been employed in the experimental setup, primarily due to its low cost and high reliability. Therefore, the use of a different laser source represents a major change to the system. The reason for the using the argon-ion laser is its emission wavelength, a critical parameter when excitation of fluorescent specimens is involved. The HeNe laser emits red light, near $632.8\,nm$, while the multiline argon-ion laser emits at six wavelengths in the blue-green region of the spectrum. The blue-green region is optimum for exciting many common fluorescent specimens, including ethidium bromide (EX: $482\,nm$), ethidium bromide bound to DNA (EX: $515\,nm$), Fluorescein (EX: $488\,nm$), and Rhodamine B (EX: $520\,nm$) to name a few.[44]

The air-cooled, multiline argon-ion laser is manufactured by Uniphase (model number 2014-40ML). The laser is CW with a total output power of $40mW$. The output power is distributed between six output wavelengths according to according to Table 1.

Table 1 - Power output by wavelength

Wavelength (nm)	Percent Power
457.9	8%
476.5	12%
488.0	20%
496.5	12%
501.7	5%
514.5	43%

The distribution of power given in Table 1 is theoretical and will change by a few percent based on the gas mix and other factors. The most important line for our experiment is the most powerful, the $514.5\,nm$ line which is used to excite the fluorescent beads used in our

experiment. At maximum output power, dial selectable, the argon ion laser will emit 17.2 mW of CW light at $514.5\,nm$.

As discussed in Section 4.1, absorption of radiant energy by a fluorescent molecule can take place over a relatively wide acceptance band of wavelengths. In practical fluorescence microscopy, more than one laser line can be used to excite a fluorescent specimen. An advantage of using two or more laser lines is to maximize the fluence on the specimen, which results in greater fluorescent emission. It is only necessary to block laser emissions which overlap the fluorescent emission spectrum of the fluorophore, thus ensuring maximum separation between excitation and emission. For the OSH experiment, however, the multi-line emission of the argon-ion laser poses a problem. Since the angle of light deflection of the acousto-optic modulator is frequency dependent, the individual frequencies separate as they are deflected by the AOM, as if passing through a prism. When the raw argon-ion laser output is passed through an AOM operating in the Bragg regime, the output light will be blue on one side and green on the other. Since this frequency separation is not advantageous to our heterodyne detection scheme, a $515\,nm$ narrow band filter is placed immediately after the laser output. The filter has center wavelength of $515 \pm 2\,nm$ and full width half maximum (FWHM) bandwidth of 10 ± 2 nm.

5.1.2 Acousto-optic Modulator Configuration

Generation of the FZP laser field was discussed in Chapter 2. The field is generated by superimposing a plane wave with a spherical wave from the same laser, but with a slightly different temporal frequency, resulting in an FZP which is temporally modulated. To apply OSH to fluorescent specimens, the FZP is generated at a wavelength near the peak absorption of the specimen and used as the heterodyned excitation field. If

the fluorescence lifetime of the specimen is short enough, the fluorescence response is also temporally modulated, allowing its heterodyne detection.

The frequency difference produced by a standard AOM is $\Delta\Omega = 2\pi \times 40\,\text{MHz}$ or higher which was found to be unsuitable to excite the fluorescent specimen. Clearly, if the fluorescent lifetime of the sample is longer than the period of the excitation (25 ns for $\Omega = 2\pi \times 40$ MHz), the fluorescent specimen will be unable to respond. Although many fluorescent dyes have lifetimes less then 10 ns,[52] when a fluorescent sample is excited by a sinusoidal light field, the modulated emission is delayed in phase and the modulation index is smaller than that of the excitation.[46] The higher the frequency of excitation, the lower the modulation depth of the emission. With fluorescent signal at a premium, we have elected to use a unique AOM configuration to allow for the use of a beat frequency close to 10 MHz.

In order to use a commercially available 40 MHz AOM to generate two light beams separated in frequency by 10.7 MHz, we employ the innovative configuration shown in Figure 19. The choice of 10.7 MHz was dictated by the availability of electronics for filtering and amplification. The setup is based on mixing signals prior to injection into the AOM which will result in radio frequencies separated by $\Delta\Omega = 2\pi \times 10.7$ MHz and lying within the frequency bandwidth of the AOM. For this experiment, we use signals at $\Omega_1 = 2\pi \times 40$ MHz and $\Omega = 2\pi \times 5.35$ MHz. The resulting drive signal consists of two cosine signals separated by $\Delta\Omega$ according to

$$cos(\Omega_1 t) \times cos(\Omega_2 t) \;=\; \tfrac{1}{2}[cos(\Omega_1 + \Omega_2)t + cos(\Omega_1 - \Omega_2)t]. \tag{20}$$

As shown in equation (19), the multiplication of the cosine signals results in a drive signal made up of cosines at 45.35 MHz, and 34.65 MHz separated by the desired 10.7 MHz. Driving the AOM with this signal results in two 1st-order diffracted beams, with

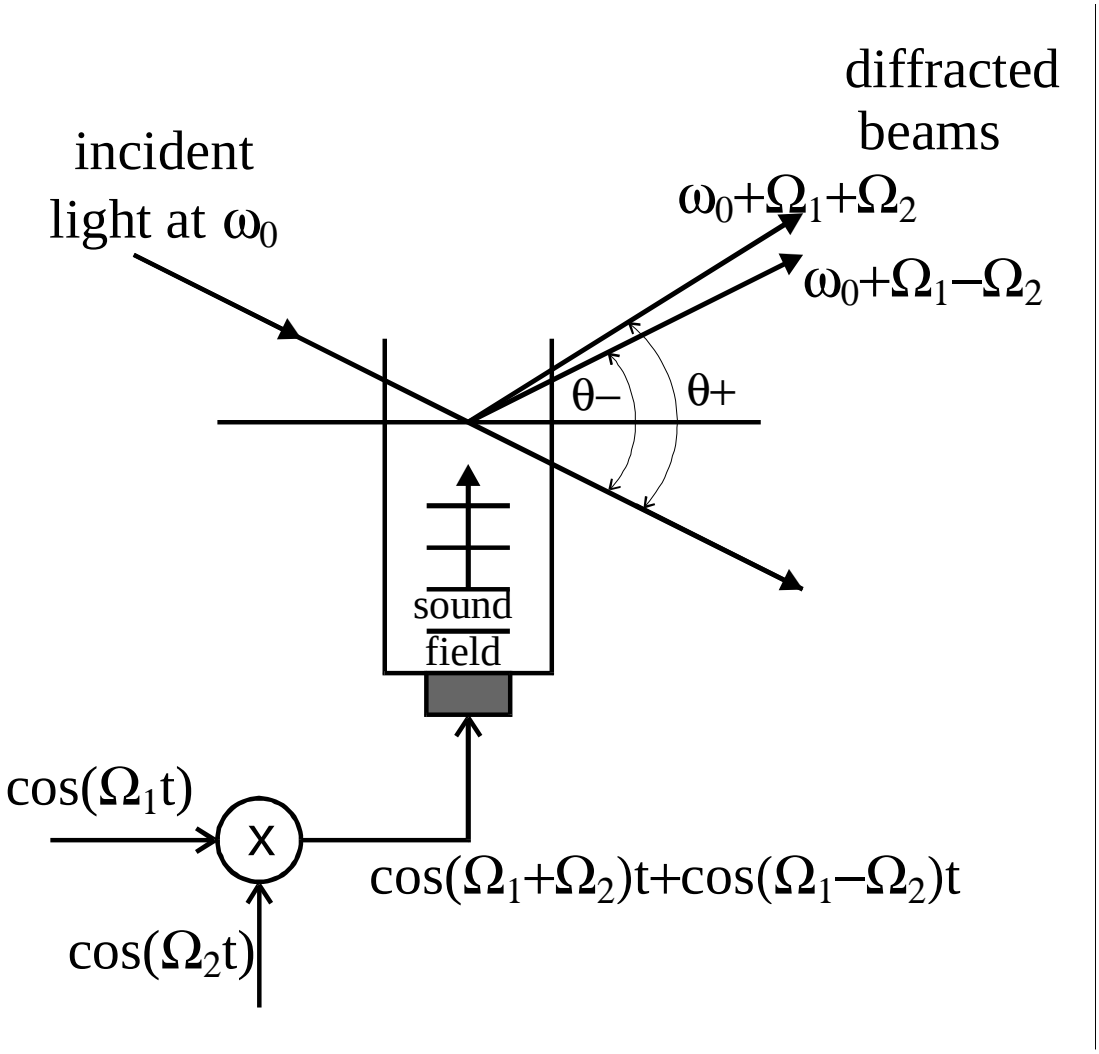

Figure 19 - Acousto-optic modulator configuration for the generation of two light beams separated by a temporal frequency difference of $2\Omega_2$.

frequencies

$$\omega_{\pm} = \omega_0 + (\Omega_1 \pm \Omega_2), \tag{21}$$

and angles of deflection[31]

$$\theta_{\pm} = (\lambda_0/2\pi V_s) \times (\Omega_1 \pm \Omega_2). \tag{22}$$

In equation (22), $\lambda_0 = 2\pi c/\omega_0$ is the wavelength of the incident light, and V_s is the speed of sound in the glass of the AOM. From equations (21) and (22) we see that the difference in temporal frequency between the two diffracted beams is $2\Omega_2/2\pi$ or 10.7 MHz, and the two beams are angularly separated by $2\Omega_2(\lambda_0/2\pi V_s)$. For our system, using $V_s = 4000 m/s$ and $\lambda_0 = 515 nm$, the angular separation is about 65 mrad (3.8°).

5.1.3 AOM Drive and Demodulation Electronics

Two things that make the drive and demodulation electronics more complicated than in previous OSH experiments are the AOM configuration described above, and the low signal levels involved in detecting fluorescence signals. In order to generate the drive signals for the AOM as described in Section 5.1.2, two radio frequency (RF) signal generators are required. A block diagram of the electronics is shown in Figure 20. With RF generators operating at 40 MHz and 5.35 MHz, a frequency doubler must be used to obtain the heterodyned frequency, 10.7 MHz, for demodulation. To avoid excess loading of the signal generator, a signal splitter is used between the mixer and the doubler. The signal splitter and frequency doubler are passive devices manufactured by Mini-circuits.

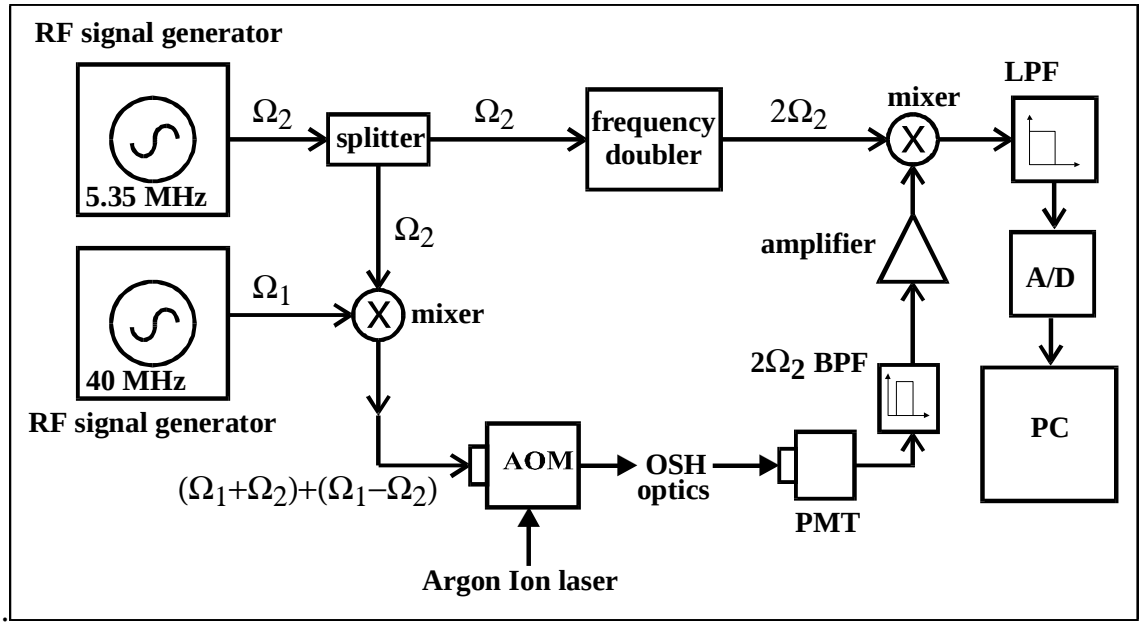

Figure 20 - Block diagram of the electronic setup used to generate the AOM drive signals and demodulate the PMT signal in holographic fluorescence microscopy. AOM: Acousto-optic modulator; PMT: photomultiplier tube; BPF: bandpass filter; LPF: lowpass filter; RF: radio frequency; PC: personal computer

The light levels involved in fluorescence microscopy are very low, so a PMT must be used to collect the light. The signal out of the PMT, already amplified appreciably, must undergo additional amplification and filtering to detect the heterodyned signal. Two high-Q electrical bandpass filters and two amplifiers are in the electrical path between the PMT and the demodulation mixer. The filters are manufactured by Cirqtel, have center frequency of 10.7 MHz and a 5% bandwidth Butterworth response.[64] Two different amplifiers are used. The first is manufactured by Mini-Circuits and has a 19 dB gain. The second is a HP Amplifier with 40 dB gain. The combined gain of the two amplifiers is therefore 59 dB. One Cirqtel filter is placed in the signal path between the PMT and the first amplifier, while the other is placed after the second amplifier.

5.1.4 Scanning and Data Acquisition

The hardware involved in data acquisition is the final area of the experimental setup to be discussed at the component level. Any other loose ends will be included in the overall experimental setup discussion given in Section 5.2. The hardware components that achieve acquisition of the hologram include the scanning apparatus, photomultiplier tube (PMT) for light collection, and analog to digital (A/D) conversion after demodulation.

In an attempt to eliminate errors involved with the scanning method itself, the new setup employs 2-D mechanical scanning platforms. This scanning method replaces the beam scanning configuration used in previous OSH experiments. With beam scanning, the object is stationary and the beam is directed by a set of 2-D scanning mirrors controlled by galvanometers. The FZP is scanned over the object in a raster fashion and diffracted light from the object is collected to form the hologram. There are some sources of error and distortion inherent in galvanometric scanning which are not present for a mechanical scan.[65] One of the main sources of distortion associated with beam scanning stems from the relationship between scanning distance and angle. At the outskirts of the object, the

scan distance will actually be slightly longer than at the center. Other errors include "pincushion" error and focusing error. Focusing errors are particularly a problem in postobjective scanning systems, such as ours. Since the scanning mirrors direct the beam after the focusing element (lens L_1 in Figure 1), the FZP becomes distorted during scanning. The fact that the mirror surface is offset from the axis of rotation is another source of errors. For experiments involving microscopic objects, the added distortion of the galvo-based scanners was deemed unacceptable. We elected to use a mechanical 2D scanning system because it is very precise. A disadvantage of the mechanical scanner is that it is slower than beam scanning, due to the mass that must be physically moved. To scan a 256×256 pixel image covering an area about 2 mm $\times$ 2 mm takes about 20 minutes. Acquisition time is proportional to area scanned and the number of pixels in the image.

The mechanical scanning system includes two motorized scanning stages with PC interfacing hardware and software. The mechanical, single-axis translation stages can be purchased separately from the controller. The PC interface and controller, manufactured by Newport/Klinger, is called the MotionMaster 2000.[66] When two scanning stages are stacked at 90° with respect to each other and used in conjunction with the MotionMaster 2000, very precise, software controlled positioning along two axes is possible. The MotionMaster 2000 has two 16-bit microcontrollers to achieve exact positioning. The user sends commands which tell the MotionMaster 2000 the distance, direction, speed and acceleration of the next move. The MotionMaster 2000 can also be instructed to send system status information to the controlling computer, such as position during movement, a "movement complete" signal or an error signal. A custom software application was developed to direct the scanning platforms, via the MotionMaster 2000, to scan back and forth and up and down, in a raster fashion. The software simultaneously acquires the hologram through an A/D board in synchronization with the scanning. The MotionMaster 2000 and custom software replace the Galva Scan Controller and CX-660 scanner drivers.

This hardware, not available for this experiment, was used in the previous OSH setup to drive the scanners and convert the demodulated current into a NTSC video signal.[20]

As the fluorescent object is scanned through and excited by the FZP, the fluorescent light is collected by a photomultiplier tube (PMT). The PMT replaces the photodiode due to the very low light levels involved in fluorescence microscopy. The PMT is manufactured by Hamamatsu (model number R1221, used in conjunction with socket E934). The PMT has characteristic current amplification of 4.2×10^5 and an anode pulse rise time of $2.6\,ns$. To collect the fluorescence signal, the PMT not only has to be extremely sensitive to low light levels, but the background and excitation light must be rejected. This is accomplished by placing a high quality narrow bandpass optical filter over the collection aperture of the PMT. A filter specially designed for fluorescence applications was purchased from Corion. The filter is Corion XM-595, with center wavelength of $590\,(+5,\,-0)\;nm$ and FWHM bandwidth of $35 \pm 3.5\,nm$. At the center wavelength, the filter has peak transmittance, $T_{pk} \geq 65\%$. The filter has high rejection of out of band wavelengths. Transmission is less than $0.01\%\ T_{pk}$ outside of a 1.7 times FWHM bandwidth. In addition, the transmittance curve of the Corion filter is not symmetric about the center frequency, but falls off less rapidly for longer wavelengths. For the XM-595 the transmission is $\leq 10^{-9}\ T_{pk}$ below $560\,nm$, making the rejection ratio at the laser wavelength more than 1,000,000,000 : 1.

The A/D board, called a DAQ Lab-PC+ manufactured by National Instruments,[67] acquires the hologram by converting the analog voltage out of the demodulation electronics (see Section 5.1.3) to a digital signal in sync with the scanning signals. The DAQ Lab-PC+, along with the custom software, effectively replaces the DVS 3010/SS Frame Memory and some functions of the Galva Scan Controller used in the previous system.[20] Again, these components were not available for the holographic fluorescence microscopy effort. The Lab-PC+ board has a 12-bit successive-approximation A/D converter with eight analog inputs. Since the Lab-PC+ board can be set for bipolar (± 5

V) or unipolar (0-10 V), it is not necessary to add a DC bias to the demodulated current prior to display or storage of the image.

5.2 3-D Holographic Fluorescence Microscopy

The experimental apparatus is described in Figures 19-21. Figure 19 shows the acousto-optic interaction producing the two beams, Figure 20 shows the electronics used to generate and demodulate the signals necessary for the experiment, and Figure 21 shows the optics which define the light path in OSH. Many of the individual components incorporated in the experimental setup discussed below were already been discussed in some detail in the previous section.

The 514 nm line of the argon-ion laser is selected by a narrow bandpass filter placed immediately at the laser output. This radiation is incident on the Bragg cell of the AOM operating as described in the previous paragraph and shown in Figure 19. This results in two beams separated in frequency by 10.7 MHz and in angle by about 3.8°. In order to spatially separate the beams, they are bounced between two mirrors and expanded by a 10x telescope. The beams are then collimated and made parallel to each other by the long focal length lens, L_1. Lens L_1 is uncoated, has a 76.20 mm diameter and a 400 mm focal length. After passing through lens L_1, the beams are parallel plane waves about 1 cm in diameter, with different temporal frequencies and separated by about 3 cm.

The Fresnel zone pattern is created by passing one of these beams through a lens,

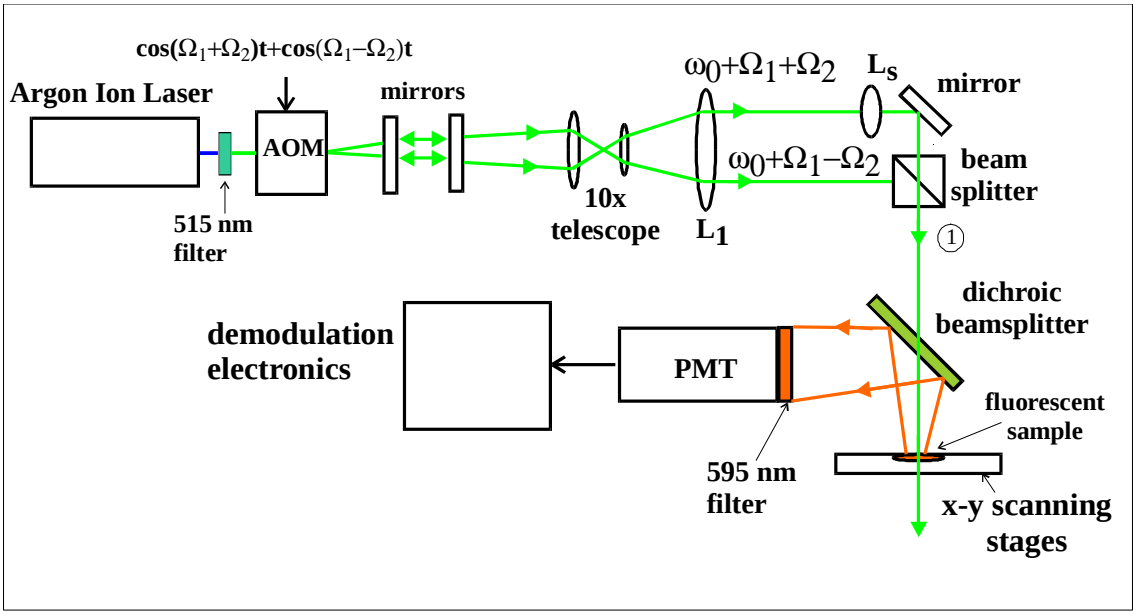

Figure 21 - Block diagram of the optical experimental setup used to record the hologram of a fluorescent specimen by optical scanning holography. AOM: Acousto-optic modulator; PMT: photomultiplier tube

thus forming a spherical wave, before recombining the beams collinearly. This is accomplished by lens L_s, a $1\,cm$ diameter lens with focal length $f = 150mm$. After passing through lens L_s, the spherical wave is immediately directed to the beamsplitter by a mirror to be recombined with the plane wave. This field, the superposition of the plane wave and spherical wave of different temporal frequencies, is allowed to propagate past the focal length of the lens L_s to illuminate the fluorescent object. After the focal point of L_s, the field is the diverging FZP. A dichroic beamsplitter is used to improve the separation of the illumination from the fluorescent response. The dichroic beamsplitter shown in Figure 21 transmits light at the excitation wavelength of the fluorescent specimen and reflects light at the emission wavelength. For this experiment the dichroic transmits light at $514\,nm$ and reflects light around $595\,nm$. Therefore, the laser light is allowed to pass through the dichroic beamsplitter and excite the fluorescent sample. The fluorescent sample consists of a solution with a high concentration of 15 μm diameter fluorescent beads having peak excitation at $530\,nm$ and peak emission at $560\,nm$. Laser light reflected from in and around the sample passes through the dichroic while the fluorescent emission is reflected, directing it to the PMT. The PMT, equipped with the $590\,nm$ narrow bandpass filter, collects and amplifies the fluorescent signal, converting it into a current. The current is filtered and amplified prior to demodulation as described in Section 5.1.3. The demodulated current contains the holographic information of the fluorescent object, exactly as described in Section 2.2. This analog current is digitized by the A/D board, in sync with the scanning signals, and the hologram is recorded and displayed by the computer.

The previous paragraphs describe the experimental setup used to illuminate the fluorescent object and collect the data necessary to record a hologram of this object. Functionally, the process is as follows. The laser, AOM, and front-end optics are used to generate a time-dependent FZP at the object plane. The FZP comes about from the interference of the plane wave and the spherical wave. The FZP is an intensity pattern in

the light itself, consisting of concentric dark and light rings. Due to the different temporal frequencies of the two laser beams, the FZP is also intensity modulated at the beat frequency, which is 10.7 MHz. In effect, the FZP is turning on and off 10.7 million times a second. The intensity modulation at the beat frequency allows the final signal to be detected using a heterodyned detection method. With heterodyned detection, a weak signal can be pulled out of the noise by electronic multiplication and filtering at the heterodyned frequency. The fluorescent object is placed in this illumination pattern and fluoresces accordingly. For a single image pixel, the intensity of the fluorescence will depend on the object's position relative to the stationary FZP. The PMT (with optical filter) collects the fluorescent emission and converts the light signal into a current. After amplification and demodulation, a voltage corresponding to the fluorescent intensity is presented to the computer's A/D board. This voltage is again in accordance with the relative position between the fluorescent object and the momentarily stationary scanning pattern. The computer digitizes and records the voltage level, lighting a pixel of the hologram with intensity proportional to the voltage. The computer program, which controls the scanning and data acquisition, instructs the scanner to move the object in the scanning beam to the position where the next pixel value will be recorded, and the process repeats. The object is scanned through the beam in a raster pattern, while the appropriate pixel values are stored until the entire hologram has been recorded and displayed. Due to the nature of convolving the object with the FZP in this manner, the recorded image is a hologram of the fluorescent object. It contains 3-D information as described in Section 2.2.

The final aspect of the experimental setup is the selection of an appropriate fluorescent dye. Typically in fluorescence microscopy, the choice of dye will depend heavily on physical and biological constraints. For instance, one dye might be better for studying the cell nucleus, while another dye may attach itself more readily to molecules in the cytoplasm. A commercial fluorescent microscope is equipped with a set of optical

filters for these various dyes. This is not the case for our prototype design. We have one optical filter set which is entirely dependent on the fluorescent dye we choose. Luckily, our choice is not constrained by any real physical or biological constraints at this "proof-of-principle" stage in the experiment. Originally we had planned to use cells stained with ethidium bromide (EB) as a fluorescent sample. EB is excited by radiation in the band around $515\,nm$ and has peak emission at $590\,nm$. This broad Stokes shift is one reason we selected EB. The filters used in our experiment, as shown in Fig. 2, reflect this choice of fluorescent dye. Unfortunately, several factors make EB a less than optimum choice for our experiment. Perhaps the most important factor is the quantum efficiency of EB, which is relatively low, below 50%. In addition, when bonded to DNA, the fluorescent lifetime of EB is in the 20 ns range.[51] It is advantageous to have the highest quantum efficiency and shortest fluorescent lifetime possible for our experiment. Also, cells stained with EB have a tendency to lose some of their fluorescing ability after several months of storage.

We also considered 15 μm diameter fluorescent beads with peak excitation at 530 nm and peak emission at $560\,nm$. These beads are promising specimens because they have a quantum efficiency near 100%, have broad excitation and emission bands, and have a fluorescence lifetime shorter than 10 ns.[44] Even with our slightly mismatched filters, the beads gave superior performance to EB stained cells. For the experimental results presented in Chapter 6, a solution containing a high concentration of these orange fluorescent beads was used as the fluorescent object.

6.0 Experimental Results

Using the experimental setup described in Chapter 5, the first holograms of fluorescent objects were recorded. Imaging fluorescent objects holographically is a unique and little studied problem. A preliminary investigation of the response of the fluorescent specimens to an optically heterodyned signal was conducted. These preliminary findings are presented for completeness. Positive preliminary results encouraged us to record holograms of fluorescent objects. A hologram was recorded of fluorescent beads situated in such a way as to be in close proximity laterally, but at different longitudinal depths. This hologram is representative of the final thesis results. It shows that holographic recordings of microscopic fluorescent objects are feasible with this technique and emphasizes the 3-D imaging capability.

6.1 Preliminary Fluorescence Results

The first experiment was designed to investigate the response of the fluorescent object at the chosen heterodyne frequency. Until it could be proven that the fluorescent object could be modulated at the heterodyne frequency, the technique had little hope of success. Ensuring that the fluorophore's fluorescence lifetime is less than the period of the heterodyned signal is not enough, since the modulation index of a fluorescent signal will always be less than that of the excitation signal. In addition, saturation of the fluorescent object is a major concern. Consider an excitation light signal with a low modulation index. Low modulation index corresponds to the relatively small AC modulation of a large DC signal. If the DC light is at a level such that the fluorescent specimen has close to 100% of its electrons in the excited state, it is said to be in saturation. For this case, the AC modulation of the already high DC signal will have no appreciable effect on the fluorescing

intensity. These concerns could only truly be alleviated experimentally by recording the fluorescent response to an optically heterodyned signal.

It may not be obvious that the heterodyning of two plane waves is much stronger than that of a plane wave and spherical wave, but this is indeed the case. In practice, the heterodyned signal is typically reduced by a factor of 10 upon introduction of lens L_s into the laser beam (see Figure 21). Therefore, to maximize the chances of recording the fluorescent response to the heterodyned signal, lens L_s was removed from the setup. The two plane waves now interfere at position 1 in Figure 21, forming the maximally heterodyned light field. The excitation field produced without lens L_s can be written as

$$I(t) = A^2 + B^2 + 2ABcos(\Delta\Omega t) \tag{23}$$

where A^2 and B^2 are the individual intensities of the two plane waves. This intensity, modulated at 10.7 MHz, measured by a photodiode at position 1 in Figure 21, is shown in Figure 22. The zero level in Figure 22 is at the '4-' in the lower left hand corner. Notice the reduced modulation depth, which can be detrimental to the experiment with fluorescent specimens. The poor modulation index is due to the unequal beam intensities caused by a nonuniform frequency response of the AOM and unbalanced, imperfect optics. Again, a large DC level may have detrimental consequences when used to excite fluorescence as it may saturate the sample, masking the modulated response. After recording the excitation signal at position 1, the light is allowed to pass through the dichroic beam splitter and onto the fluorescent bead solution.

The fluorescent beads absorb the radiation and respond by fluorescing as described in Chapter 3. The fluorescent emission is relatively broad-band with a peak

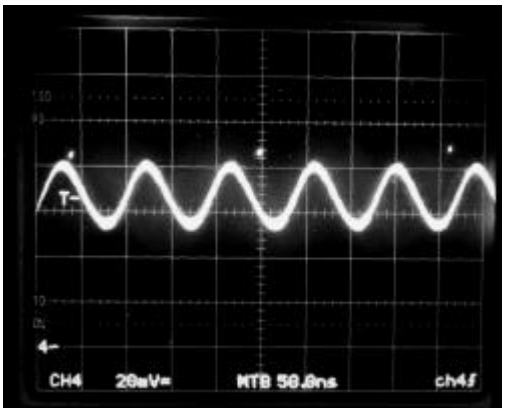

Figure 22 - Oscilloscope trace showing the measured heterodyned laser field used to excite the fluorescent specimen. The scope is DC coupled with 0 volt DC level at the '4-' in the lower left hand corner. The voltage scale is 20 mV/div and the time scale is 50 ns/div.

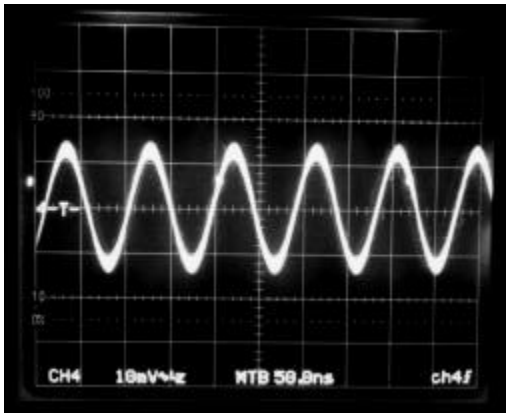

Figure 23 - Oscilloscope trace showing the measured fluorescent response to the heterodyned laser excitation after filtering and amplification. The scope is AC coupled with 0 volt level at the center. The voltage scale is 10 mV/div and the time scale is 50 ns/div.

wavelength near $560\,nm$. This fluorescent signal is reflected by the dichroic beam splitter, passed through the $590\,nm$ narrow bandpass filter and into the PMT. The signal is electronically filtered and amplified at 10.7 MHz before being displayed on the oscilloscope. A resulting fluorescence signal due to the heterodyned excitation is shown in Figure 23. The trace in Figure 23 is AC coupled so the 0 volt DC level is in the center of the screen. These preliminary results show that the fluorescent beads, and by extension, a fluorescent dye-stained specimen, respond to a heterodyned excitation field at 10.7 MHz and indicate that fluorescent holography by OSH is feasible. With the feasibility of the technique demonstrated by this experiment, the setup was reconfigured for holographic recording, by inserting lens L_s, and experimental results were taken.

6.2 Fluorescence Holograms by OSH

To reconfigure the setup for holographic recording, lens L_s was put in place, as shown in Figure 21. The modulated FZP excited the fluorescent sample. The sample was scanned using the computer controlled x-y scanning stage and the fluorescent light collected by the PMT. The PMT current, containing the three-dimensional information of the object was demodulated and digitized in sync with the x-y scanners to produce an electronic hologram.

As with the preliminary results, the fluorescent sample was the solution containing a high concentration of fluorescent latex beads. To demonstrate the depth discriminating capability of the system, a small amount of fluorescent solution was placed on the ends of two wires. These wires were then positioned next to each other, parallel to the optical axis, but with their ends at slightly different distances from the focus of lens L_s. The configuration of the fluorescent object is shown in Figure 24. The

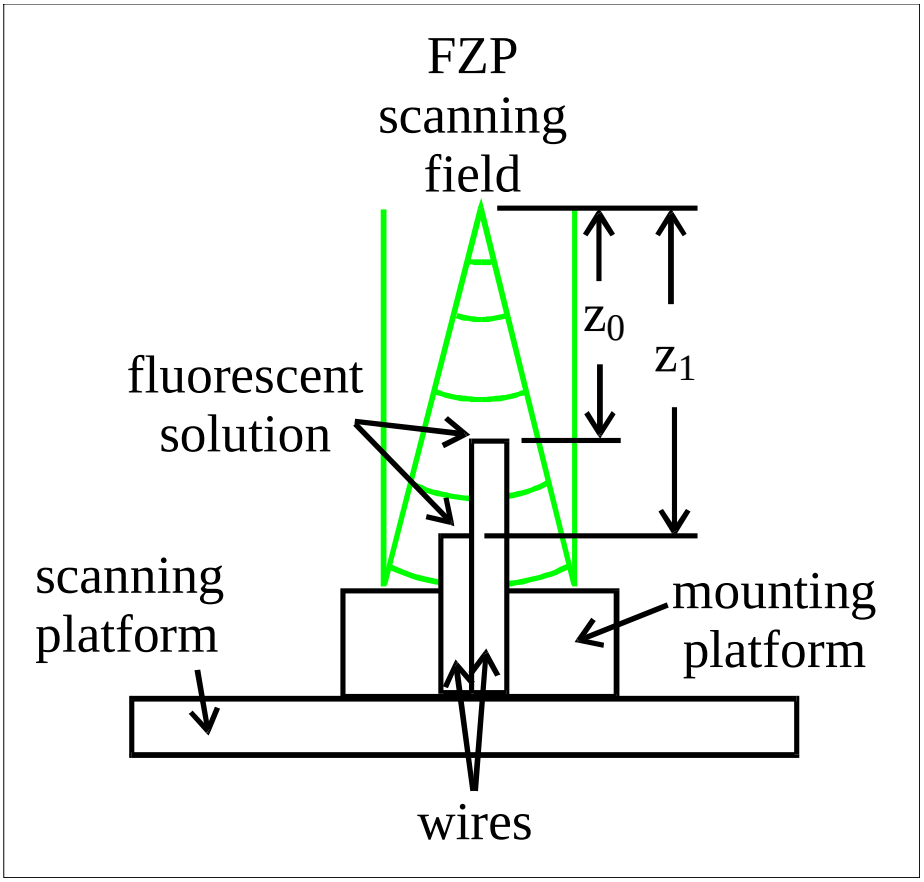

Figure 24 - Experimental configuration of fluorescent solution on the ends of two wires

ends of the wires, and therefore the two drops of solution, are separated in depth by approximately 2 mm, with the drop on the left at $z_0 \approx 35\,mm$ and the drop on the right at $z_1 \approx 37mm$. A hologram of this fluorescent sample was recorded and is shown in Figure 25. The area scanned to produce the hologram is about $2\,mm \times 2mm$. The hologram is a 256×256 array with intensity level represented by 256 gray levels. The two fluorescent drops are easily distinguishable in Figure 25.

Once the hologram (Figure 25) had been recorded and stored, the 3-D image could be reconstructed either optically or numerically. As described in Chapter 3, numerical image reconstruction is based on convolving the hologram with the free space impulse response corresponding to the desired depth z. Once again we emphasize the difference between the holographic technique and standard 3-D imaging techniques. In optical sectioning methods, the image is brought into focus at a chosen depth, say z_0, and the 2-D image for that plane is recorded and stored. This process is repeated for as many planes in z as desired, and an image must be recorded and stored for each plane. With OSH, a hologram of the object is recorded and stored with a single 2-D scan. Since all the depth information is stored in the hologram, any desired image plane can be brought into focus during image reconstruction. Numerical image reconstruction was performed on the hologram shown in Figure 25 for fifty different depths. The two images of particular interest are shown in Figures 26 and 27. Figure 26 is a reconstructed image at $z_0 = 34.5$ mm, and Figure 27 is an image reconstruction at $z_1 = 36.8\,mm$. Since the individual attributes in each fluorescent drop are not obvious in Figures 26 and 27, arrows have been overlaid on the figures to point out certain areas of interest. In Figure 26, the fluorescent drop on the left is in better focus than that on the right. The arrow in Figure 26 points to particular beads which are better imaged when the hologram is reconstructed at depth z_0 than in Figure 27 at depth z_1. Similarly, the arrow in Figure 27 points out a string of four beads which can be individually distinguished when the hologram is

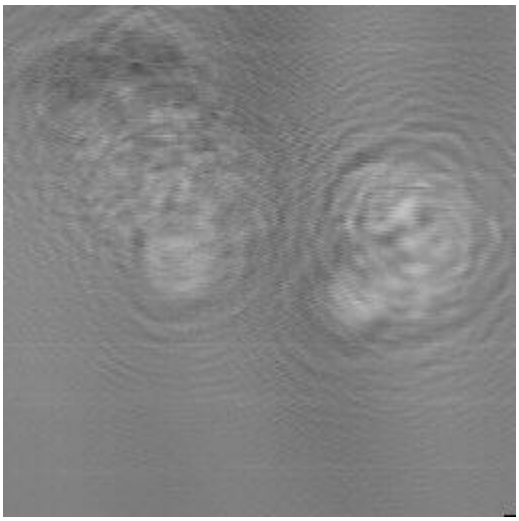

Figure 25 - Hologram of fluorescent specimen recorded using OSH. The object consists of two drops of solution containing a high concentration of fluorescent latex beads separated in depth by about 2 mm. The image is a 256 level gray scale image consisting of 256x256 pixels. The area scanned is about 2.0 mm x 2.0 mm.

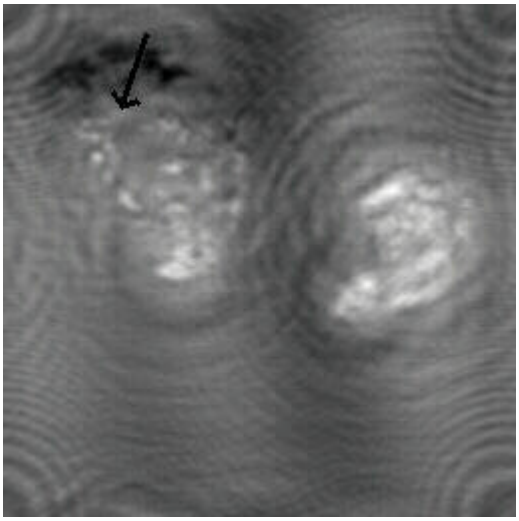

Figure 26 - Reconstruction of the hologram shown in Figure 2 at a depth of $z_0 = 34.5$ mm. Arrow shows individual fluorescent beads which are in focus at this depth.

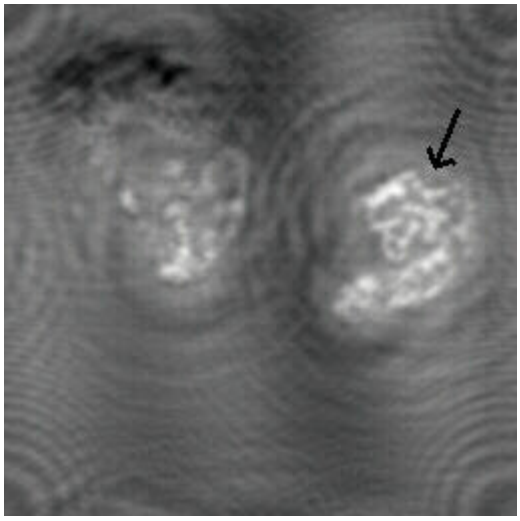

Figure 27 - Reconstruction of the hologram shown in Figure 2 at a depth of $z_1 = 36.8$ mm. The arrow shows four individual fluorescent beads which are in focus at this depth.

reconstructed at depth z_1, but which are blurred in the image reconstruction plane z_0 in Figure 26. No attempt was made to eliminate the twin image in these reconstructions, which explains the residual "fringing" observable in these images.

One reason the differences between Figures 26 and 27 are not more striking lies in the limited resolving power of the optics used in our experiment. The diffraction limited resolution limits for our system are investigated in detail in Chapter 7, but are addressed briefly here to prove a point. The resolution of the OSH system is limited by the system's numerical aperture (NA), which in turn depends on the focal length of lens L_s ($f = 150$ mm), and the diameter of the plane wave focused by lens L_s ($D = 10mm$). Resolution limits can be estimated by those of optical microscopy, according to the following equations:[71] *lateral resolution* $= \Delta x = \frac{\lambda}{2NA}$ and *longitudinal resolution* $= \Delta z = \frac{\lambda}{NA^2}$, where λ is the wavelength of the laser. The NA of our system is approximately 0.033 which corresponds to diffraction limited resolution limits of $\Delta x = 7.8\,\mu m$ and $\Delta z = 473$ μm. The 15 μm bead size is very close to the limit that we can expect to resolve laterally with our current setup, and more than an order of magnitude beyond what we can resolve in the z dimension. At this "proof of principle" stage, our optics have not been optimized for resolution.

7.0 Analysis

Several advantages holographic fluorescence microscopy by OSH has over standard 3D microscopes have been pointed out here, and in the literature. Most of these stem from the fact that 3D imaging by OSH requires only a single 2D scan to acquire 3D information. This leads to a reduction in 3D image acquisition time, a less critical positioning requirement, and a potential reduction in photobleaching. To quantify these claims, a detailed analysis is presented. The approach is to compare the new technique based on OSH with the industry standard for 3D imaging microscopy, the confocal scanning optical (or laser) microscope. Areas of primary concern are image acquisition time, resolution limits, and photobleaching. In this chapter, some preliminaries are addressed before considering in detail the resolution limits of OSH and the amount of photo-damage inflicted by the technique. Since both CSOM and OSH are far field optical approaches, the limits of resolution are based on the diffraction limit of light. It is important to understand how different resolution criteria are derived and related in order to fairly compare the two systems. With this in mind, resolution criteria based on a Gaussian beam approach is compared to diffraction by a circular aperture. Where photobleaching is concerned, the fundamental differences between the two systems are addressed. Since the illumination is tightly focused on the specimen in the confocal case, CSOM inflicts a significantly higher peak irradiance on the specimen. However, with the broader scan pattern used in OSH, the object receives more total radiant energy in a single scan in the holographic case than CSOM.

7.1 Preliminary Calculations

Before jumping into the detailed and rather complicated comparison of the two systems, a number of parameters and relationships must be defined. First, a review of Gaussian beam parameters is presented. There are a number of important relationships concerning the number of fringes in the FZP, scanning distance, spatial sampling rate, resolution, etc. which must be thoroughly understood before a discriminating analysis can be performed. For instance, the resolution limit for OSH deteriorates as the distance z increases. One obvious solution to this problem is to decrease z to zero to maximize resolution. Unfortunately, z cannot be decreased to zero. As z gets smaller, the overall size of the FZP scanning field decreases with respect to the object and recorded fringe information is lost. Since in OSH the 3D object information is stored in the fringes of the hologram, image quality is dependent on the number of fringes that contribute to recording. The number of fringes that contribute information to the hologram is defined by the relationship between the fringe spacing and sampling step size. Some of these relations have been referred to qualitatively in the literature. The goal here is a detailed and precise quantitative treatment of these relationships.

7.1.1 Rayleigh Range, Gaussian Beam Waist and Numerical Aperture

To achieve maximum resolution in OSH, it is desirable to scan the object just beyond the focus of the spherical wave, or in other words to minimize z. Care must be taken, however, because the theory behind the recording scheme, the basis for numerical image reconstruction, and the following analysis are all based on Fraunhofer diffraction theory. The assumption is that the object is in the far field, or Fraunhofer regime, when scanning by the FZP occurs. A parameter associated with Gaussian beams called the Rayleigh range is used as a discriminating factor between the near field and the far field

case. The Rayleigh range, as well as the Gaussian beam waist and numerical aperture, is defined here.

In one leg of the interferometer there is a plane wave incident on the lens, L_s. Under a Gaussian analysis this situation is modeled by a broad Gaussian with waist w_{p0} (the subscript p is for plane wave) that is incident on a lens at its waist, as shown in Figure 28. It is assumed that the radius of the lens is large compared to w_{p0}, allowing truncation of the Gaussian wave by the lens to be neglected. The Rayleigh range, designated as z_0, is defined as the distance from the waist in which the beam spot size increases by $\sqrt{2}$. The far field, where Fraunhofer diffraction is said to occur, is defined as being much greater than the Rayleigh range. The analysis to follow, therefore, is valid at distances $z \gg z_0$. The Rayleigh range is defined as[68]

$$z_{s0} = \frac{n\pi w_{s0}^2}{\lambda}, \tag{24}$$

where w_{s0} is the waist of the focused wave, and n is the index of refraction. Imaging in air is assumed in all cases for OSH, so $n = 1$. Note that the plane wave incident on the lens has a Rayleigh range associated with it as well, $z_{p0} = \frac{n\pi w_{p0}^2}{\lambda}$. If a plane wave is incident on a lens with focal length f, as in Figure 28, the beam is focused to a minimum, but finite spot size at the focus of the lens. The waist of the resulting focused beam is given by

$$w_{s0} = \frac{w_{p0} f}{z_{p0}\sqrt{1+(f/z_{p0})^2}}. \tag{25}$$

If $z_{p0} \gg f$, equation (25) reduces to

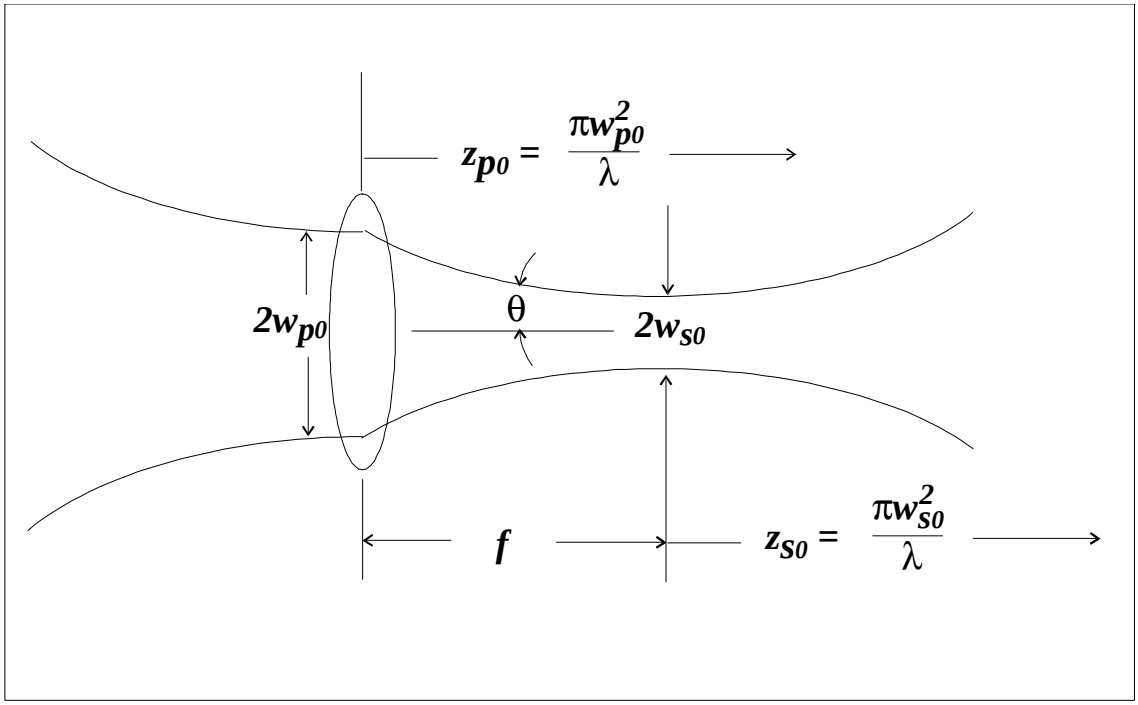

Figure 28 - Focusing of a Gaussian beam with beam waist and numerical aperture shown

$$w_{s0} = \frac{\lambda f}{\pi w_{p0}}, \tag{26}$$

and the waist occurs at the focus of the lens. For OSH, λ is on the order of $10^{-6}m$ and w_{p0} is on the order of $10^{-2}\ m$, giving z_{p0} a value on the order of $300m$. It is safe to make the assumption that $f \ll 300m$, particularly for microscopy. Since the assumption that $z_{p0} \gg f$ is justified, equation (26) will be used for w_{s0}.

The numerical aperture is defined as $NA = nsin\theta$, where θ is the half angle of the cone of illumination.[69] The angle θ is also shown in Figure 28. For a Gaussian beam and for small angles, $NA = \frac{w_{p0}}{f}$. Making use of this definition, the beam waist of the spherical wave, w_{s0}, and the Rayleigh range, z_{s0}, can be written in terms of the NA as

$$w_{s0} = \frac{\lambda}{\pi NA}, \tag{27}$$

and

$$z_{s0} = \frac{n\lambda}{\pi NA^2}. \tag{28}$$

These expressions for the focused beam waist, Rayleigh range, and NA will be used extensively in the sections to follow.

7.1.2 Relationship Between Number of Zones in the FZP and z

The number of zones in the FZP is dependent on the NA of the focusing lens, but also changes with distance. The relationship between the NA of lens L_s, the distance z, and the number of zones in the FZP is derived in this section. This relationship is important since the number of zones in the FZP effects the quality of the hologram and subsequent image reconstruction.[23] To investigate the situation in detail, consider the

FZP as the sine term multiplied by a Gaussian function. The equation describing the intensity distribution of this FZP is given by equation (10), repeated here for convenience,

$$I(x,\, y,\, z) = exp\Big[- \tfrac{2(x^2+y^2)}{w_{fzp}^2} \Big] sin\big[\tfrac{\pi}{\lambda z}(x^2 + y^2) \big], \tag{10}$$

where the constant term has been neglected. The FZP is created by superimposing a plane wave and a spherical wave, which can be considered broad and narrow Gaussian beams with widths w_p and w_s, respectively. If the broad Gaussian beam, associated with the plane wave, is diverging very little, the width is nearly constant with z and equal to the value at the waist, w_{p0}. Throughout the remainder of this analysis, w_{p0} and w_p will be used interchangeably. If we assume that the FZP only exists when both the plane wave and spherical wave have intensity greater than $1/e^2$ of their maximum, the area beyond the focus of lens L_s can be separated into two distinct regions. Figure 29 is a depiction of the superposition of the plane wave and spherical wave. The shaded area designates where the FZP exists beyond the waist of the spherical beam. As the spherical wave diverges from its waist at the focus of lens L_s, its width is initially less than that of the plane wave. Assuming that the original beam profiles have equal diameters, when $z = f$ (the focal length of lens L_s) the widths of the plane wave and spherical wave are equal. At distances $z > f$, the spherical wave has a larger diameter than the plane wave. Region 1 is defined in the figure as the region where $w_s < w_p$, and Region 2 is where $w_s > w_p$. The important thing to realize is that in Region 1 $w_{fzp} = w_s$, but in Region 2 $w_{fzp} = w_p$.

In Region 1, $w_s < w_p$ and the number of zones in the FZP depends on the numerical aperture (NA) of the focusing lens. As shown by simulation in Chapter 3, the number of fringes in the FZP, given by equation (11), is determined by the relationship between the $1/e^2$ points of the Gaussian multiplier and the sine term. Using cylindrical

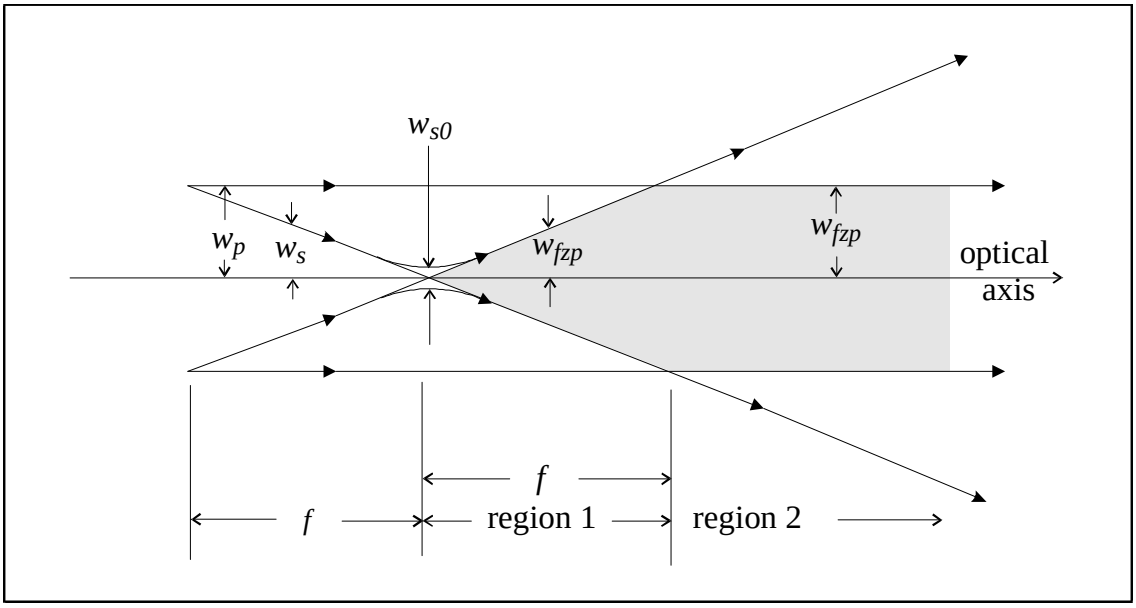

Figure 29 - Dependence of ω_{fzp} on z

coordinates, the relationship between the lateral distance from the origin and the number of zones or fringes in the FZP is given by

$$N_z = \frac{1}{2\lambda z}\rho^2, \tag{29}$$

where N_z is the number of zones and $\rho^2 = x^2 + y^2$. The $1/e^2$ points of the spherical wave will occur at $\rho^2 = w_{fzp}^2$. Combining these equations, we see that the number of fringes in the pattern inside the $1/e^2$ beam width of the spherical wave is given by

$$N_z = \frac{1}{2\lambda z}w_{fzp}^2. \tag{30}$$

The width of the spherical wave at distance z is dependent on the NA of the lens. For $z \gg z_{s0}$, $w_{fzp}/z = w_p/f$, so

$$w_{fzp} = \frac{zw_p}{f} = z(NA) \qquad z \gg z_{s0}. \tag{31}$$

Making use of equation (31), the number of zones in the FZP for Region 1 can be rewritten in terms of the NA of the focusing optics as

$$N_z(\text{Region 1}) = \frac{1}{2\lambda z}\left(\frac{z\omega_p}{f}\right)^2 = \frac{z}{2\lambda}\left(\frac{\omega_p}{f}\right)^2 = \frac{z}{2\lambda}(NA)^2. \tag{32}$$

As equation (32) shows, the number of zones in the FZP is dependent not only on $(NA)^2$, but is proportional to the distance from the focus of the lens. Figure 30 shows a plot of equation (32), illustrating the relationship between the number of zones in the FZP and z for several different values of NA. Since the number of zones in the FZP has an effect on the recording capability of the OSH system, and subsequent image reconstruction, it is

intuitively obvious that there must be a lower limit on N_z. A minimum fringe requirement should be based on the quality of the image reconstruction. It was demonstrated by simulation, for instance, that a FZP having ten zones within the $1/e^2$ points has acceptable image quality upon reconstruction. For a given NA, wavelength, and number of zones, there also corresponds a minimum scanning distance based on equation (32) and Figure 30. The importance of this minimum scanning distance will become clear when resolution limits are discussed in Section 7.2. Equation (32) is rewritten to give an explicit expression for this value:

$$z_{min} = \frac{2\lambda N_z}{(NA)^2}. \tag{33}$$

Keeping in mind that the analysis is valid for $z \gg z_{s0}$, equation (33) is compared to the expression for the Rayleigh range (equation 28). The minimum scanning distance can be written in terms of the Rayleigh range,

$$z_{min} = \frac{\pi N_z}{2} z_{s0,} \tag{34}$$

showing that for $N_z \geq 7$, z_{min} is more than 10 times the Rayleigh range.

For the current experimental configuration $NA = 0.033$, so the minimum z for ten fringe holography is $9.5mm$. A second interesting value associated with the current setup can be extracted from the preceding analysis. Using a typical value for z of $35mm$, equation (32) shows that there are approximately 37 zones contained within the $1/e^2$ points of the FZP used to create the hologram shown in Chapter 6.

A similar analysis is conducted for the second region, in which $w_s > w_p$. In Region 2, w_{fzp} is no longer dependent on the NA of the focusing lens, but only on the

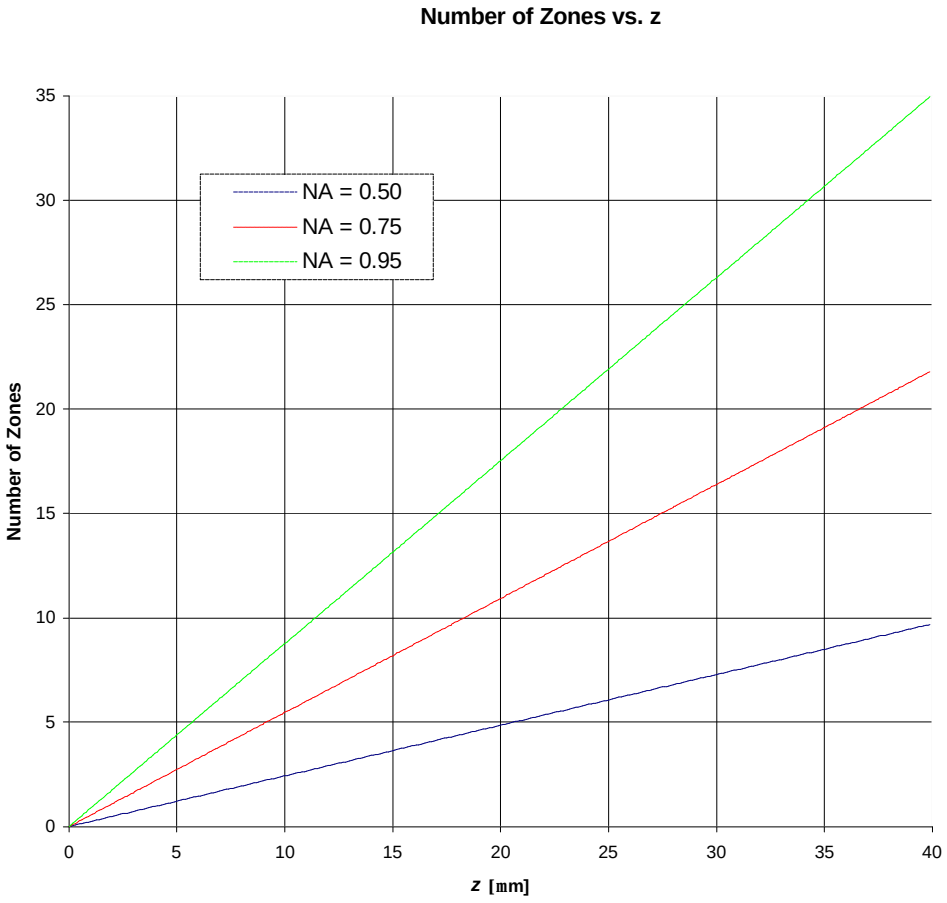

Figure 30 - Plot of N_z vs. z for $NA = 0.5,\ 0.75$ and 0.95. ($\lambda = 515\,nm$)

original beam width of the plane wave used to create the FZP, or $w_{fzp} = w_p$ (see Figure 29). For Region 2, equation (30) can be written

$$N_z(\text{Region}\,2) = \tfrac{1}{2\lambda z} w_p^2. \tag{35}$$

The number of fringes in this region is inversely proportional to z. Since w_{fzp} is independent of the NA of the focusing optics, this NA is no longer relevant. When $z > f$, an effective NA can be defined, $NA_e = \frac{w_p}{z}$. Since w_p is nearly constant, the effective NA gets smaller with increasing z. It is now obvious that the resolving capability of the system will deteriorate in Region 2 with increasing distance. This fact is critical for remote sensing applications and large scale holography, as large diameter plane waves must be generated to improve NA_e in Region 2 (one of the deterrents to standard holography of very large objects).

By adhering to the assumption that there is a lower limit to the number of zones in the scanning pattern for holography by OSH, equation (35) can be used to derive a maximum bound for z under this condition. Having minimum and maximum z values equates to a depth of field criteria based on a required minimum number of zones in the FZP. Using equation (35) the maximum value for z in terms of N_z and w_p is given by

$$z_{max} = \tfrac{1}{2\lambda N_z} w_p^2. \tag{36}$$

Equation (36) is plotted in Figures 31 and 32, illustrating the relationship between w_p and z_{max} for $N_z = 5$, 10, and 20. Figure 31 shows maximum z values for small w_p, up to about $1\,cm$ which corresponds to almost 1 inch diameter optics. For the current system, using $N_z = 10$ and $\omega_p = 5mm$ gives $z_{max} = 2.43\ m$. For longer range holography, applicable to remote sensing, Figure 32 shows the same relationship for w_p up to $20\,cm$.

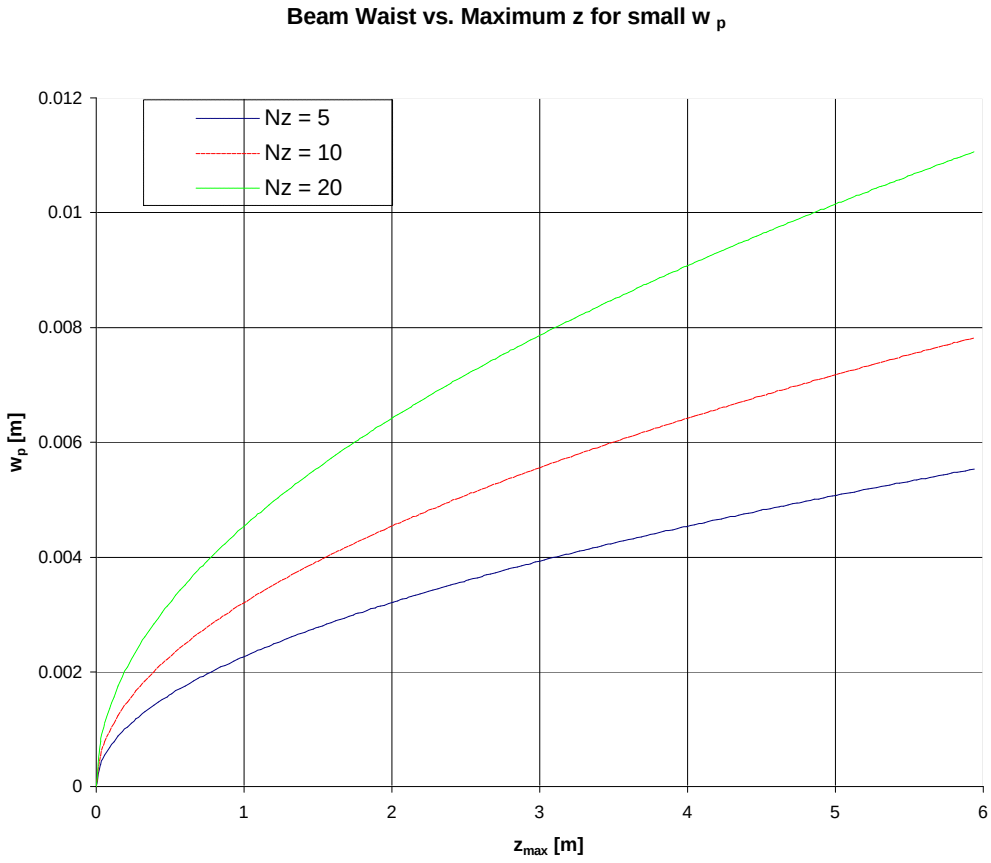

Figure 31 - Plot showing maximum w_p vs. z, for small w_p and $N_z = 5,\ 10,$ and 20.

($\lambda = 515\,nm$)

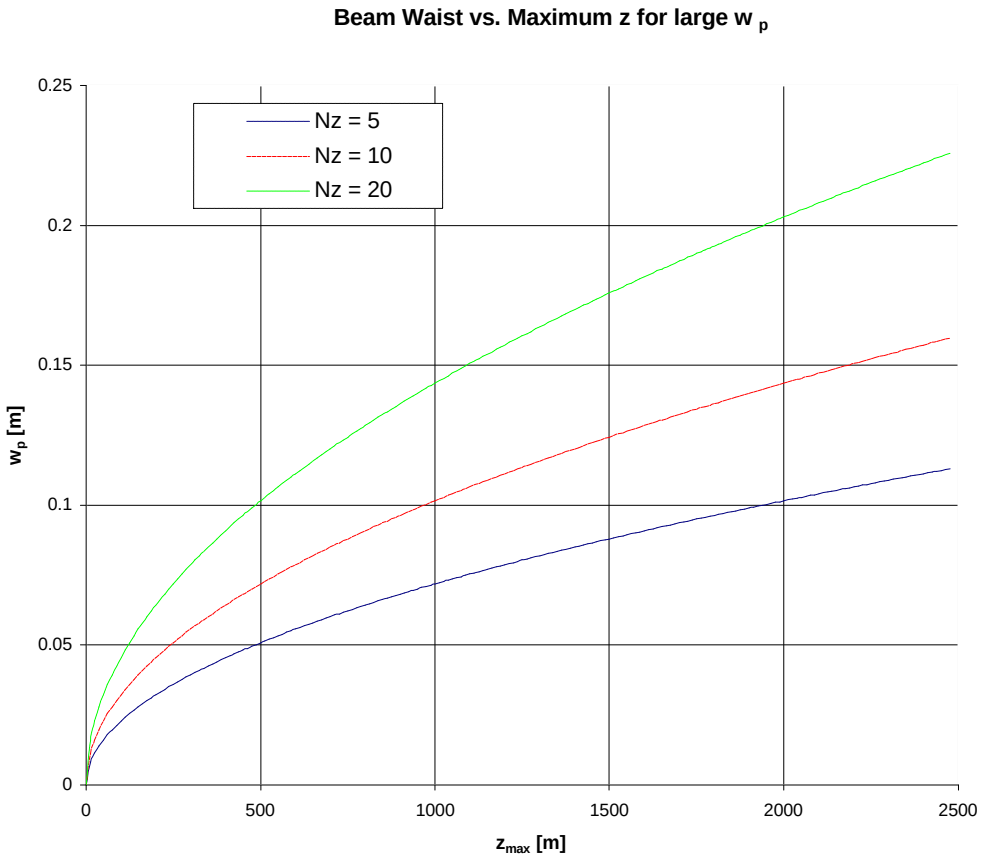

Figure 32 - Plot showing w_p vs. maximum z for large w_p and for $N_z = 5,\ 10,$ and 20.

$(\lambda = 515\, nm)$

The figure implies that 10 zone holography is possible at ranges of $2.5\,km$ if a beam radius of $15\,cm$ can be achieved. A plane wave beam radius of $15\,cm$ corresponds to about 12 inch diameter optics. This is probably close to the practical limit from a systems point of view, based on cost. Twelve inch optics of reasonable quality are not cheap. Mirrors or diffractive (Fresnel) lenses, may be an alternative to standard lenses for long-range applications.

A few aspects of the system have been quantified in this section. Emphasis has been placed on bounding the scanning distance z based on a minimum requirement of FZP zones that contribute to image reconstruction. Understanding the lower limit on scanning distance, given by z_{min}, has particular relevance in the resolution limit analysis that follows. Two distinct regions have been identified based on practical considerations involved in generating the FZP. It is reasonable to assume that when OSH is applied to microscopy, imaging will take place in Region 1. For applications such as remote sensing and large scale holography, the equations for Region 2 will apply.

7.1.3 Fringe Spacing and Sampling

Yet another practical consideration involves the number of zones in the FZP and the scanning distance. The required spatial sampling rate (samples/meter) is dependent on fringe spacing, and therefore dependent on both N_z and z. The relationship between fringe spacing, the lateral distance between adjacent intensity peaks in the FZP, and the sampling rate is derived in this section. To quantify this aspect of the system, consider again the scanning pattern (for this analysis the Gaussian multiplier is irrelevant):

$$I(\rho,\, z) = sin\left[\tfrac{\pi}{\lambda z}\rho^2\right]. \tag{37}$$

Again, fringes occur when the argument of equation (37) equals $2\pi N_z$, or when $\rho = \sqrt{2\lambda z N_z}$. The radial extent of a particular zone of interest (say the predetermined minimum required fringe) is given by

$$\Delta\rho_z = \sqrt{2\lambda z N_z} - \sqrt{2\lambda z (N_z - 1)}. \tag{38}$$

As discussed in Chapter 3, for OSH the Nyquist criterion must be satisfied for the scanning field as well as the object being scanned. By the Nyquist criterion, the sampling step size, Δx_s, must be less than or equal to $\frac{\Delta\rho_z}{2}$, or

$$\Delta x_s \leq \frac{1}{2}\left\{\sqrt{2\lambda z N_z} - \sqrt{2\lambda z (N_z - 1)}\right\} = \frac{\sqrt{2\lambda z}}{2}\left\{\sqrt{N_z} - \sqrt{(N_z - 1)}\right\}. \tag{39}$$

From equation (39), the maximum sampling step size can be determined for a given number of fringes in the FZP and z. This relationship is plotted in Figure 33 for $N_z = 5$, 10, and 20. To assure that the tenth FZP zone contributes to image reconstruction in the current configuration, the step size of the scanning platform must be less than 16 μm, (using $z = 35mm$). Equation (39) gives only one of the two criteria which must be met for OSH sampling rate. Since the Sampling theorem must hold for both the scanning field and the object itself, these requirements are compared and the more stringent of the two must be met.

7.1.4 Scanning Limits

The total scan area must be used to calculate irradiance levels for the photobleaching analysis. From the previous section we know that the sampling step size is determined by the desired resolution and the minimum zone count requirement. For a

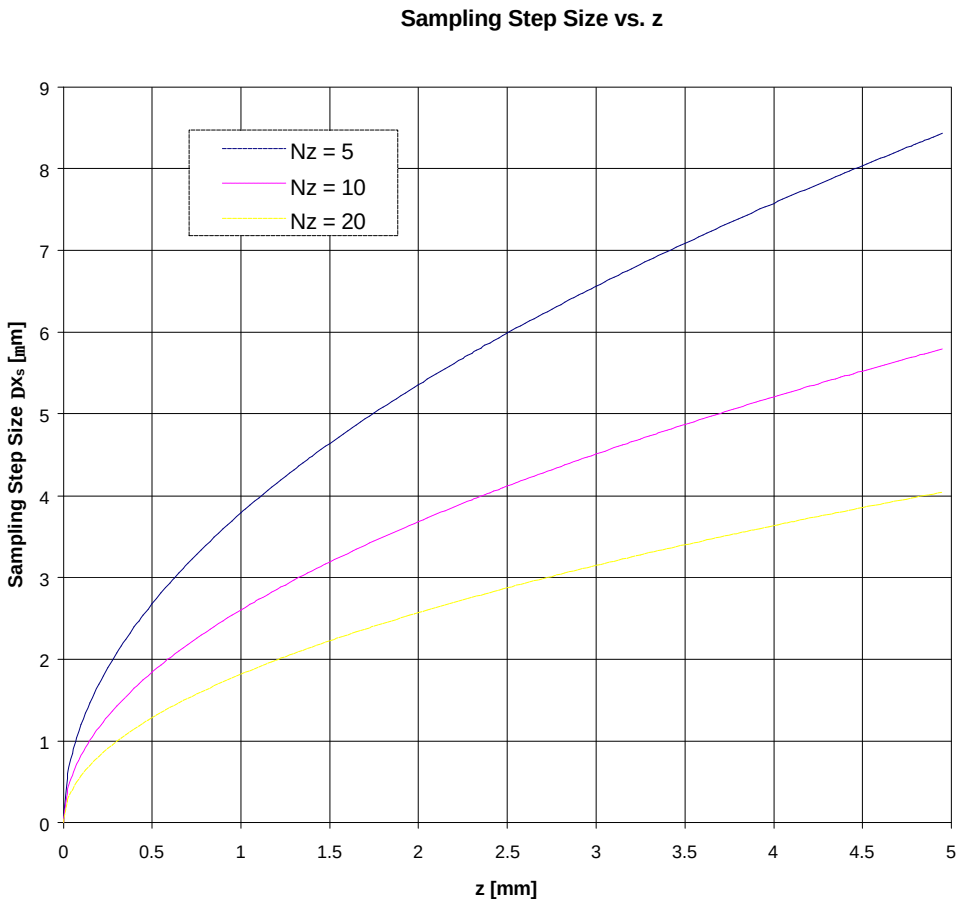

Figure 33 - Maximum sampling step size versus z for $N_z = 5,\ 10$ and 20. ($\lambda = 515\,nm$)

given sampling step size, the width and height of the scan area is determined by the number of pixels in the image. In this experiment 256×256 pixel images are used so the number of pixels in the x and y directions are equal, or $N_{px} = N_{py} = 256$. The width of the object in the x direction is referred to as the x-extent, and the height of the object is referred to as the y-extent. These values are given by

$$\left.\begin{aligned} x_{ext} &= N_{px} \times \Delta x_s \\ y_{ext} &= N_{py} \times \Delta x_s \end{aligned}\right\}. \tag{40}$$

For spot scanning systems, such as CSOM, equation (40) defines the scanned area for all intents and purposes. The width and height of the object, however, are not the end of the story when determining the scan limits for OSH. Again, the omnipresent factor N_z, the required number of zones, comes into play. To see how, consider Figure 34. The requirement is to ensure that a particular number of zones contribute to the image reconstruction of each point in the object. To achieve this, the object, in its entirety, must be scanned through the pattern to just beyond this zone. The situation for beam scanning is shown in Figure 34 a), while the situation for object scanning is illustrated in Figure 34 b). For object scanning, the platform must move the lateral distance: $x_{ext} + 2w_{fzp}$. One important reason that it is necessary to investigate the scan area in detail is to determine the total irradiance received by the specimen during an image acquisition. Consider a point in the center of the object area. During an image acquisition, this point will be irradiated by all the power in the scanning field out to a radius of

$$\rho_{tot} = \left(\tfrac{x_{ext}}{2} + w_{fzp}\right). \tag{41}$$

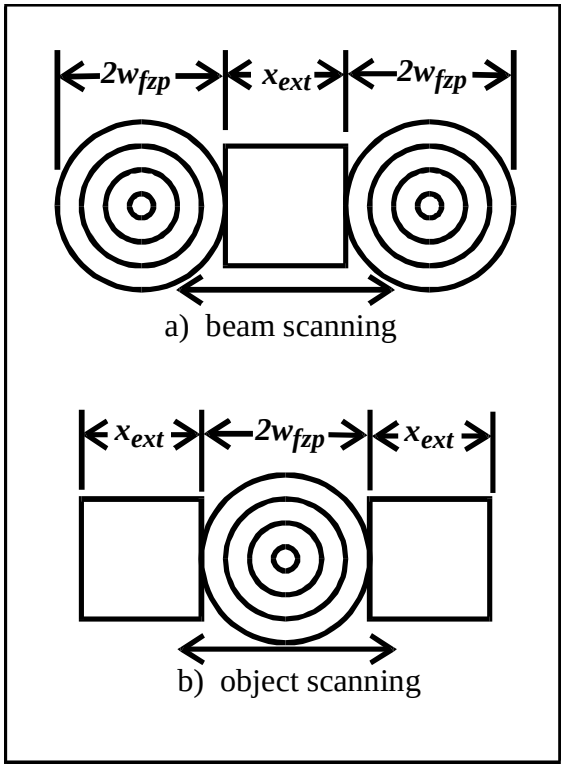

Figure 34 - Diagram showing the scanning limits in the lateral dimension for a) beam scanning and b) object scanning

In the following analysis, this radius will be used as a limit of integration to determine the total power in the scanning beam, and hence define the total energy received by the specimen.

7.1.5 FWHM, $1/e$ and $1/e^2$ Widths of a Gaussian Beam

Because most optics, such as lenses, have a circular cross section, resolution limits for optical systems are generally derived based on how light is diffracted by a circular aperture. Uniform illumination diffracted by a circular aperture results in an Airy pattern. The resolution limits for OSH, however, have been derived based on a Gaussian beam analysis. Nontruncated Gaussian beams stay Gaussian in shape as they diffract. In order to compare resolution limits derived under these different analyses, circular aperture versus Gaussian beam, it is necessary to explicitly specify the relationship between results obtained by each method. To make matters worse, different resolution limit criteria exist based on "how resolved" is resolved (see Section 7.2). These different criteria are based on the diffraction patterns of adjacent points overlapping at different percentages of the maximum intensity of the focused spots. Typical percentages are half the maximum, $1/e$ of the maximum, and $1/e^2$ of the maximum. If half the maximum width, the width is usually referred to as the full-width at half maximum (FWHM) width. Consider the equation for the intensity pattern produced by a Gaussian beam:[69]

$$I_{\text{Gauss}}(\rho,\, z) = I_0 exp\Big[- \tfrac{2(\rho^2)}{w^2} \Big]. \tag{42}$$

For a nontruncated Gaussian beam, (i.e. lens diameter $> 2w),$ the waist radius is given by equation (27), $w = w_{s0} = \frac{\lambda}{\pi NA}$. Substituting into equation (42) yields

$$I_{\text{Gauss}}(\rho,\, z) = I_0 exp\Big[- \tfrac{2(\pi NA\rho)^2}{\lambda^2} \Big]. \tag{43}$$

The equation for the Airy pattern, the diffraction pattern at the focus of a uniformly illuminated circular lens, is given by[70]

$$I_{\text{Airy}}(\rho) = I_0 \Big\{ \tfrac{2J_1[2\pi(NA)\rho/\lambda]}{2\pi(NA)\rho/\lambda} \Big\}^2, \tag{44}$$

where J_1 is a Bessel function of the first kind and first order. The Gaussian profile given by equation (43) is plotted in Figure 35 for $NA = 0.95$, along with the Airy pattern at the focus of a lens with the same NA .

As the plot shows, the FWHM of a focused Gaussian beam is smaller than the FWHM of the focus spot produced by a uniformly illuminated lens with the same NA. By definition the Gaussian parameter, w, defines the beam width, or beam radius, of the Gaussian beam at the $1/e^2$ points. It is easy to determine the FWHM width for the Gaussian case as well. The radial distance at which the Gaussian beam is at half its maximum is defined by the following equation:

$$exp\Big[- \tfrac{2(\pi NA\rho_{1/2})^2}{\lambda^2} \Big] = 1/2. \tag{45}$$

Solving for $\rho_{1/2}$, we have

$$\rho_{1/2} = \sqrt{\tfrac{-ln(.5)}{2\pi^2}} \tfrac{\lambda}{NA} = .187 \tfrac{\lambda}{NA} \tag{46}$$

The distance given in equation (46) defines the Gaussian half-width at half maximum point. The FWHM width is twice $\rho_{1/2}$, or

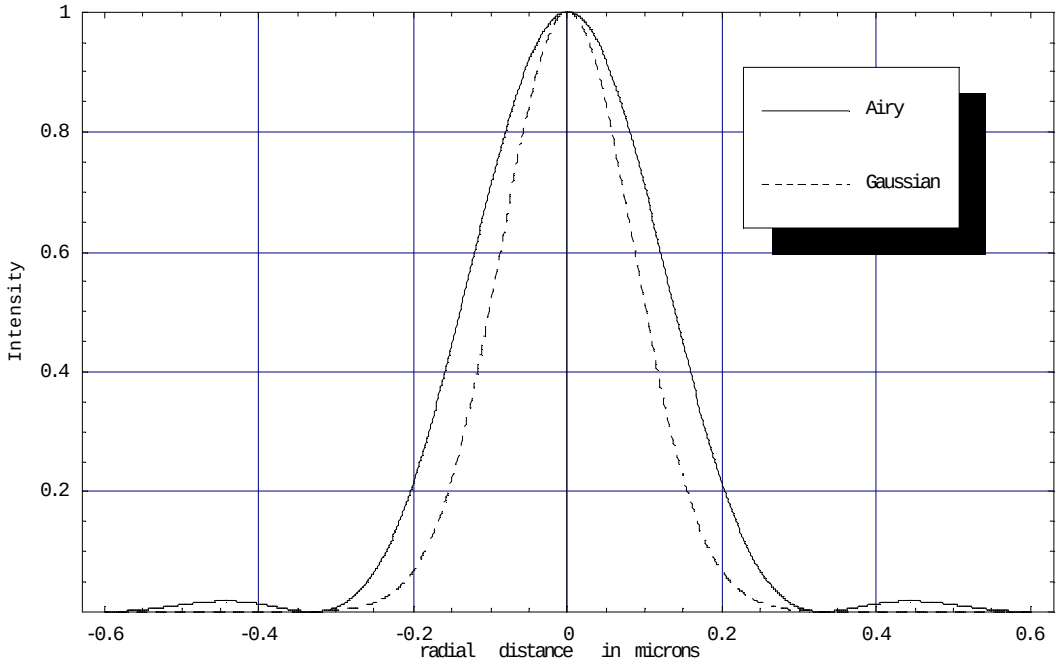

Figure 35 - Plot of Gaussian and Airy pattern at the focus of a lens with $NA = 0.95$ ($\lambda = 515\,nm$)

Gaussian: $\Delta\rho$(FWHM) $= 0.375\frac{\lambda}{NA}$, (47)

where the symbol $\Delta\rho$ indicates a lateral resolution criterion. As a comparison, the FWHM of the Airy pattern is given by[73]

Airy: $\Delta\rho$(FWHM) $= 0.51\frac{\lambda}{NA}$.

Widths for the $1/e^2$ and $1/e$ points can be derived as easily for the focused Gaussian beam:

Gaussian: $\Delta\rho(1/e^2) = \frac{2}{\pi}\frac{\lambda}{NA}$, (48)

and

Gaussian: $\Delta\rho(1/e) = \frac{\sqrt{2}}{\pi}\frac{\lambda}{NA}$. (49)

These relationships are helpful for calculating the factors necessary to make valid comparisons between resolution criteria derived by different approaches. For instance, comparing a Gaussian-based $1/e$ lateral resolution limit to a Gaussian FWHM resolution criterion can be achieved within a reasonable error by simply multiplying by 0.833. That is Gaussian: $0.833[\Delta\rho(1/e)] \Rightarrow \Delta\rho$(FWHM). Other conversions are given in Table 2. Table 2 will prove indispensable in the next section for equalizing the resolution limits of optical microscopy, CSOM and OSH.

Table 2 - Conversion factors for comparing resolution criteria

Multiply by	To convert: $\Rightarrow$	To:
0.833	Gaussian $\Delta\rho(1/e)$	Gaussian $\Delta\rho(\text{FWHM})$
0.589	Gaussian $\Delta\rho(1/e^2)$	Gaussian $\Delta\rho(\text{FWHM})$
1.36	Gaussian $\Delta\rho(\text{FWHM})$	Airy $\Delta\rho(\text{FWHM})$
1.133	Gaussian $\Delta\rho(1/e)$	Airy $\Delta\rho(\text{FWHM})$

7.2 Resolution Limits

The resolution of a standard optical system, such as a microscope or telescope is limited by diffraction effects which result from the finite size of the light collecting aperture.[69] Because of diffraction, an infinitely small point source cannot be imaged exactly, but instead appears as a bright central spot of finite extent surrounded by rings of rapidly decreasing intensity. The central lobe of this pattern is referred to as the Airy disk. Diffraction has a similar effect on nonstandard optical systems, such as a confocal microscope or OSH imaging system. Due to the finite size of the illuminating optics, light cannot be focused to an infinitely small point. The resolution limits of these systems are determined by the size and design of the optics used for illumination. Two point source objects which are close together may have diffraction patterns which overlap in the image. If the Airy disks of the two patterns blend together, they may appear to be due to a single source. The resolving power of an imaging system is a measure of its ability to separate images of two neighboring object points. According to the Rayleigh criterion, two equally bright point images are regarded as just resolved when the principal maximum of one coincides with the first minimum of the other.[71] When two points are separated according to the Rayleigh criterion, the combined intensity at the midpoint is 73.5% of the maximum intensity at either point. Another way to say this is that the intensity patterns cross at the

$1/e$ points, or at the point where each individual source has dropped to $1/e$, or 36.78% of its maximum value. For an imaging system, the limit of resolution is the distance Δx or angle $\Delta\theta$ between two points separated by the Rayleigh range. The resolving power is defined as the reciprocal of this quantity.

Other types of resolution criteria exist and are important. Of particular importance is the "single-point resolution" defined as the width of the image of a point object between the half power points of the main lobe. This parameter, FWHM, was considered for a Gaussian beam in Section 7.1.5. The concept is particularly relevant to confocal microscopy since depth resolution is often measured using a single point method. A two-point resolution criterion called the Sparrow criterion is equivalent to the FWHM method. The Sparrow criterion states that two adjacent, equally bright points are just distinguishable if the intensity of the midway point is equal to the intensity of the imaged points.[73] If the intensity of the combined signal at the midway point adds to the maximum value of each point, each contribution is half its maximum value, hence the equivalence of the two methods.

7.2.1 Resolution Limits for Optical Microscopy

For an optical microscope using incoherent illumination, the lateral limit of resolution under the Rayleigh criterion, or the diffraction limit, is given by[71]

$$\Delta x_{opt}(\text{Rayleigh}) = 0.61\frac{\lambda}{NA}, \tag{50}$$

where NA is the numerical aperture of the microscope objective. The numerical aperture is defined as in the Gaussian case as $NA = nsin\theta$ where θ is the half angle of the cone of illumination.[69] For the Sparrow criterion, the lateral resolution is given by[73]

$$\Delta x_{opt}(\text{Sparrow}) = 0.51\frac{\lambda}{NA}. \quad (51)$$

The axial resolution is more complicated to measure and is usually only given as a single point resolution limit. For optical microscopy, the depth resolution is given by Stelzer as[72]

$$\Delta z_{opt} = n\frac{\lambda}{NA^2}. \quad (52)$$

Interestingly, Stelzer gives a separate axial resolution for standard fluorescence microscopy:

$$\Delta z_{fl} = 1.5\ n\frac{\lambda}{NA^2}. \quad (53)$$

The axial resolution for a reflecting object is about 30% better than that of a fluorescent object. The factor in equation (53) of 1.5 is dependent on the ratio of excitation to emission wavelength and will increase with increasing Stokes shift.[72]

When imaging takes place in the air, the practical limit for NA is about 0.95.[40] For illumination at 515 nm, an NA of 0.95 corresponds to theoretical limits of resolution $\Delta x_{opt} = 0.28\ \mu m$ and $\Delta z_{opt} = 0.57\ \mu m$ under the Sparrow resolution criterion.

7.2.2 Resolution Limits for Confocal Scanning Optical Microscopy

Even though the CSOM has better edge response, and therefore better contrast characteristics, the lateral resolution is not significantly better than standard optical microscopy. The lateral resolution limit under the Rayleigh criterion is[73]

$$\Delta x_{cf} = 0.51\frac{\lambda}{NA}. \quad (54)$$

Under the Sparrow criterion, the lateral resolution limit for the standard microscope and confocal microscope are the same. Not everyone agrees with this sentiment. Cogswell and Sheppard claim confocal techniques can provide as much as 1.4 times the lateral resolution of a conventional microscope.[74] This potential increase in lateral resolution limit is because the object is effectively imaged using both the incident and collected light. Since the resolution is dependent on pinhole size, it is more likely that this improvement will manifest itself in confocal brightfield imaging as opposed to confocal fluorescent systems, where pinhole size is often increased due to low fluorescent signal levels. The longitudinal resolution is not usually considered in the two-point sense. As reported in the literature, the range resolution is observed by scanning a highly reflective surface, such as a mirror, axially through the focal plane. The range resolution is then defined as the approximate distance between points where the signal drops to half its maximum intensity. This distance is generally given as[73]

$$\Delta z_{cf} = 0.45 \frac{\lambda}{n(1-cos\theta)}. \tag{55}$$

In the paraxial approximation with $n = 1$, equation (55) reduces to[73]

$$\Delta z_{cf} \approx 0.89 \frac{\lambda n}{NA^2}. \tag{56}$$

For illumination at 515 nm, an NA of 0.95 corresponds to theoretical limits of resolution $\Delta x_{cf} = 0.28\ \mu m$ and $\Delta z_{cf} = 0.51\ \mu m$ under the Sparrow resolution criterion.

7.2.3 Resolution Limits for OSH

It has always been assumed that resolution limits of microscopy by OSH will roughly follow those of optical microscopy as defined in Section 7.2.1. Some insight can be gained, however, by considering the z dependence and effect of fringe spacing on the theoretical resolution limit for OSH. This z dependence was first pointed out by Duncan and Poon who derived the resolution limits for the system based on a Gaussian beam analysis.[18] Of course, for any optical system Δx (the lateral resolution limit) and Δz (the longitudinal resolution limit) are dependent on z. This fact can easily be overlooked since formulas for resolution limits of common optical systems only contain a dependence on the numerical aperture, NA. The universal z dependence of resolution limit can be driven home with a few examples. First consider a telescopic sight, such as a rifle scope. Now the z dependence of the lateral resolution limit, Δx, is obvious. A given scope might have a spatial resolution limit of one centimeter at 10 meters, meaning it is possible to distinguish two points separated by one centimeter that are 10 meters away. However, this centimeter resolution limit certainly will not hold as well for 10 kilometers, 100 kilometers and 1000 kilometers. For telescopes, resolution is usually specified in terms of resolving power, which is defined as an angular resolution limit, $\Delta\theta$, instead of a resolution limit given in terms of lateral distance, Δx. Angular resolution limits are, in fact, independent of z. In microscopy, the z dependence is more subtle. The assumption is made that the object is located at the focus of the objective lens system. If the object is in some plane other than the focus, blurred imaging will result and resolution will suffer. Therefore, in microscopy, z is fixed and the resolution limits are determined based on this fixed, but not independent, depth. The case is different for microscopy by OSH since the object is not at the focus of any lens when the hologram is recorded. As the distance between the object and the focus of the spherical wave used to create the FZP scanning field is increased, the lateral resolution will suffer.

For OSH, a detailed analysis of lateral and longitudinal resolution has been conducted based on a Gaussian beam analysis. Expressions for the lateral and longitudinal resolution limits were derived. These limits are based on the distances at which the reconstructed images of adjacent, infinitesimal point objects will overlap at the $1/e$ points.[18] The criterion is therefore similar to the Rayleigh criterion, with the only difference being that the intensity distribution is assumed to be Gaussian as opposed to the Airy pattern. The lateral resolution for OSH is given as

$$\Delta x_{osh} = \sqrt{2} w_{s0} \left(\epsilon + \frac{z^2}{f^2} \right)^{\frac{1}{2}}, \tag{57}$$

and the longitudinal resolution limit is given as

$$\Delta z_{osh} = \frac{\sqrt{2} w_{s0} \frac{\lambda_2}{\lambda_1} M \left(\epsilon + \frac{z^2}{f^2} \right)^{\frac{1}{2}}}{1 - w_{s0} \frac{\lambda_2}{\lambda_1} \frac{M}{\sqrt{2}} \left(\epsilon + \frac{z^2}{f^2} \right)^{\frac{1}{2}} \left(\frac{z}{\epsilon f^2 + z^2} \right)}. \tag{58}$$

In equations 57 and 58, w_{s0}, w_p, and ϵ are defined as

$$\epsilon = \frac{\lambda_1 f}{\pi w_{s0} w_p}, \tag{59}$$

$$w_{s0} = \frac{\lambda_1 f}{\pi w_l M_{cs}}, \tag{60}$$

and

$$w_p = M_{cp} w_l. \tag{61}$$

As previously, subscripts p and s are used to denote the plane wave and spherical wave paths of the interferometer. In equations (57)-(61), the variables are defined as follows:

λ_1 = wavelength of the laser used for recording
λ_2 = wavelength of the laser used for reconstruction
f = focal length of lens L_s which creates spherical wave for the FZP

w_l = beam width of the laser beam at laser
w_p = beam width of plane wave for FZP, equal to w_{p0} above
w_{s0} = waist of the spherical wave for FZP
M_{cp} = magnification of collimator in plane wave path for FZP
M_{cs} = magnification of collimator in spherical wave path for FZP
M = system magnification factor
z = the distance between the waist of the spherical wave and the object

The equations can be simplified for the fluorescence microscopy case as follows. For the classical OSH setup, from which equations (57)-(61) were derived, λ_1 is the wavelength used to record the hologram. For optical image reconstruction, a different wavelength can be used to introduce magnification into the system. This project involves only numerical reconstruction in which $\lambda_2 = \lambda_1$ is assumed so $\lambda_2/\lambda_1 = 1$. The fluorescence microscopy setup uses a single telescope to expand both legs of the interferometer, making $M_{cp} = M_{cs}$, which in turn leads to the equality of $M_{cp}w_l$ and $M_{cs}w_l$. The expressions can be further simplified by replacing $M_{cp}\omega_l$ and $M_{cs}\omega_l$ with w_p, as they are simply the beam radius of the expanded, collimated plane wave, w_p. Therefore, the waist of the focused Gaussian can be rewritten in terms of w_p as

$$\omega_{s0} = \frac{\lambda f}{\pi \omega_p}, \tag{62}$$

where the subscript on λ has been dropped. These simplifications bring the expression for the beam waist of equation (62) in line with previous derivations (see equations (26) and (27)). Another simplification arises from having equal beam widths in each interferometer leg prior to focusing by lens L_s: ϵ is always 1. Perhaps the only other parameter that requires explanation is M. This magnification parameter results from the fact that the area used to display the hologram may be larger (or smaller) than the area which was scanned to record the hologram.[18] For equal scaling in both the x and y directions, the factor is the ratio between the lateral distance scanned and the width of the hologram. Although

the magnification parameter can be important for optically recorded and reconstructed holograms, the significance of M for numerically reconstructed holograms needs further investigation. Therefore M is assumed to equal 1 for this analysis.

Note that the lateral resolution can be expressed in terms of NA as

$$\Delta x_{osh} = \frac{\sqrt{2}}{\pi}\frac{\lambda}{NA}\left(1+\frac{z^2}{f^2}\right)^{\frac{1}{2}} = 0.45\frac{\lambda}{NA}\left(1+\frac{z^2}{f^2}\right)^{\frac{1}{2}}. \tag{63}$$

When compared to equation (49), which defines the width of a focused Gaussian beam at the $1/e$ point, we see that the resolution criterion for OSH differs by the multiplicative factor $\left(1+\frac{z^2}{f^2}\right)^{\frac{1}{2}}$. Apparently, for $z \ll f$, the resolution limit will be approximately that of a focused Gaussian beam, that is the same as optical microscopy. As z increases, however, the resolution will suffer. For z equal to the focal length, f, the resolution limit is given by

$$\Delta x_{osh} = \frac{2}{\pi}\frac{\lambda}{NA}, \qquad \text{for } z = f, \tag{64}$$

which is $\sqrt{2}$ times worse than the optical case. For $z > f$, equation (63) is no longer valid since the rules of Region 2 in Section 7.1.2 come into play. In Region 2, the NA of lens L_s is no longer relevant. For comparison with resolution limits derived under the Sparrow criterion for optical and confocal microscopy, Δx_{osh} is multiplied by 1.133 (see Section 7.1.5), giving

$$\Delta x_{osh}(\text{Sparrow}) = 0.51\frac{\lambda}{NA}\left(1+\frac{z^2}{f^2}\right)^{\frac{1}{2}}. \tag{65}$$

A final simplification can be made to the original equations for resolution limit. Close inspection of equations (57) and (58) show that Δz_{osh} can be expressed in terms of Δx_{osh} as follows,

$$\Delta z_{osh} = \frac{M\Delta x_{osh}}{1-\frac{M}{2}\Delta x_{osh}\left(\frac{z}{f^2+z^2}\right)}. \tag{66}$$

Longitudinal resolution limits comparable to that of optical microscopy are expected from the OSH system, where $\Delta z_{opt} = \frac{\lambda}{NA^2}$. Note that the longitudinal resolution limit for the optical system can also be expressed in terms of Δx_{opt} as

$$\Delta z_{opt} \propto \frac{1}{NA}\Delta x_{opt}. \tag{67}$$

7.2.3.1 Resolution of the Current OSH Microscopy Setup

Although at this "proof-of-principle" stage, the setup described in Chapter 5 is not optimized for resolution, it is interesting to examine the expected resolution limits for the current setup. The equations from the last section can be put to use determining the limits of resolution. For the system as it stands

$\lambda \quad = 515\,nm$,
$f \quad = 15\ cm$,
$w_p \quad = w_l M_{cp} = 0.5\,cm$,
$z \quad = 3.5\,cm$, and
$M \quad = 1$.

Making use of these values we find

$$NA = \frac{w_p}{f} = \frac{0.5\,cm}{15.0\,cm} = 0.033.$$

Holographic recording is taking place in Region 1, so the OSH microscope is capable of a lateral resolution given by

$$\begin{aligned}\Delta x_{osh} &= 0.45\frac{\lambda}{NA}\left(1+\frac{z^2}{f^2}\right)^{\frac{1}{2}} \\ &= 0.45\left(\frac{515\times10^{-9}}{0.033}\right)\left(1+\left[\frac{0.035m}{0.15m}\right]^2\right)^{\frac{1}{2}} \\ \Delta x_{osh} &= 7.2\,\mu m\end{aligned}$$

The longitudinal resolution is given by

$$\begin{aligned}\Delta z_{osh} &= \frac{M\Delta x_{osh}}{1-\frac{M}{2}\Delta x_{osh}\left(\frac{z}{f^2+z^2}\right)} \\ &= \frac{\left(7.2\times10^{-6}m\right)}{1-\frac{1}{2}(7.2\times10^{-6}m)\left(\frac{0.035m}{(0.15m)^2+(0.035m)^2}\right)} \\ \Delta z_{osh} &= 7.2\,\mu m.\end{aligned}$$

Note that under the assumption $M=1$, the analysis of Duncan and Poon gives approximately equal lateral and longitudinal resolution limits. Using the expected resolution limit of optical microscopy we have

$$\begin{aligned}\Delta z_{osh} \approx \Delta z_{opt} &= \frac{\lambda}{NA^2} \\ &= \frac{515\times10^{-9}}{0.033^2} \\ &= 473\,\mu m.\end{aligned}$$

7.2.3.2 Theoretical and Practical Resolution Limit for Microscopy by OSH

Making use of the analysis presented thus far, expressions for the theoretical limits of resolution for microscopy by OSH can finally be derived. The basis for the derivation is equation (65), repeated here for convenience,

$$\Delta x_{osh} \ = 0.45\frac{\lambda}{NA}\left(1+\frac{z^2}{f^2}\right)^{\frac{1}{2}}.$$

Assuming imaging takes place in the air, the practical limit for NA of 0.95 is used.[40] It is assumed that $\lambda = 515\,nm$ and 10 zones is the minimum number of zones in the FZP for holographic recording. Again, this choice is rather arbitrary, based mainly on the simulations presented in Chapter 3 which suggest the adequacy of 10 zones. The next assumption is that the object will be located in Region 1 at the minimum z distance for $N_z = 10$. From equation (33), the minimum scanning distance for 10 zones inside the $1/e^2$ points of the FZP is $z = 11.4\,\mu m$. With these parameters set, the resolution limit for OSH is determined by the focal length of the lens, L_s. Figure 36 shows a plot of the resolution limit versus focal length for $NA = 0.95$, $n = 10$, $\lambda = 515\,nm$, and $z = z_{min}$. Theoretically, f could be very large, making the multiplicative factor $\left(1+\frac{z^2}{f^2}\right)^{\frac{1}{2}}$ approximately one and maximizing resolution. Therefore, the OSH theoretical resolution limit for a $(1/e)$-point Gaussian beam analysis is

$$\Delta x_{osh} \approx 0.45\frac{\lambda}{NA}. \tag{68}$$

For comparison to the Sparrow criterion, this limit is multiplied by 1.133, giving the identical resolution limit as optical microscopy.

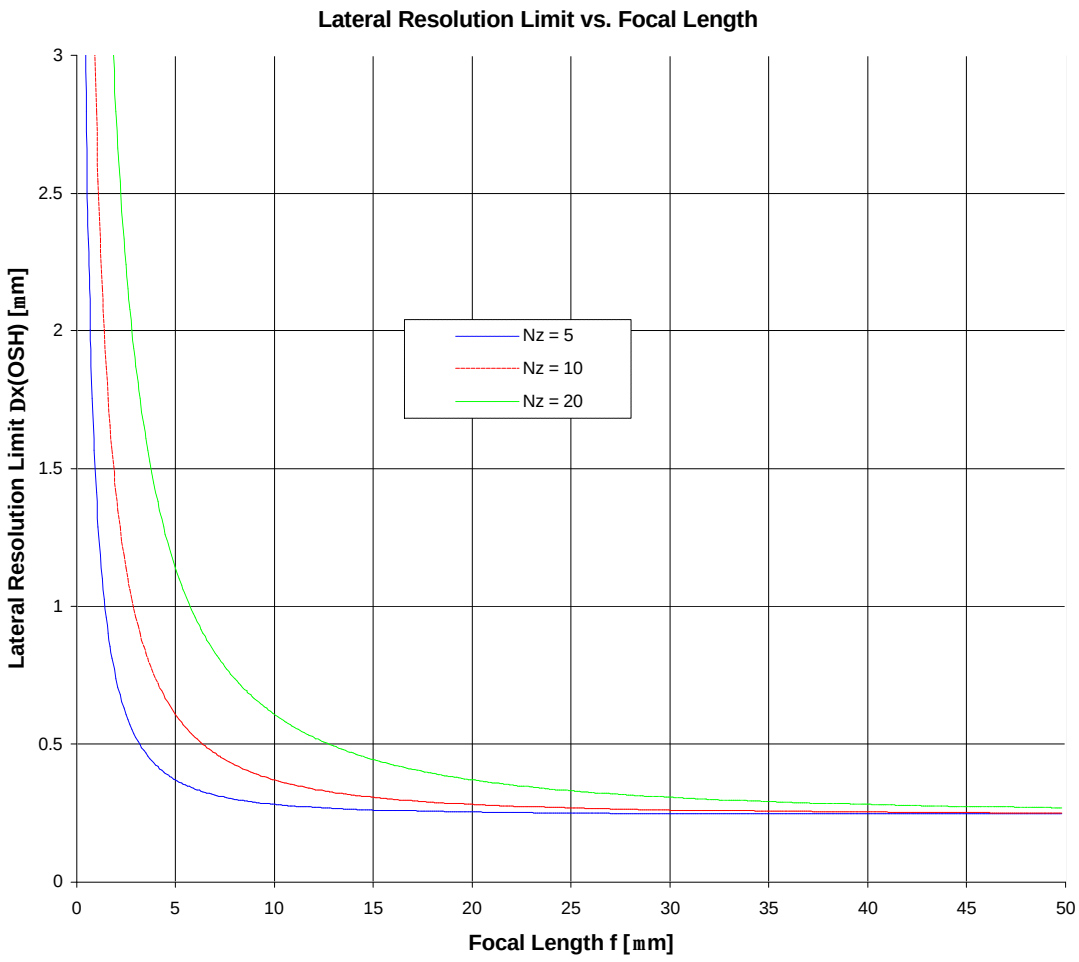

Figure 36 - Plot showing resolution limit for OSH at minimum z

for $NA = 0.95$, and $\lambda = 515\,nm$

There is a practical consideration, however, when f gets very large. Since NA is set, as f gets large, w_p, the beam width of the plane wave must grow accordingly. For large f, the optics quickly become unmanageable. For $f = 100mm$, for example, a plane wave with a 7.5 inch diameter is required for focusing. However, as the plot in Figure 36 shows, focal lengths greater than about $50\ \mu m$ result in nearly maximum resolution. Obviously, we are still quite far from reaching the theoretical limit of resolution for experimental microscopy by OSH.

7.3 Photobleaching Analysis

Photobleaching, a serious problem with 3D fluorescence microscopes, was defined in Chapter 4 as the permanent destruction of fluorescence by light-induced conversion of the fluorophore to a chemically nonfluorescent compound.[42] The effects of photobleaching are reduced by regulating the light dose, or fluence, of the excitation. The main advantage 3D microscopy by OSH has over current methods, such as CSOM, is that it requires a single 2D scan, rather than multiple 2D scans, to collect 3D information. It is natural to assume that the dramatic reduction in scan time afforded by OSH will result in an equally dramatic reduction of photo-damage during image acquisition. However, the large area scan pattern of OSH results in more average fluence on the specimen for a single 2D scan. The amount of photobleaching induced during excitation is proportional to the fluence received by the specimen, where fluence is the irradiance of the specimen times the duration of illumination. Fluence is considered in detail in the sections that follow and is more carefully defined in the next section. This chapter contains a detailed comparison of the amount of photo-damage inflicted by OSH and CSOM.

To compare the two very different systems as fairly as possible, it is satisfactory to analyze each technique based on a specific imaging problem or specimen. The goal of the analysis is to determine and compare the minimum fluence on the object required by each

technique for a 3D image acquisition. A likely specimen might be a 1 μm fluorescent bead. Assume then, that a lateral resolution of better than 1 μm is desired. Under the Sparrow criterion for lateral resolution, the confocal system and the holographic system have the same NA requirement, $NA = 0.26$. Since the confocal system has better axial resolution than the OSH microscope, the amount of photo-damage is determined on a per scan, or per section, basis. For CSOM, approximately the same amount of photobleaching occurs with each section. Therefore, the damage per scan can be multiplied by the total number of sections and directly compared with the OSH case, which requires only a single scan. For equivalent 3D imaging results, each section by the CSOM technique must be made at intervals equal to the longitudinal resolution of the OSH microscope. If the recordable depth in a single hologram was well understood, the number of CSOM sections necessary to match this depth could be calculated. However, the recordable depth has not yet been determined quantitatively.

In order to compare CSOM and OSH, it is necessary to compare the minimum required irradiance of each technique as well as scanning speed. Being the simpler of the two parameters, scanning times are considered first. The minimum excitation irradiance necessary for fluorescence imaging is dependent on the PMT, optical components, and optical design. Peak and average fluence levels received by the fluorescent bead per scan are calculated.

7.3.1 Scanning Times

The current OSH system employs a heavy mechanical 2D scanning mechanism which has a slow scan rate. Typical hologram acquisition times for a 256×256 pixel image are on the order of 20 minutes. When calculating the amount of photobleaching accrued by each system, scanning time is a critical parameter. Photo-damage is

proportional to the fluence received by the fluorophore, where fluence is defined as the irradiance, L, times the exposure time, t_{scan},

$$F = L \times t_{scan.} \tag{69}$$

For a meaningful comparison, it is necessary to assume that the OSH system could be redesigned to achieve a scan rate equivalent to CSOM per section. This is a reasonable assumption. The primary scanning techniques used in CSOM, specimen scanning and beam scanning, have both been demonstrated for OSH. Under this assumption, the total 3D image acquisition time for CSOM is N_s times that for OSH, where N_s is the number of sections recorded for CSOM. Typically 10 to 100 sections are scanned in CSOM for a 3D image acquisition, so the total scan time for OSH will be 10 to 100 times less than for CSOM.

According to Cogswell and Sheppard, a 256×256 pixel, specimen-scanned image acquisition can be completed in as little as 2.5 to 3 seconds.[74] Commercial confocal microscope specifications call out a wide variety of scan rates. Scan times specified for a microscope manufactured by Carl Zeiss, Inc. are anywhere from 0.5 to 64 seconds for an image containing 512×512 pixels.[75] Meridian Instruments, Inc. specifies a minimum scan time for specimen scanning of 55 seconds for a 512×480 pixel image.[76] For this analysis, the actual scan time is less important than the consistency of values used for each method. We will assume a 256×256 pixel, 2D image acquisition can be completed in 3 seconds. Under this assumption, the per pixel dwell time is

$$t_{pix} = 3\,\text{seconds}/(256 \times 256) = 46\,\mu\text{seconds}. \tag{70}$$

7.3.2 Minimum Irradiance Requirement for PMT Detection

The derivation of the fluence on the specimen required by each technique begins with the minimum power requirements of the PMT at the photocathode. The power required for excitation can then be back-calculated by taking into account the sources of signal degradation between the PMT objective and the specimen. Yariv gives an expression for the minimum detectable power for direct detection, which applies to the CSOM case.[77] In direct detection of low light level signals with a PMT, the important sources of noise are shot noise and dark current noise, while thermal and amplifier noise can be neglected. For direct detection, the minimum detectable optical power is given by

$$P_{min}(\text{CSOM}) = \frac{h\nu(i_d B)^{1/2}}{\eta e^{1/2}}, \tag{71}$$

where $h = 6.626 \times 10^{-34}$ joule-second is Planck's constant, ν is the optical frequency of the signal, i_d is the PMT dark current, B is the bandwidth of the electrical filter, η is the quantum efficiency of the PMT and $e = 1.6 \times 10^{-19}$ Coulomb is the charge of an electron.[78] For this experiment $\lambda_f = 590\,nm$ (the wavelength of the fluorescent emission), which corresponds to $\nu = 5.08 \times 10^{14}$ Hz. The limiting bandwidth, from the lowpass electrical filter, is related to the single pixel dwell time according to

$$B = \frac{1}{t_{pix}}. \tag{72}$$

Given the assumptions of the previous section, $B = 1/46\,\mu\text{s} = 21.74\,kHz$. The PMT quantum efficiency is related to the photocathode radiant sensitivity, S in A/W, by[79]

$$\eta = \frac{S \times 1240}{\lambda_f}, \tag{73}$$

where λ_f must be in nanometers.

In most cases of heterodyned detection, the minimum detectable optical power corresponds to a shot noise limited case. This shot noise limited detection is achievable because a strong local oscillator optical field is mixed with the signal just prior to detection by the PMT. This local oscillator field can be made strong enough to dominate all other sources of noise, including dark current noise. For OSH, however, there is no strong local oscillator. The two light beams which interfere to create the optically heterodyned field are both involved in scanning the object. For reflective or transmissive objects, the plane wave is considered as the reference beam corresponding to the local oscillator. For these cases, the power of the plane wave could be increased to achieve shot noise limited detection. Due to the nature of fluorescent specimens and photobleaching, increasing the power of the scanning field in any way is not prudent. For the purposes of this analysis, the two beams which make up the optically heterodyned field for holographic fluorescence microscopy are assumed to be approximately equal in intensity. For this situation the usual advantage of heterodyning (the ability to achieve shot noise limited detection) is not realized. The detection limit given by equation (71), which takes into account both shot noise and dark current noise, will therefore be used for OSH. This will result in equal minimum power requirements for OSH and CSOM, given by

$$P_{min}(\text{OSH}) = P_{min}(\text{CSOM}) = \frac{h\nu(i_d B)^{1/2}}{\eta e^{1/2}}. \tag{74}$$

Note that the bandwidth, B, of equation (74) corresponds to an electrical bandpass filter centered at the heterodyned frequency, although the bandwidth is still defined by equation (72). Dividing by the PMT photocathode's active area, A_{pmt}, converts the minimum power requirement of equation (71) into a minimum irradiance requirement,

$$L_{min} = P_{min}/A_{pmt}. \tag{75}$$

Using the detection limits given by equations (71)-(75) as a starting point, the factors that effect the signal between excitation and detection are each considered by tracing the light path backward from the PMT to the fluorescent specimen in Figure 21.

7.3.3 Excitation Irradiance Requirement

The appropriate transmissivities and reflectivities of the optical elements along the optical signal path must first be taken into account. For both systems, a narrow bandpass filter is used at the PMT objective and a dichroic beamsplitter is incorporated at some point to separate the fluorescent signal from the excitation light. The bandpass filter in our setup has a transmissivity at the fluorescence emission wavelength of τ_{bp}(in band) $= 0.65$. A more dramatic effect comes from the narrow pass band of this filter. Somewhere on the order of 40% of the photons emitted from the fluorophore will be outside the pass band of the emission filter. An effective transmissivity of the bandpass filter is therefore $\tau_{bp} = 0.65 \times 0.40 = 0.26$. Similarly, the dichroic beamsplitter has some reflectivity at the fluorescence wavelength, which is assumed to be $\rho_d = 0.8$.

A primary source of signal loss can be attributed to the collection capability of the PMT and associated optics. When excited, the fluorophore will emit radiation in a sphere. Only a small percent of this total fluorescent emission can be collected by the PMT. Since OSH employs a large area detection scheme, the maximum amount of light is collected, while in CSOM a near diffraction limited point is imaged through an aperture. This gives the holographic system a distinct advantage in collection efficiency over the confocal configuration. Due to the differences in configuration, comparing the collection capabilities of CSOM and OSH is particularly difficult in this analysis. One point of

contention for this comparison concerns the major source of signal attenuation in the confocal system, the pinhole aperture. The pinhole aperture at the detector reduces the amount of fluorescent emission incident on the PMT, and thus SNR, by rejecting emissions from out of focus planes in the specimen. However, the reduced signal is the price that is paid for increased axial resolution, contrast, and sectioning capability. It is hardly fair to compare the harmful effects of photobleaching between systems with different resolution capabilities. For instance, the resolution limit for CSOM could be relaxed to meet that of OSH. In so doing, the diameter of the pinhole could also be expanded, allowing more signal and greater SNR. On the other hand, if the analysis is somehow conducted without the pinhole included, the system is no longer confocal and the comparison becomes totally meaningless. Having stated this point of contention, the problem is basically ignored and the analysis continued. Simple derivations of the percent of fluorescent light that can be collected for the two systems follow.

In the OSH setup, the percent of fluorescent emission that can be collected by the PMT, call it η_c(OSH), is the ratio of the solid angle subtended by the PMT collection aperture, Ω_{pmt}, to that of an entire sphere or $\eta_c = \Omega_{pmt}/4\pi$. To calculate Ω_{pmt}, consider Figure 37, which specifies some needed distances and angles. Interestingly, under the "optimized" configuration shown in Figure 37, the percentage of light collected by the PMT is independent of the collection aperture size, having diameter D_{pmt}. The only assumptions necessary are that the dichroic beamsplitter is as close as possible to (i.e. touching) the PMT objective, is at an angle of $\theta = 45°$, and is large enough to overfill the PMT objective. In addition, the object must be positioned as close as reasonably possible to the dichroic, as shown in the figure. In this configuration, the distance from the specimen to the PMT objective is $2l = D_{pmt}$. The solid angle calculation depends only on D_{pmt} and the distance, l. Figure 37, b) shows an unfolded version with the dichroic beamsplitter removed for clarity. The solid angle is dependent on the area of the PMT objective, $A_{pmt} = \pi(r_{pmt})^2 = \pi(l)^2$according to

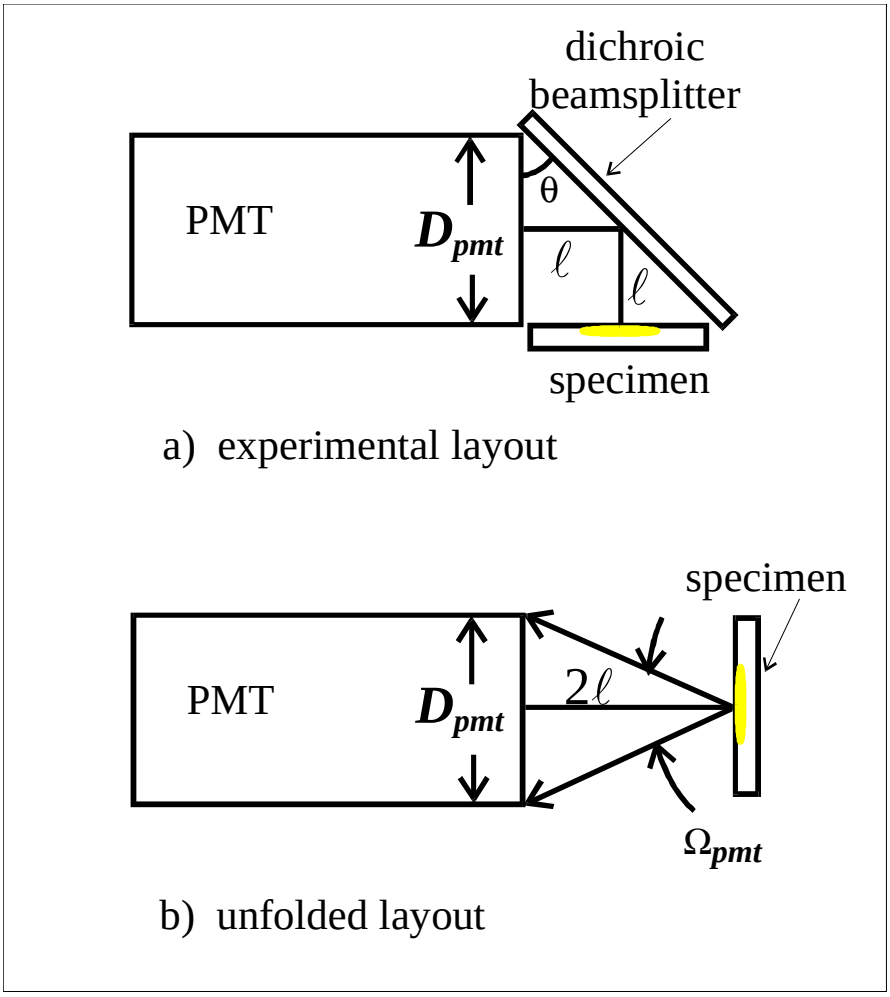

Figure 37 - Diagram used in calculation of η_c(OSH), the light collection efficiency for the wide area detection scheme of OSH

$$\begin{aligned}\Omega_{pmt} &= \frac{A_{pmt}}{4l^2} \\ &= \frac{\pi(r_{pmt})^2}{4l^2} \\ &= \frac{\pi(l)^2}{4l^2} \\ &= \pi/4, \end{aligned} \tag{76}$$

where r_{pmt} is the radius of the PMT objective's active area. The percentage of fluorescent light collected by the PMT is

$$\eta_c(\text{OSH}) = \Omega_{pmt}/4\pi = 1/16. \tag{77}$$

A similar derivation is conducted to determine the percentage of fluorescent emission collected in the CSOM case. In commercial confocal microscopes the objective also acts as the condenser, thus the solid angle of collected light is proportional to NA^2. The solid angle that subtends the objective is $\Omega_{obj} = \pi(NA)^2$. With an NA of 0.26, $\Omega_{obj} = 0.21$ and η_c for CSOM is given by

$$\eta_c(\text{CSOM}) = \Omega_{obj}/4\pi = 0.017. \tag{78}$$

According to this analysis, somewhere around 6% of the light can be collected using the large area detector scheme of OSH, while less than 2% of the fluorescent emission is collected by the confocal microscope objective. An additional source of loss is attributed to signal blocked by the pinhole itself. Stelzer suggests that the optimal detection pinhole diameter is given by,

$$P_d = 1.22\frac{\lambda_f}{NA}, \tag{79}$$

but a 10% to 30% smaller pinhole is often used in practice.[72] Using $\lambda_f = 590\,nm$ and $NA = 0.26$, gives an optimal pinhole diameter of $P_d = 2.77\,\mu m$ for this system. A 30% smaller pinhole would correspond to a diameter of $1.9\,\mu m$. Integrating equation (44) out to the radius of the optimum pinhole size indicates that about 84% of the power will pass through a pinhole of $2.77\,\mu m$. This will be considered as a transmissivity factor attributed to the pinhole, designated $\tau_p = 0.84$.

Two other factors must be considered in determining the total minimum signal required to meet the PMT detection limit. These are the quantum efficiency of the fluorophore, η_f, and in the case of heterodyned excitation, the demodulation factor which was introduced in Chapter 4. Quantum efficiencies vary widely among fluorescent dyes, anywhere from a few percent to near one-hundred percent. For instance, when EB is bonded to DNA, the quantum efficiency is below 50%. However, the quantum efficiency of the fluorescent beads used in our experiment is close to 100%. For this exercise, a quantum efficiency of 80% is assumed. Finally, in the case of heterodyned excitation, a demodulation factor must be included in the calculation. As discussed in Chapter 4, when a fluorescent sample is excited by a sinusoidal light field, the modulated emission is delayed in phase and has a modulation index that is smaller than that of the excitation. The relationship for first order, single exponential decay is repeated here for convenience,[46]

$$m = [1 + \omega^2\tau^2]^{-\frac{1}{2}}. \tag{80}$$

The demodulation factor for $\Delta\Omega/2\pi = 10.7\,\text{MHz}$ and a fluorescent lifetime $\tau = 5\ ns$ is $m = 0.95$.

Taking all factors into account, the minimum excitation irradiance resulting in fluorescent emission above the detector sensitivity threshold is given by

$$L_{ex}(\text{OSH}) = \frac{L_{min}(\text{OSH})}{\tau_{bp}\rho_d\eta_f m\eta_c(\text{OSH})} \tag{81}$$

for OSH. A similar equation describes the minimum required excitation irradiance for the confocal system,

$$L_{ex}(\text{CSOM}) = \frac{L_{min}(\text{CSOM})}{\tau_{bp}\rho_d\eta_f\eta_c(\text{CSOM})\tau_p}. \tag{82}$$

Comparing the excitation irradiance requirements of the two systems we see that

$$L_{ex}(\text{CSOM}) = L_{ex}(\text{OSH}) \times \frac{\eta_c(OSH)}{\eta_c(CSOM)} \times \frac{m}{\tau_p}. \tag{83}$$

The last two terms in equation (83) represent the difference between minimum excitation irradiance levels of the two systems. The first of these terms stems from the large aperture detection scheme of OSH, while in CSOM the fluorescent signal is imaged through a pinhole. From the analysis above, OSH collects the fluorescent signal about 3.7 times more efficiently than CSOM. The last term is the demodulation factor divided by the effective transmissivity of the pinhole used in the detection stage of a confocal microscope. Using the "optimum" pinhole diameter of $P_d = 1.22\,\mu m$, this factor is about 1.13. From equation (83) we see that the confocal system will require more than 4 times the irradiance on the specimen in order to break the PMT detection threshold. The following equation stipulates this relation

$$L_{ex}(\text{CSOM}) \approx 4 \times L_{ex}(\text{OSH}). \tag{84}$$

7.3.4 Total Power Contained in the Scanning Beam

In the previous section, a value for the minimum excitation irradiance level was calculated based on PMT detection limits. However, in OSH, the sample is scanned by a relatively large scanning pattern with varying intensity throughout the pattern. In CSOM, a tightly focused Airy pattern is scanned over the specimen. The total power of the scanning beam is calculated from the excitation irradiance derived in the previous section coupled with the profile of the scanning pattern. The OSH case is considered first. Remember, the point must be scanned through an FZP pattern given in cylindrical coordinates by

$$I_{fzp}(\rho,\, z) = exp\Big[-\tfrac{2\rho^2}{\omega_{fzp}^2}\Big]\big\{A^2 + B^2 + 2AB sin\big[\tfrac{\pi}{\lambda z}\rho^2\big]\big\}. \tag{85}$$

The variables A and B are determined from the initial amplitudes of the plane and spherical wave that make up the FZP pattern. If we make the assumption that $A = B$, equation (85) reduces to

$$\begin{aligned} I_{fzp}(\rho,\, z) \qquad &= exp\Big[-\tfrac{2\rho^2}{w_{fzp}^2}\Big]\big\{2A^2 + 2A^2 sin\big[\tfrac{\pi}{\lambda z}\rho^2\big]\big\} \\ &= 2A^2 exp\Big[-\tfrac{2\rho^2}{w_{fzp}^2}\Big]\big\{1 + sin\big[\tfrac{\pi}{\lambda z}\rho^2\big]\big\}. \end{aligned} \tag{86}$$

Due to the overall Gaussian shape of the beam, the intensity will be greater in the center than at the edges. In addition, the intensity varies according to the $sin(\frac{\pi}{\lambda z}\rho^2)$ term, through a maximum and a minimum for each zone. Once again, it becomes necessary to choose an outlying zone or fringe of the FZP which will irradiate the fluorophore at the excitation irradiance threshold. Fringes outside of the selected zone will excite the

specimen, but result in a signal below the detection threshold of the PMT. Radiation from these outer fringes will, on the other hand, irradiate the sample and contribute to photobleaching. Radiation from these zones could, in principle, be masked off to improve the photobleaching situation, but this analysis assumes no masking. As for previous cases, the tenth zone is selected as the last necessary zone for holographic recording by OSH. This leads to the requirement that the half irradiance point (middle) of the tenth fringe must excite the specimen at the minimum irradiance. This point corresponds to a lateral distance at which the sine term equals zero, simplifying the mathematics to a certain extent, and the Gaussian exponential term equals $1/e^2$. Under these assumptions, the intensity at this radial distance is given by $I_{fzp} = 2A^2/e^2$, which must equal the minimum required irradiance, or $2A^2/e^2 = L_{ex}$(OSH). From this relation, we calculate a value for A^2 which can then indicate a laser power requirement,

$$A^2 = (L_{ex}(\text{OSH}) \times e^2)/2. \tag{87}$$

Substitution into equation (86) yields

$$I_{fzp}(\rho, z) = e^2 L_{ex}(\text{OSH})\left\{exp\left(-\frac{2\rho^2}{w_{fzp}^2}\right)\left[1 + sin\left(\frac{\pi}{\lambda z}\rho^2\right)\right]\right\}. \tag{88}$$

A normalized one dimensional version of this equation is shown in Figure 38, which shows $I_{fzp}(\rho, z)/L_{ex}$(OSH) versus ρ. Note that the Gaussian windowing function brings the FZP to $1/e^2$ of its maximum at about the tenth fringe. Also note that the scanning pattern has intensity of L_{ex}(OSH) at the half intensity point of the same zone. Since the specimen must be convolved with the entire FZP, it follows that during an image acquisition the fluorescent specimen will receive an irradiance dose equal to the total power in the scanning beam, to the radial distance described in Section 7.1.4. The power in the pattern

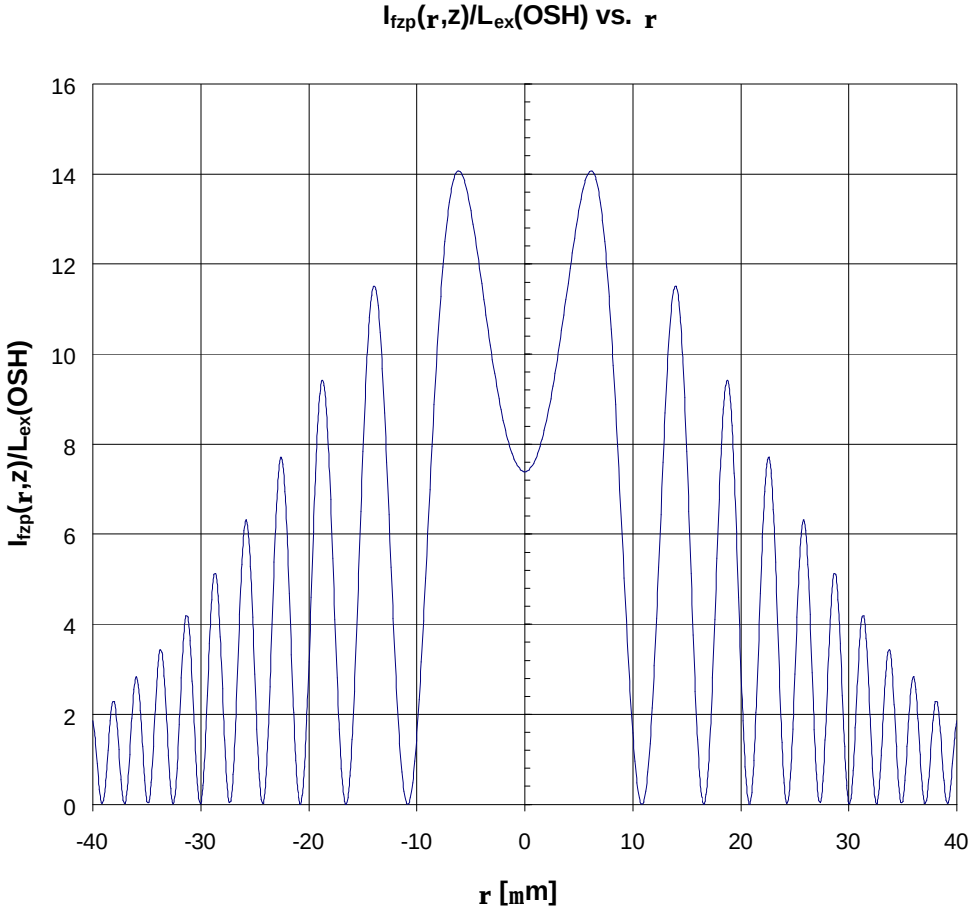

Figure 38 - Normalized FZP intensity profile

is calculated by integrating the Gaussian apodized FZP over the total scan area, with limits as defined in Section 7.1.4, or

$$P_{OSH} = e^2 L_{ex}(\text{OSH}) \int_0^{\rho_{tot}} \int_0^{2\pi} exp\Big[-2\tfrac{\rho^2}{w_{fzp}^2}\Big]\big\{1 + sin\big(\tfrac{\pi}{\lambda z}\rho^2\big)\big\}\rho d\rho d\phi$$

$$= e^2 L_{ex}(\text{OSH}) 2\pi \int_0^{\rho_{tot}} exp\Big[-2\tfrac{\rho^2}{w_{fzp}^2}\Big]\big\{1 + sin\big(\tfrac{\pi}{\lambda z}\rho^2\big)\big\}\rho d\rho, \tag{89}$$

where $\rho_{tot} = \big(\frac{1}{2}x_{ext} + w_{fzp}\big)$, as derived in Section 7.1.4. The integration is conducted numerically using Mathematica in the calculation section to follow.

For the confocal case the scanning pattern is not Gaussian, but the Airy pattern. As Figure 35 shows, the Airy pattern also has maximum intensity in the center, decays with radial distance, and contains circular fringes. The equation for the Airy pattern at the focus of the objective lens, given by equation (44), is repeated here for convenience,

$$I_{\text{Airy}}(\rho) = I_0\left\{\tfrac{2J_1[2\pi(NA)\rho/\lambda]}{2\pi(NA)\rho/\lambda}\right\}^2. \tag{44}$$

Similar to the OSH case, it is assumed that the required excitation irradiance level must occur at the $1/e^2$ point of the central lobe of the Airy pattern. Therefore $I_0 = e^2 L_{ex}(\text{CSOM})$. Using equation (83), I_0 is written is terms of $L_{ex}(\text{OSH})$ as

$$I_0 = e^2 L_{ex}(\text{OSH}) \times \tfrac{\eta_c(OSH)}{\eta_c(CSOM)} \times \tfrac{m}{\tau_p}. \tag{90}$$

Just as in the case with OSH, the specimen will be scanned through the beam, receiving the total irradiance in the Airy pattern out to the limits derived in Section 7.1.4. The size

of the scanning beam is not a factor for a focused spot scan, so the limits of integration are $\rho_{tot} = x_{ext}/2$. The power in the scanning pattern that is incident on the specimen is therefore

$$P_{CSOM} = I_0 \int_0^{\rho_{tot}} \int_0^{2\pi} \left\{ \frac{2J_1[2\pi(NA)\rho/\lambda]}{2\pi(NA)\rho/\lambda} \right\}^2 \rho d\rho d\phi$$

$$= e^2 L_{ex}(CSOM) 2\pi \int_0^{\rho_{tot}} \left\{ \frac{2J_1[2\pi(NA)\rho/\lambda]}{2\pi(NA)\rho/\lambda} \right\}^2 \rho d\rho. \quad (91)$$

In order to determine the total irradiance in the Airy pattern, the equation must be integrated over the scan area. Again, the total power in the scanning beam is integrated numerically to determine actual power.

7.3.5 Peak Irradiance and Peak Fluence

Both peak and average fluence levels are important for the photobleaching analysis. Peak irradiance and fluence levels are derived in this section. In OSH with a sine-based FZP, the peak irradiance will occur at the innermost bright ring where the sine term has a value of one. At this point, the Gaussian multiplier will have some value slightly less than one, reducing the peak irradiance level. Rather than complicating the analysis by determining this value, an upper bound is calculated under the assumption that both the sine term and the Gaussian term are one. For OSH the peak irradiance level is L_{pk}(OSH) $= 2e^2 L_{ex}$(OSH). For CSOM the peak irradiance occurs at the center of the Airy pattern, and is given by L_{pk}(CSOM) $= I_0 = e^2 L_{ex}$(CSOM). If equation (83) is used

we see that the peak irradiance for the confocal system can be written in terms of the peak irradiance for the holographic case or,

$$L_{pk}(\text{CSOM}) = \tfrac{1}{2} L_{pk}(\text{OSH}) \times \tfrac{\eta_c(OSH)}{\eta_c(CSOM)} \times \tfrac{m}{\tau_p}. \tag{92}$$

Thus, the necessary peak irradiance of laser excitation for the confocal microscope is roughly 2 times that required by the holographic system for the assumed parameters.

As defined by equation (69), fluence is the irradiance times the exposure time. The peak fluence is the peak irradiance times the time it takes to acquire a single pixel of data. Under the assumptions of Section 7.3.1, the single pixel dwell times for OSH and CSOM will be identical. Therefore, the peak fluence levels between the two systems will obey the same relationship as that of peak irradiance. Under the previous assumptions for bandwidth and dark current ($B = 22\,kHz$, $i_d = 20nA$), the optimum pinhole diameter of $P_d = 2.44\,\mu m$, and using the collection efficiencies derived in Section 7.3.3, CSOM will result in about 2 times the peak fluence of OSH, or $F_{pk}(\text{CSOM}) \approx 2F_{pk}(\text{OSH})$.

7.3.6 Energy and Average Fluence

Finally, average fluence on the specimen is calculated. An expression for the total radiant power received by the specimen during a 2D image acquisition was derived in Section 7.3.3. Multiplying the power in the beam by the time required for a complete 2D scan gives the total radiant energy received by the specimen during a 2D scan. Average fluence is determined by dividing this energy by the area scanned. Again, scan times of $t_{scan} = 3$ seconds are assumed for both methods. For OSH and CSOM the area upon which the radiation is incident is the same, $x_{ext} \times y_{ext}$. The following relations hold for a single 2D scan by either technique,

$$E = P \times t_{scan} \tag{93}$$

$$F_{ave} = \frac{E}{x_{ext} \times y_{ext}} = \frac{P \times t_{scan}}{x_{ext} \times y_{ext}} \tag{94}$$

For CSOM, the fluorescent bead will receive approximately the same level of average fluence during each scan. This is easily understood by considering equation (94). For planes in the specimen other than the plane of focus, the Airy pattern will be spread out. However, approximately the same amount of total power is in the spread Airy pattern as in the focused case. The integration of equation (91) calculates the total power under the curve, resulting in very nearly the same average fluence for each section. If N_s is the number of sections recorded, a 3D image acquisition by CSOM will irradiate the fluorophore with an average fluence of approximately $N_s \times F_{ave}$(CSOM). For OSH, only a single 2D scan is required to record the complete 3D image, so F_{ave}(OSH) is the total average fluence for a 3D image acquisition.

7.3.7 Calculations

The information compiled in this chapter allows for a complete comparison of the photobleaching effects of OSH and CSOM. In this section, the analysis is concluded with a numerical example. The first step is to calculate the minimum required irradiance levels at the PMT objective for each system. Table 3 lists a number of important specifications for a PMT manufactured by Hamamatsu (model number R1221, the PMT used in the current OSH experiment).

Table 3 - Summary of relevant PMT specifications[79]

Quantity	Symbol	Numerical Value	Source
dark current	i_d	$20\,n$A	Ref. 79
anode pulse time response	t_r	$2.6\,n$S	Ref. 79
photocathode useful area	A_{pmt}	$17\,cm^2$	Ref. 79
bandwidth	B	$22\,kHz$	eq. (72)
cathode radiant sensitivity (420nm peak)	S	$51\,m$A/W	Ref. 79
quantum efficiency	η	0.123	eq. (73)

From Table 3 and equations (71)-(75), the minimum irradiance levels for OSH and CSOM are:

$$L_{min}\text{(CSOM)} = L_{min}\text{(OSH)} = 8.6 \times 10^{-12}\text{W/cm}^2.$$

Relevant low light detection limits are tabulated in Spring and Lowy.[80] The detection limit of the eye is given as $.017$ nW/cm^2, while the lowest irradiance level detectable by the best video image tube (1989) is 8.5×10^{-4} nW/cm^2. Spring and Lowy also give a practical lower limit for direct detection as 0.17×10^{-4} nW/cm^2. Note that these numbers are based on a SNR of about 3, while the minimum power levels of equations (71)-(75) are for a SNR equal to 1.

The next step is to calculate the minimum excitation irradiance level, based on these PMT requirements. Minimum excitation irradiance is determined by taking into account the sources of signal degradation between the PMT and fluorescent specimen. A number of values needed for this calculation have been pulled from the literature, assumed, or calculated from simple fundamentals. These values are summarized in Table 4. From Table 4 and equations (81) and (82), the excitation requirements are

L_{ex}(OSH) $= 0.87\,n$W/cm^2, and

L_{ex}(CSOM) $= 3.6\,n$W/cm^2.

Table 4 - Summary of values used for photobleaching analysis

Quantity	Symbol	Numerical Value	Source
irradiance detection limit (OSH)	L_{min}(OSH)	$8.6\ p$W/cm^2	eq. (75)
irradiance detection limit (CSOM)	L_{min}(CSOM)	$8.6\ p$W/cm^2	eq. (75)
transmissivity of bandpass filter	τ_{bp}	0.26	assumed
reflectivity of dichroic beam splitter	ρ_d	0.8	assumed
quantum efficiency of fluorophore	η_f	0.8	assumed
demodulation factor	m	0.948	eq. (80)
photon collection efficiency (OSH)	η_c(OSH)	$1/16 = 0.0625$	eq. (77)
photon collection efficiency (CSOM)	η_c(CSOM)	0.017	eq. (78)
diameter of pinhole	P_d	$2.77\ \mu m$	eq. (79)
transmission through pinhole	τ_p	0.84	eq. (79)
2D image scanning time	t_{scan}	3 seconds	ref. 74
single pixel dwell time (256×256)	t_{pix}	46 μseconds	eq. (70)

As expected, the required excitation irradiance for CSOM is more than four times that of OSH. The difference can be attributed to the signal lost in collection capability of the confocal technique. Stelzer estimates the detection efficiency of a commercial confocal microscope based on a similar analysis as 0.3%, which agrees well with this analysis.[72] Steltzer's analysis does not include the factor for the quantum efficiency of the fluorophore, therefore the efficiency factor is calculated without this factors for comparison. Steltzer's analysis also differs from ours in that Steltzer includes an extra loss factor of about 12% for the scan/relay lens and scanning mirror. As we are assuming specimen scanning in our system, this factor does not come into play in our analysis.

With values for excitation irradiance levels for the two systems in hand, peak irradiance and fluence levels can be calculated according to the analysis of Section 7.3.4,

L_{pk}(OSH) $= 12.9\ n$W/cm^2, and

L_{pk}(CSOM) $= 27\ n$W/cm^2.

Again, these values are in line with the expected results. The peak irradiance of CSOM with a spot scanning approach is more than twice that of OSH with the broader FZP scanning field. Peak fluence is determined by multiplying these peak irradiance values by the single pixel dwell time. From equation (70), this time is $t_{pix} = 46\,\mu$seconds and peak fluence levels are

F_{pk}(OSH) $= 0.59\ \ pJ/cm^2$, and
F_{pk}(CSOM) $= 1.2\ \ pJ/cm^2$.

For this numerical example, therefore the peak fluence delivered by each system are related by

$$F_{pk}(\text{CSOM}) \approx 2F_{pk}(\text{OSH}). \tag{95}$$

The next step is to calculate the power in the scanning beams. The variables in equations (89) and (91) must be calculated first. As elsewhere in this analysis, the required number of zones in the FZP is assumed to be 10. From equation (51), a resolution limit of $1.0\,\mu m$ will require an $NA = 0.26$. The minimum z for $NA = 0.26$ is calculated from equation (33) to be $152\,\mu m$. For a 1.0 μm object, the Nyquist criterion for the highest spatial frequency in the object is fulfilled with a sampling step size of 0.5 μm. Remember, the Nyquist requirement must be met for the FZP pattern as well. With the help of equation (39) the sampling rate for 10 fringe OSH must be greater than 1.0 μm. The sampling rate requirement due to the object's highest spatial frequency is therefore the more stringent of the two requirements. In practice, it is a good idea to slightly over sample, so $\Delta x_s = 0.3$ μm will be used. The limits of integration can now be determined. From equation (40), $x_{ext} = y_{ext} = 77\,\mu m$, and from equation (31) the beam radius is $40\,\mu$m. The limits on the integration are then ρ_{tot}(OSH) $= 78\,\mu m$ for OSH and

ρ_{tot}(CSOM) $= 38\,\mu m$ for CSOM. Table 5 gives a summary of the values needed to perform the integrals of equations (89) and (91).

Table 5 - Calculated values for equations (89) and (91)

Quantity	**Symbol**	**Numerical Value**	**Source**
desired lateral resolution	Δx	$1.0\,\mu m$	assumed
numerical aperture	NA	0.26	eq. (51)
number of zones	N_z	10	assumed
minimum scan distance	z_{min}	$152\,\mu m$	eq. (33)
lateral extent scanned	x_{ext}	$77\,\mu m$	eq. (40)
Gaussian beam radius of FZP	w_{fzp}	$40\,\mu m$	eq. (31)
limits of integration FZP	ρ_{tot}(OSH)	$78\,\mu m$	eq. (41)
limits of integration Airy	ρ_{tot}(CSOM)	$38\,\mu m$	Sec. 7.3.3

The integration, carried out using Mathematica, gives the following expressions for the power in the scanning fields in terms of the excitation irradiance levels required by the two systems. For OSH,

$$\begin{aligned} P_{OSH} &= e^2 L_{ex}(\text{OSH}) \times [(2500\,\mu m^2)] \\ &= (1.9 \times 10^{-4}\,cm^2)(L_{ex}(\text{OSH})) \\ &= 0.17\,p\text{W}, \end{aligned}$$

where the bracketed term is the power integral carried out by Mathematica. For the confocal case

$$\begin{aligned} P_{CSOM} &= e^2 L_{ex}(\text{CSOM}) \times [(1.2\,\mu m^2)] \\ &= (9.2 \times 10^{-8} cm^2)(L_{ex}(\text{CSOM})) \\ &= 0.33\,f\text{W}. \end{aligned}$$

The important relationship between the power in the scanning beams is emphasized by expressing P_{OSH} in terms of P_{CSOM} as

$$P_{OSH} \approx 500 P_{CSOM}. \tag{96}$$

In the final analysis we find that the total power in the OSH scanning beam is more than 500 times that of OSH. Equation (96) represents one of the most important results of this analysis as it relates the total illumination power for the two systems. For a single scan, $P_{OSH} \approx 500 P_{CSOM}$. As described in section 7.3.6, and under the assumption that 2D scan times are equal for both systems, the total energy incident on the specimen will obey the same relationship as that of equation (96), given by

$$E_{OSH} \approx 500 E_{CSOM}. \tag{97}$$

Likewise, the average fluence delivered by the two 3D fluorescence imaging systems follows directly from the same equation. This relationship is approximated by

$$F_{ave}(\text{OSH}) \approx 500 F_{ave}(\text{CSOM}). \tag{98}$$

For this numerical example, equations (95) and (98) clearly indicate the difference in photobleaching between OSH and CSOM. For the given parameters, the average fluence on the specimen for OSH is many hundred times that of CSOM, although the peak fluence of the CSOM system is higher. For a 3D image acquisition with the confocal system, the specimen will receive approximately the same amount of photodamage with each section. Even still, for a complete 3D image acquisition CSOM could acquire 500 sections before the average fluence received by the fluorescent specimen will be equal to that of OSH.

Radiant energy and average fluence received by the specimen for a 2D scan are calculated according to equations (93) and (94). These values, along with other major results stemming from the photobleaching analysis are summarized in Table 6.

7.3.8 Summary of Photobleaching Analysis

In this chapter, OSH and CSOM have been compared in the areas of image acquisition speed, resolution limit and photobleaching. For OSH, a number of preliminary relationships were derived prior to addressing these main areas. Relationships such as those between the number of zones in the scanning pattern, scanning distance, NA and sampling rate were addressed. Though necessary for the analysis that followed, these relationships are important in their own right. Careful consideration indicates that the OSH system will have a 3D image acquisition time equal to the 2D image acquisition time of CSOM. This effectively makes OSH N_s times faster than CSOM, where N_s is the number of sections taken with the confocal microscope. The photobleaching analysis shows that OSH can offer an advantage over CSOM when it comes to peak fluence, and therefore the level of instantaneous photo-damage due to the scanning beam. However, for an entire 2D scan, the broad FZP scanning field will irradiate the specimen with more total energy that the spot scanning technique used for CSOM. For a 3D image acquisition, OSH will irradiate the specimen with about the same amount of energy as 500 sections taken by CSOM.

Table 6 - Major results of the photobleaching analysis

Quantity	**Symbol**	**Numerical Value**	**Source**
excitation irradiance (OSH)	L_{ex}(OSH)	$0.87\,n$W/cm^2	eq. (81)
excitation irradiance (CSOM)	L_{ex}(CSOM)	$3.6\,n$W/cm^2	eq. (82)
peak irradiance (OSH)	L_{pk}(OSH)	$12.9\,n$W/cm^2	Sec. 7.3.5
peak irradiance (CSOM)	L_{pk}(CSOM)	$27\,n$W/cm^2	Sec. 7.3.5
peak fluence (OSH)	$\boldsymbol{F_{pk}}$**(OSH)**	$\boldsymbol{0.59\,pJ/cm^2}$	Sec. 7.3.5
peak fluence (CSOM)	$\boldsymbol{F_{pk}}$**(CSOM)**	$\boldsymbol{1.2\ pJ/cm^2}$	Sec. 7.3.5
power in scanning beam (OSH)	P_{OSH}	$0.16\,p$W	eq. (89)
power in scanning beam (CSOM)	P_{CSOM}	$0.33\,f$W	eq. (91)
energy per scan (OSH)	E_{OSH}	$0.5\,p$J	eq. (93)
energy per scan (CSOM)	E_{CSOM}	$0.99\,f$J	eq. (93)
average fluence (OSH - 3D)	$\boldsymbol{F_{ave}}$**(OSH)**	$\boldsymbol{83.6\,\mu J/cm^2}$	eq. (94)
average fluence (CSOM - 2D)	$\boldsymbol{F_{ave}}$**(CSOM)**	$\boldsymbol{16.7\,\mu J/cm^2}$	eq. (94)

8.0 Conclusions and Future Research

The objective of this project has been the application of optical scanning holography to fluorescence microscopy. The work has been primarily experimental in nature, coupled with computer-based simulation and image reconstruction. Aside from the novelty of a new fluorescence microscopy technique, the practicality of the idea has been investigated through a detailed comparison between OSH and the industry standard for 3D fluorescent microscopic imaging, the confocal scanning optical microscope.

The original OSH setup was redesigned to accommodate fluorescent specimens. Alterations included the use of an argon-ion laser source. A unique AOM configuration was employed to generate a heterodyned laser excitation field suitable for fluorescent specimens. Specimen scanning replaced the beam scanning approach used in previous OSH experiments. In addition, a custom software application was developed to control the scanning and synchronize it with data acquisition. Finally, the photodetector of previous setups has been replaced with a PMT for improved sensitivity.

Although heterodyne methods have been employed in the detection of weak fluorescence signals,[81] to our knowledge no experiment has been conducted which uses a heterodyned light field to excite a fluorescent sample. To generate the excitation field, the AOM is driven by a mixed radio frequency signal. Fluorescent samples were irradiated and the response to this field was recorded. The preliminary results indicated that incoherent holography of fluorescent objects is feasible. The project culminated with the successful demonstration of 3D holographic imaging of a fluorescent microscopic specimen by OSH. The fluorescent specimen consisted of a solution containing a high concentration of 15 μm diameter fluorescent beads. Upon numerical image reconstruction, the fluorescent beads were distinguishable at different depths.

After the successful demonstration of a new and novel technique for 3D fluorescence microscopy, attention was directed to practical considerations. In this vein, a detailed comparison of 3D fluorescence microscopy by OSH with the confocal approach was conducted on the basis of 3D image acquisition time, resolution limits and photobleaching. The analysis shows that an optimized OSH-based fluorescence microscope can offer improved image acquisition time with equal lateral resolution, but with degraded longitudinal resolution when compared to CSOM. The OSH system will deliver a lower peak fluence to the specimen, which will reduce the instantaneous damage of photobleaching. For a single 2D scan, however, the broad FZP scanning pattern irradiates the specimen with significantly more average fluence than the spot scan of CSOM. This means that for a 2D scan, OSH will cause more damage due to photobleaching than confocal microscopy. However, the great advantage of OSH is the need for only a single 2D scan to record 3D information, while multiple sections are recorded for 3D imaging by CSOM. For the particular example, OSH incurred about 500 times the average fluence of CSOM. Therefore, the confocal system will cause less total photobleaching provided less than 500 sections are recorded.

The experimental as well as the analytical results presented here give us the incentive to continue to research 3D holographic fluorescence microscopy by OSH. A major goal of future research is the application of the system to biological specimens. As a means to this end, several areas of improvement are discussed. Future research will include eliminating the twin-image noise with special algorithms during image reconstruction. The twin-image problem has been carefully studied for several years, and remains an active area of research for the Optical Image Processing Laboratory. There is plenty of room for improvement to the current system's limits of resolution and magnification. Attention to these parameters will involve major modification to the existing system. To improve the system's resolution, the NA must be increased, either by using larger diameter beams or a shorter focal length lens to create the FZP.

As with most optical systems, especially those involving interferometry, optical alignment is critical in the OSH setup. It is imperative to have the plane wave and spherical wave of Figure 21 collinear when superposition of these fields takes place. Slight misalignment will result in poor heterodyning and reduced signal. A second consequence of misalignment is that a slightly skewed FZP scans the object. The assumption inherent in the numerical reconstruction process is that a perfect FZP is used for holographic recording. A skewed pattern will therefore cause distortion. One solution is to record the scanning pattern along with the hologram as the object is being scanned. The actual pattern could then be used as the impulse response for numerical reconstruction. Figure 39 suggests a setup in which a pinhole detector records the intensity distribution of the scanning pattern. A dichroic beamsplitter that reflects 5% or 10% of the excitation field is used. Like the specimen, the pinhole detector must be a distance z from the focus of lens L_s. Synchronized mechanical platforms are shown in the figure, but are not necessary if beam scanning is employed. Incorporating scanning pattern detection in the recording process of OSH may open up completely new areas of research. In addition to potentially eliminating distortions stemming from an imperfect FZP scanning field, the setup of Figure 39 might be used to investigate completely different scanning patterns. Alternate patterns could result in a reduction of twin-image noise or holograms that exhibit edge enhancement upon reconstruction.

There are many possibilities for continued research on 3D imaging by OSH. Improvements such as those suggested here will bring OSH to yet another level and closer to the ultimate goal of holographic microscopy of biological specimens. Although preliminary, the results presented here are an important step in the development of the 3D holographic fluorescence microscope.

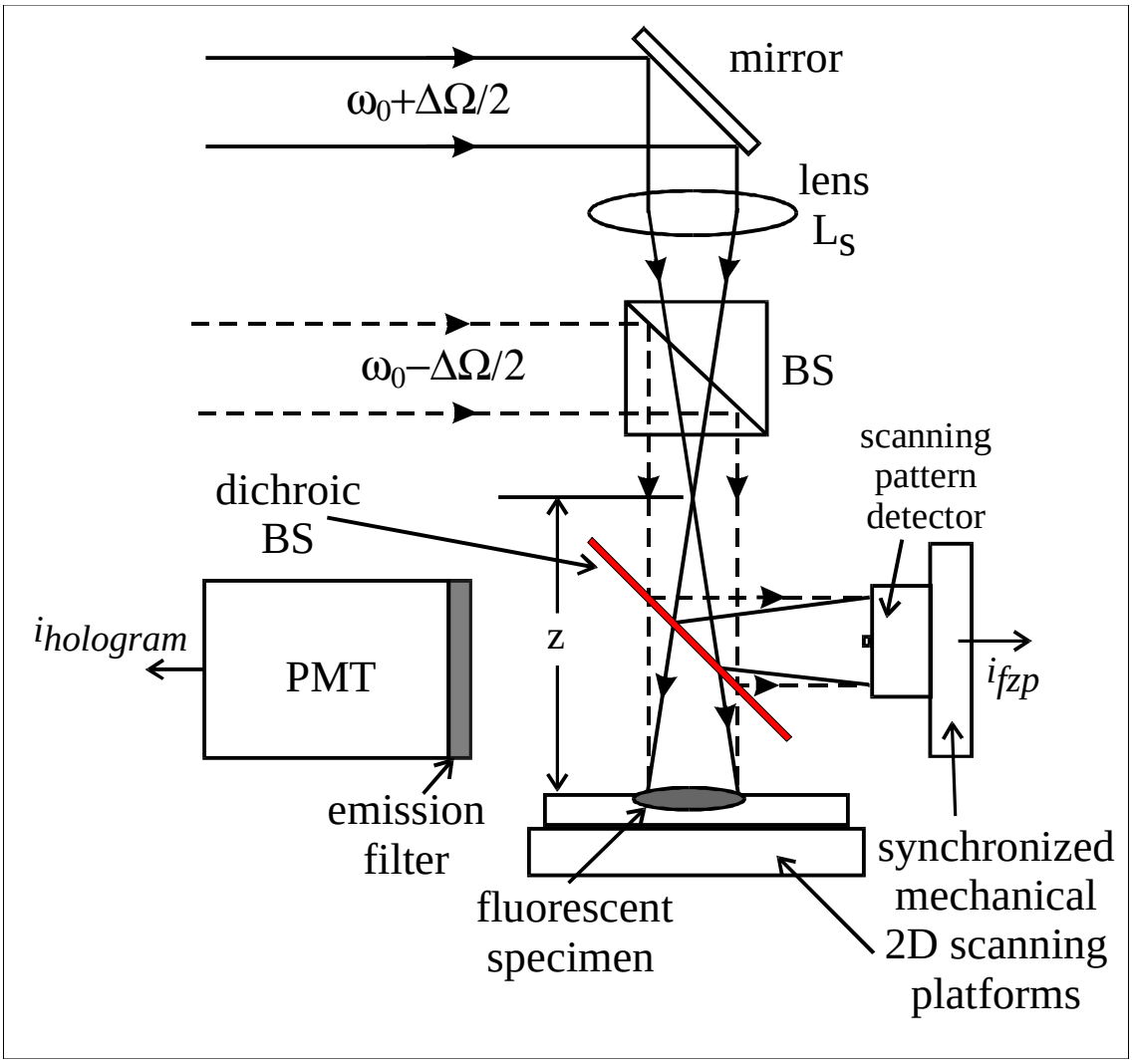

Figure 39 - Proposed setup to record scanning pattern during holographic recording

References

1. D. Gabor, "Microscopy by reconstructed wavefronts," *Proceedings of the Royal Society of London*, Vol. 197, pp. 454-487, (1949).

2. T.-C. Poon and A. Korpel, "Optical transfer function of an acousto-optic heterodyning image processor," *Optics Letters*, Vol 4, pp. 317-319, (1979).

3. T.-C. Poon, "Method of two-dimensional bipolar incoherent image processing by acousto-optic two-pupil synthesis," *Optics Letters*, Vol 10, pp. 197-199, (1985).

4. T.-C. Poon, "Scanning Holography and Two-Dimensional Image Processing by Acoustic-Optic Two-Pupil Synthesis," *Journal of the Optical Society of America A* Vol 2, pp. 521-527, (1985).

5. L. Mertz and N. O. Young, "Fresnel Transformations of Images," *Proceedings of the Conference on Optical Instruments and Techniques*, K. J. Habell, ed. Chapman and Hall, London, pp. 305-312, 1962.

6. A. W. Lohmann, "Wavefront reconstruction for incoherent objects," *Journal of the Optical Society of America*, Vol. 55, pp. 1555-1556, 1965.

7. Gary Cochran, "New method of making Fresnel transforms with incoherent light," *Journal of the Optical Society of America*, Vol. 56, No. 11, pp. 1513-1517, Nov. 1966.

8. George W. Stroke and Robert C. Restrick III, "Holography with spatially noncoherent light," *Applied Physics Letters*, Vol. 7, No. 9, pp. 229-230, Nov. 1965.

9. H. R. Worthington, Jr., "Production of holograms with incoherent illumination," *Journal of the Optical Society of America*, Vol. 56, No. 10, pp. 1397-1398, Oct. 1966.

10. P. J. Peters, "Incoherent holograms with mercury light source," *Applied Physics Letters*, Vol. 8, No. 8, pp. 209-210, Apr. 1966.

11. O. Bryngdahl and A. Lohman, "One-dimensional holography with spatially incoherent light," *Journal of the Optical Society of America*, Vol. 58, No. 5, pp. 625-628, May 1968.

12. C. B Burckhardt and E. T. Doherty, "Formation of carrier frequency holograms with an on-axis reference beam," *Applied Optics*, Vol. 7, No. 6, pp. 1191-1192, Jun. 1968.

13. Adam Kozma and Norman Massey, "Bias level reduction of incoherent holograms," *Applied Optics*, Vol. 8, No. 2, pp. 393-397, Feb. 1969.

14. Gabriel Sirat and Demetri Psaltis, "Conscopic holography," *Optics Letters*, Vol. 10, No. 1, pp. 4-6, Jan. 1984.

15. T.-C. Poon, B. D. Duncan, M. H. Wu, K. Shinoda and Y. Suzuki, "Real-time Optical Holography Using a Spatial Light Modulator," *Japanese Journal of Applied Physics*, Vol 29, pp. L1840-L1842, 1990.

16. B. D. Duncan, "Investigation of real-time optical scanning holography," Ph.D. dissertation, Virginia Polytechnic Institute and State University, Blacksburg, VA, 1991.

17. B. D. Duncan, T.-C. Poon, M. H. Wu, K. Shinoda and Y. Suzuki, "Real-time Reconstruction of Scanned Optical Holograms Using an Electron-Beam-Addressed Spatial Light Modulator," *Journal of Modern Optics*, Vol 39, pp. 63-80, 1992.

18. B. D. Duncan and T.-C. Poon, "Gaussian Beam Analysis of Optical Scanning Holography," *Journal of the Optical Society of America A*, Vol 9, pp. 229-236, 1992.

19. T.-C. Poon, B. W. Schilling, M. H. Wu, K. Shinoda and Y. Suzuki: "Real-Time Two-Dimensional Holographic Imaging Using an Electron-Beam-Addressed Spatial Light Modulator," *Optics Letters*, Vol 18, pp. 63-65, 1993.

20. B. W. Schilling, "Advances in Real-time Optical Scanning Holography," M.S. thesis, Virginia Polytechnic Institute and State University, Blacksburg, VA, 1992.

21. G. Indebetouw and T.-C. Poon, "Novel Approaches of Incoherent Image Processing With Emphasis on Scanning Methods," *Optical Engineering*, Vol 31, pp. 2159-2167, 1992.

22. K. Doh, T.-C. Poon, M. H. Wu, K. Shinoda, and Y. Suzuki, "Twin-Image Elimination in Optical Scanning Holography," *Optics & Laser Technology*, Vol. 28, pp. 135-141 (1996).

23. K. B. Doh, T.-C. Poon, G. Indebetouw, "Twin-image noise in optical scanning holography," *Optical Engineering*, Vol 35, No. 6, pp. 1550-1555, (1996).

24. B. W. Schilling and T.-C. Poon, "Real-time preprocessing of holographic information," *Optical Engineering*, Vol. 34, No. 11, pp. 3174-3180, Nov. (1995).

25. T.-C. Poon, K. B. Doh, B. W. Schilling, M. H. Wu, K. Shinoda, and Y. Suzuki, "Three-dimensional microscopy by optical scanning holography," *Optical Engineering*, Vol 34, No. 5, pp. 1338-1344, (1995).

26. B. W. Schilling, T.-C. Poon, G. Indebetouw, B. Storrie, K. Shinoda, Y. Suzuki, and M. Wu, "Three-dimensional holographic fluorescence microscopy," *Optics Letters*, Vol. 22, pp. 1506-1508 (1997).

27. B. Saleh and M. Teich, *Fundamentals of Photonics.* Wiley, New York, 1991.

28. Product information sheet for the EBSLM model X3636, provided by Hamamatsu Photonics K.K., Japan and Hamamatsu Corp., Bridgewater, NJ, 1989.

29. B. W. Schilling, T.-C. Poon, M.H. Wu, K. Shinoda and Y. Suzuki, "Advances in optical scanning holography," *Optical information Processing, SPIE Proceedings*, Vol. 2051, pp. 364-375 (1993).

30. Craig A. Lindley, *Practical Image Processing in C.* John Wiley & Sons, Inc. New York, 1991.

31. P. P. Banerjee and T.-C. Poon, *Principles of Applied Optics.* Akensen Associates Inc. Boston, 1991.

32. James S. Walker, *Fast Fourier Transforms.* CRC Press, Boston, 1991.

33. William H. Press, Brian P. Flannery, Saul A. Teukolsky, and William T. Vetterling, *Numerical Recipes in C, The Art of Scientific Computing*. Cambridge University Press, Cambridge, MA, 1988.

34. J. W. Goodman, *Introduction to Fourier Optics.* McGraw-Hill Publishing Company, Inc. New York, 1968.

35. Taylor, D.L.; Nederlof, M.; Lanni, F.; Waggoner, A.S., "The new vision of light microscopy," *American Scientist*, vol.80, no.4, p. 322-35, Jul. 1992.

36. Ploem, J.S., "Laser scanning fluorescence microscopy," *Applied Optics*, vol.26, no.16, p. 3226-31, 15 Aug. 1987.

37. Arndt-Jovin, D.J.; Robert-Nicoud, M.; Kaufman, S.J.; Jovin, T.M., "Fluorescence digital imaging microscopy in cell biology," *Science*, vol.230, no.4723, p. 247-56, 18 Oct. 1985.

38. Hell, S.; Stelzer, E.H.K., "Properties of a 4Pi confocal fluorescence microscope," *Journal of the Optical Society of America A*, vol.9, no.12, p. 2159-66, Dec. 1992

39. Kimura, S.; Munakata, C., "Depth resolution of the fluorescent confocal scanning optical microscope," *Applied Optics*, vol.29, no.4, p. 489-94, 1 Feb. 1990

40. Rita G. Lerner and George L. Trigg, *Encyclopedia of Physics, Second Edition.* VCH Publishers, Inc., New York, 1991.

41. Ronald Waynant and Marwood Ediger, *Electro-optics Handbook*, McGraw-Hill, Inc., New York, 1994.

42. D. Lansing Taylor and E. D. Salmon, "Basic fluorescence microscopy." In Yu-Li Wang and D. Lansing Taylor (Eds.), *Methods in Cell Biology*. Vol. 29, pp. 207-237. Academic Press, Inc., Boston,1989.

43. Rost, F. W. D., *Fluorescence Microscopy,* Cambridge University Press, Cambridge, 1992.

44. Haugland, Richard P., *Handbook of Fluorescent Probes and Research Chemicals, 5th Edition.* Molecular Probes, Inc., Oregon, 1992.

45. J. S. Ploem and H. J. Tanke, *Introduction to Fluorescence Microscopy.* Oxford University Press, New York, 1987.

46. J. R. Lakowicz, *Principles of Fluorescence Spectroscopy.* Plenum Press, New York, 1983.

47. Robert M. Clegg and Peter C. Schneider, "Fluorescence Lifetime-Resolved Imaging Microscopy: A General Description of Lifetime-Resolved Imaging Measurements." In J. Slavik (Ed.), *Fluorescence Microscopy and Fluorescence Probes*. (pp. 15-33) Plenum Press, New York, 1996.

48. Hans C. Gerritsen, "Confocal Fluorescence Lifetime Imaging." In J. Slavik (Ed.), *Fluorescence Microscopy and Fluorescence Probes*. (pp. 35-46) Plenum Press, New York, 1996.

49. M. vandeVen and E. Gratton, "Time-Resolved Fluorescence Lifetime Imaging." In Brian Herman and John J. Lemasters (Eds.), *Optical Microscopy, Emerging Methods and Applications*. (pp. 373-402) Academic Press, New York, 1993.

50. Peter T. Waltenberg and Peter J. Hilton, "Laser Induced Fluorescence Lifetime Measurement." *SPIE Proceedings*, Vol. 2349, pp. 160-166, 1995.

51. T. Araki, N. Hanabusa, T. Uchida, X. F. Wang, and s. Minami, "Versatile and high-repetition subnanosecond light source for fluorescence lifetime measurements," *Applied Spectroscopy*, Vol. 46, No. 3, 1992.

52. F. W. D. Rost, *Quantitative Fluorescence Microscopy.* Cambridge University Press, New York, 1991.

53. Steve Potter, "Vital imaging: Two photons are better than one," *Current Biology*, Vol. 6, No. 12, pp. 1595-1598, 1996.

54. G. L. Picciolo and D. S. Kaplan, "Reduction of Fading of Fluorescent Reaction Product for Microphotometric Quantitation." In Allen I. Laskin (Ed.), *Advances in Applied Microbiology*. Vol. 30, pp 197-234. Academic Press, Inc., New York, 1984.

55. John E. Wampler and Karl Kutz, "Quantitative fluorescence microscopy using photomultiplier tubes and imaging detectors." In Yu-Li Wang and D. Lansing Taylor (Eds.), *Methods in Cell Biology*. Vol. 29, pp. 239-267. Academic Press, Inc., Boston, 1989.

56. J. Lichtman, "Confocal microscopy," *Scientific American*, Vol. 271, No. 2, pp. 40-45, August (1994).

57. David A. Agard, Yasushi Hiraoka, Peter Shaw and John W. Sedat, "Fluorescence Microscopy in Three Dimensions." In Yu-Li Wang and D. Lansing Taylor (Eds.), *Methods in Cell Biology*. Vol. 30, pp. 353-377. Academic Press, Inc., Boston,1989.

58. Winfried Denk, James Strickler and Watt Webb, "Two-Photon Laser Scanning Fluorescence Microscopy," *Science*, Vol. 248, pp. 73-76 1990.

59. C. J. R. Sheppard and R. Kompfner, "Resonant scanning optical microscope," *Applied Optics*, Vol. 17, pp. 2879-2883 1978.

60. C. J. R. Sheppard, R. Kompfner, J. Gannaway and D. Walsh, "The scanning harmonic optical microscope," *IEEE Journal of Quantum Electronics*, Vol. QE-13, p. 100D.

61. Steve Potter, C. M. Wang, P. A. Garrity, and S. E. Fraser, "Intravital imaging of green fluorescent protien using 2-photon laser-scanning microscopy," *Gene*, Vol. 173, pp. 25-31 1996.

62. S. Maiti, Jason B. Shear, R. M. Williams, W. R. Zipfel and Watt W. Webb, "Measuring Serotonin Distribution in Live Cells with Three-Photon Excitation," *Science*, Vol. 275, pp. 530-532, 1997.

63. Min Gu and J. R. Sheppard, "Comparison of three-dimensional imaging properties between two-photon and single-photon fluorescence microscopy," *Journal of Microscopy*, Vol. 177, pp. 128-137 1995.

64. *Cirqtel Incorporated Standard Filters Product Guide*, 10504 Wheatly street, Kensington, Maryland 20795.

65. Gerald F. Marshall, ed. *Optical Scanning*, Marcel Dekker, Inc. New York, 1991.

66. *MotionMaster 2000 Advanced Motion Controller User's Manual, Revision 3.1*, Newport/Klinger Corporation, 999 Stewart Ave, Garden City NY 11530.

67. *DAQ Lab-PC+ User Manual*, National Instruments Corporation, 6504 Bridge Point Parkway, Austin TX 78730, August 1994 Edition.

68. Amnon Yariv, *Quantum Electronics, 3rd Ed.* John Wiley & Sons, New York, 1989.

69. W. J. Smith, *Modern Optical Engineering*. McGraw-Hill, Inc., New York, 1990.

70. Walter T. Welford, *Useful Optics.* The University of Chicago Press, Chicago, 1991.

71. M. Born and E. Wolf, *Principles of Optics, Sixth Edition*. Pergamon Press, New York, New York, (1980).

72. Ernst H. K. Stelzer, "Designing a Confocal Microscope." In P. C. Cheng, T. H. Lin, W. L. Wu, J. L. Wu (Eds.), *Multidimensional Microscopy*. Springer-Verlag, New York, 1994.

73. Timothy R. Corle and Gordon S. Kino, *Confocal Scanning Optical Microscopy and Related Imaging Systems.* Academic Press, New York, 1996.

74. C. J. Cogswell and C. J. R. Sheppard, "Confocal Brightfield Imaging Techniques Using an On-Axis Scanning Optical Microscope." In T. Wilson (Ed.) *Confocal Microscopy*. Academic Press, New York, 1990.

75. Zeiss LSM 410 Invert Product Information Sheet, Inverted Lasr Scan Microscope for Biology and Medicine. Carl Zeiss, Inc., Miscroscope Division. One Zeiss Drive, Thornwood, New York 10594. 800-233-2343. 1993.

76. The Ultima Product Information Sheet, Premium Laser Confocal Microsope System. Meridian Instruments, Inc. 2310 Science Parkway, Okemos, Michigan 48864. 800-247-8084. 1993.

77. Amnon Yariv, *Optical Electronics, 3rd Ed*. Holt, Rinehart and Winston, New York, 1985.

78. R. E. Simon, *RCA Electro-Optics Handbook.* RCA, Solid State Division, Electro Optics and Devices, Lancaster, PA 17604. 1974.

79. Hamamatsu product information guide, "Photomultiplier Tubes and Assemblies for Scintillation Counting and High Energy Physics," provided by Hamamatsu Photonics K.K., Japan and Hamamatsu Corp., Bridgewater, NJ, 1994.

80. Kenneth R. Spring and R. Joel Lowy, "Characteristics of Low Light Level Television Cameras." In Yu-Li Wang and D. Lansing Taylor (Eds.), *Methods in Cell Biology.* Vol. 29, pp. 269-289. Academic Press, Inc., Boston,1989.

81. W.-K. Lee, A. Gungor, P.-T. Ho, and C. C. Davis, "Direct measurement of dilute dye solution quantum yield by photothermal laser heterodyne interferometry," *Applied Physics Letters*, Vol. 47, No. 9, 1 Nov. 1985.

VITA

Bradley Wade Schilling was born in Portsmouth, Virginia on September 15, 1967. He graduated from Tabb High School in Tabb, Virginia in 1985. He received a Bachelor of Science degree in electrical engineering from Virginia Polytechnic Institute and State University (Virginia Tech) in May 1989. Since June, 1989, Mr. Schilling has been employed by the U.S. Army's Night Vision and Electronic Sensors Directorate, Ft. Belvoir, Virginia. As a member of the Advanced Laser Branch, Mr. Schilling has been involved in the design and development of many laser based electro-optical systems, such as those used for rangefinding, fire control and obstacle avoidance. Mr. Schilling received his Master of Science degree in 1992, also from Virginia Tech. His research interests include laser systems, 3D imaging, holography, optical information processing, digital image processing and fluorescence microscopy.

Mr. Schilling is a member of the Optical Society of America (OSA), The Society for Photo-Optical Instrumentation Engineers (SPIE), and the American Association for the Advancement of Science (AAAS). His personal interests are primarily outdoor activities, including mountain biking and extended backpacking trips.